



University of Kentucky  
UKnowledge

---

Theses and Dissertations--Mechanical  
Engineering

Mechanical Engineering

---


2020

## COARSE-GRAINED DYNAMICALLY ACCURATE SIMULATIONS OF IONIC LIQUIDS AT VACUUM-INTERFACE

Tyler D. Stoffel

University of Kentucky, tdstoff7@gmail.com

Author ORCID Identifier:

 <https://orcid.org/0000-0003-2244-5505>

Digital Object Identifier: <https://doi.org/10.13023/etd.2020.086>

[Right click to open a feedback form in a new tab to let us know how this document benefits you.](#)

### Recommended Citation

Stoffel, Tyler D., "COARSE-GRAINED DYNAMICALLY ACCURATE SIMULATIONS OF IONIC LIQUIDS AT VACUUM-INTERFACE" (2020). *Theses and Dissertations--Mechanical Engineering*. 148.  
[https://uknowledge.uky.edu/me\\_etds/148](https://uknowledge.uky.edu/me_etds/148)

This Master's Thesis is brought to you for free and open access by the Mechanical Engineering at UKnowledge. It has been accepted for inclusion in Theses and Dissertations--Mechanical Engineering by an authorized administrator of UKnowledge. For more information, please contact [UKnowledge@lsv.uky.edu](mailto:UKnowledge@lsv.uky.edu).

## **STUDENT AGREEMENT:**

I represent that my thesis or dissertation and abstract are my original work. Proper attribution has been given to all outside sources. I understand that I am solely responsible for obtaining any needed copyright permissions. I have obtained needed written permission statement(s) from the owner(s) of each third-party copyrighted matter to be included in my work, allowing electronic distribution (if such use is not permitted by the fair use doctrine) which will be submitted to UKnowledge as Additional File.

I hereby grant to The University of Kentucky and its agents the irrevocable, non-exclusive, and royalty-free license to archive and make accessible my work in whole or in part in all forms of media, now or hereafter known. I agree that the document mentioned above may be made available immediately for worldwide access unless an embargo applies.

I retain all other ownership rights to the copyright of my work. I also retain the right to use in future works (such as articles or books) all or part of my work. I understand that I am free to register the copyright to my work.

## **REVIEW, APPROVAL AND ACCEPTANCE**

The document mentioned above has been reviewed and accepted by the student's advisor, on behalf of the advisory committee, and by the Director of Graduate Studies (DGS), on behalf of the program; we verify that this is the final, approved version of the student's thesis including all changes required by the advisory committee. The undersigned agree to abide by the statements above.

Tyler D. Stoffel, Student

Dr. Sergiy Markutsya, Major Professor

Dr. Alexandre Martin, Director of Graduate Studies

COARSE-GRAINED DYNAMICALLY ACCURATE SIMULATIONS OF IONIC  
LIQUIDS AT VACUUM-INTERFACE

---

THESIS

---

A thesis submitted in partial fulfillment of the  
requirements for the degree of Master of Science in  
Mechanical Engineering in the College of Engineering at  
the University of Kentucky

By  
Tyler D. Stoffel  
Lexington, Kentucky

Co-Directors: Dr. Sergiy Markutsya, Assistant Professor of Mechanical Engineering,  
Dr. Y. Charles Lu, Professor of Mechanical Engineering  
Lexington, Kentucky 2020

Copyright© Tyler D. Stoffel 2020  
<https://orcid.org/0000-0003-2244-5505>

## ABSTRACT OF THESIS

### COARSE-GRAINED DYNAMICALLY ACCURATE SIMULATIONS OF IONIC LIQUIDS AT VACUUM-INTERFACE

Ionic liquids, possessing improved properties in many areas of technical application, are excellent candidates as components in development of next-generation technology, including ultra-high energy batteries. If they are thus applied, however, extensive interfacial analysis of any selected ionic configuration will likely be required. *Molecular dynamics* (MD) provides an advantageous route by which this may be accomplished, but can fall short in observing some phenomena only present at larger time/length scales than it can simulate. Often times this is approached by *coarse-graining* (CG), with which scope of simulation can be significantly increased. However, coarse-grained MD systems are generally known to produce inaccurately “fast” dynamics. In this work, two different sets of ionic liquid pairs are coarse-grained from atomistic MD reference systems, expanding their system size and time duration capabilities for analysis at vacuum-interface. The dynamics of each system are corrected using the novel in-house *probability distribution function coarse-graining* (PDF-CG) method. The bonded structure, non-bonded structure and dynamics of each system are developed and proven to match reference system data at two temperature scales. Density profile results of vacuum-interface exposure show effects of both temperature scaling and CG method, varying significantly from bulk behavior. At the interface, a density increase, cation orientations and multilayer ordering are observed.

KEYWORDS: Ionic liquids, molecular dynamics, coarse-grained, vacuum-interface

---

Tyler D. Stoffel

Author

---

April 1, 2020

Date

COARSE-GRAINED DYNAMICALLY ACCURATE SIMULATIONS OF IONIC  
LIQUIDS AT VACUUM-INTERFACE

By  
Tyler D. Stoffel

Dr. Sergiy Markutsya  
Co-Director of Thesis

---

Dr. Y. Charles Lu  
Co-Director of Thesis

---

Dr. Alexandre Martin  
Director of Graduate Studies

---

April 1, 2020

---

Date

Dedicated to my remarkable wife, who endured many sleepless and lonely nights that this work may be accomplished. You are my greatest gift of this world.

*'A wife of noble character who can find? She is worth far more than rubies. Her husband has full confidence in her and lacks nothing of value. She brings him good, not harm, all the days of her life.'*

Proverbs 31:11-12

## ACKNOWLEDGMENTS

Firstly, thanks goes to my advisor on this work, Dr. Sergiy Markutsya. His immense dedication to the success and quality of not only this project, but the lives of every student he mentors is vastly apparent. He has spurred my interest and passion for understanding the natural world, while mentoring me in essential life wisdom. I now look forward with confidence to the challenges and opportunities that this educational work affords me. I would also like to thank Dr. Charles Lu for being an invaluable voice of wisdom and honesty in my education. My other committee members: Dr. José Graña-Otero and Dr. Sean Bailey, thank you for contributing your time and expertise to help me achieve this milestone.

Above all, I must thank God, who is the ultimate deliverer of all things good, with which he has blessed me abundantly. Often, His help comes forth through the people placed in one's life. By grace, a staggering many of these wonderful people have been implanted to mine. Hence, I would especially like to thank my wonderful family and friends for abundant support and encouragement; my dear wife Emma Stoffel, who has made many sacrifices for this work to be possible, all the while with joyful grace and fortitude. My parents: Brian and Lisa Stoffel, for their great support to myself and my family. My wife's parents: Tim and Sherri Percy, for always being there - especially when we need babysitters. My great and ever-trusted friend Jordan Garcia, for being as a brother to me. Also, my foundation of devoted friends: John Higgins, Nathan Schmidt, Alex Bolin and Tommy Harper. The colleagues who contributed to this work: Alex Doom, Austin Haley and Donovan McKinney.

I also thank the imperative contributors to this work, without which it would not have been possible. My collaborators from NASA Ames Research center: Dr. John Lawson and Justin Haskins, who provided the highly valuable reference data used here. Also, Dr. Gregory Voth for graciously sharing the algorithm required for performing his group's Force Matching method. Finally, I am thankful to the NASA Kentucky Space Grant Consortium for providing the significant funding required to bring me through my program and to this work. The material in this thesis is based upon work supported by NASA Kentucky under NASA award No: NNX15AR69H.

# Contents

<b>Acknowledgements</b>	<b>iii</b>
<b>List of Tables</b>	<b>v</b>
<b>List of Figures</b>	<b>vi</b>
<b>Nomenclature</b>	<b>vii</b>
<b>1 Introduction</b>	<b>1</b>
<b>2 Theory</b>	<b>4</b>
2.1 System Trajectories and Averages . . . . .	4
2.2 All-atom Molecular Dynamics . . . . .	4
2.3 Coarse-grained Molecular Dynamics . . . . .	6
2.4 The Probability Distribution Function Coarse-graining Method . . . . .	6
<b>3 Methods</b>	<b>8</b>
3.1 All-atom Reference Systems . . . . .	8
3.2 Construction of Coarse-grained Models . . . . .	9
3.3 Coarse-grained Structure Calibration . . . . .	11
3.3.1 Bonded Structure Calibration . . . . .	11
3.3.2 Non-bonded Structure Calibration . . . . .	14
3.4 Coarse-grained Dynamics Calibration . . . . .	15
3.5 Summary of Calibration . . . . .	17
<b>4 Results</b>	<b>18</b>
4.1 Bonded Structure . . . . .	18
4.2 Non-bonded Structure . . . . .	20
4.3 Dynamics . . . . .	21
<b>5 Application</b>	<b>24</b>
5.1 Vacuum-interface Systems . . . . .	24
5.2 Interfacial Properties . . . . .	25
<b>6 Conclusions</b>	<b>32</b>
<b>A Appendix</b>	<b>34</b>
A.1 Coarse-graining Information . . . . .	34
A.2 Representations of Systems . . . . .	35
A.3 Bonded Distributions . . . . .	39
A.4 Radial Distribution Functions . . . . .	45
A.5 Non-bonded Forces . . . . .	47
A.6 Mean-square Displacements . . . . .	50
A.7 Density Profiles . . . . .	52
<b>Bibliography</b>	<b>63</b>
<b>Vita</b>	<b>67</b>



# List of Tables

2.1	Ensembles applied in this work. . . . .	4
3.1	Parameters of all-atom reference systems. . . . .	9
3.2	Parameters of structure calibration systems. . . . .	11
3.3	Parameters of dynamics calibration systems. . . . .	15
3.4	Non-bonded pair groupings for $\Delta t_0$ . . . . .	16
3.5	Summary of calibration processes. . . . .	17
4.1	Values of $\alpha, \beta$ determined . . . . .	22
4.2	Diffusion coefficients of the [pyr14][TFSI] ionic liquid. . . . .	22
4.3	Diffusion coefficients of the [EMIM][BF <sub>4</sub> ] ionic liquid. . . . .	23
5.1	Parameters of vacuum-interface systems. . . . .	24
5.2	Ions evaporated at interface. . . . .	24

# List of Figures

1.1	Typical scopes of simulation tools. . . . .	2
3.1	Ionic liquids considered in this work. . . . .	8
3.2	Coarse-grained sites of [pyr14][TFSI]. . . . .	10
3.3	Coarse-grained sites of [EMIM][BF <sub>4</sub> ]. . . . .	10
3.4	Boltzmann inversion process. . . . .	12
3.5	Examples of all-atom bonded distributions from [pyr14][TFSI]. . . . .	13
4.1	Example [pyr14][TFSI] bonded distribution results. . . . .	18
4.2	Example [EMIM][BF <sub>4</sub> ] bonded distribution results. . . . .	19
4.3	Example non-bonded force field results. . . . .	20
4.4	Example radial distribution function results. . . . .	21
5.1	By-type number density profiles of [pyr14][TFSI]. . . . .	26
5.2	By-type number density profiles of [EMIM][BF <sub>4</sub> ]. . . . .	26
5.3	Effect of temperature on [pyr14] <sup>+</sup> density profiles. . . . .	27
5.4	Effect of temperature on [EMIM] <sup>+</sup> density profiles. . . . .	27
5.5	Orientation of [pyr14] <sup>+</sup> cation from density plots. . . . .	28
5.6	Orientation of [EMIM] <sup>+</sup> cation from density plots. . . . .	29
5.7	Effect of CG method on [pyr14] <sup>+</sup> density profiles at 298K. . . . .	30
5.8	Effect of CG method on [EMIM] <sup>+</sup> density profiles at 298K. . . . .	30
5.9	Main site density profile samples. . . . .	31

# Nomenclature

## Physics Constants

$k_B$  Boltzmann Constant  $1.380\,648\,52 \times 10^{-23} \text{ m}^2\text{s}^{-2}\text{K}^{-1}\text{kg}$

## Symbols

$A$  Any general property

$b(r)$  Bonded distribution (probability)

$D$  Diffusion coefficient

$E$  Total energy

$F$  or  $\mathbf{F}$  Resultant force on a particle or each of  $N$  particles

$g(r)$  Radial distribution function

$m$  or  $\mathbf{m}$  Mass of a particle or each of  $N$  particles

$MSD$  Mean-square displacement

$N$  Global number of particles

$n$  Local number of particles

$p$  or  $\mathbf{p}$  Momentum of a particle or each of  $N$  particles

$r$  or  $\mathbf{r}$  Position of a particle or each of  $N$  particles

$T$  Temperature

$t$  Time

$U$  Potential energy

$V$  Volume

$v$  or  $\mathbf{v}$  Velocity of a particle or each of  $N$  particles

# 1 Introduction

*Ionic liquids* are a class of organic solvents which, in recent decades, have increasingly gathered attention from chemists and other technical experts. Distinguished from the more broad classification of molten salts by their melting temperature, they exist as liquids at temperatures less than 100 °C [1]. An immediate result of this distinction is that ionic liquids are peculiarly easy to handle at the level of the chemist and every-day user, although they are functional and novel in many other ways. They have negligible vapor pressure, a wide liquid range, low flammability, high thermal stability and ionic conductivity, and can solvate with many compounds, including those with highly varying polarity [2]. This makes them not only viable for a wide range of synthetic and catalytic processes [3], but also attractive for applications in many fields, including development of next-generation technology.

To name an example of interest, certain ionic liquids with imidazolium or sulfonium-based cations and complex halide anions [4] are considered for electrolytes in improved Lithium batteries [5]. Applying new electrode materials, such as Lithium-air, in conjunction with such alternative electrolytes provides the potential to supersede current Lithium-ion battery technology. Lithium-air technology is theoretically more energy-dense than most traditional battery designs while having potential to stand above emerging technologies, making it an excellent candidate in the developing market of mobile electrically-powered technology. It has been limited, though, by multiple technical challenges like low charge/discharge cycling efficiency, internal shorts from dendrite formation and poor humidified air management [6]. Since ionic liquids possess improved properties in these areas, they have the potential to solve such problems. Hence, using ionic liquids at the interface of such electrodes could significantly assist in breaking through the performance barrier to widespread implementation of electrically-powered transportation, such as hybrid-electric aircraft [7–9]. Additionally, if such technology were to be applied in space, the vacuum-interface behavior of such liquids would be of great interest to the user.

Many investigations, both experimental [10, 11] and computational [12, 13] have shown that interactions at interfaces have significant influence on the structure of ionic liquids. Presence of interfaces can change the ordering of anions and cations, thus influencing dynamic, transport, and rheological properties. Knowing these effects are present when exposed to various interfaces, a fundamental knowledge of such behaviors is crucial for technological development. Computational methods, such as *molecular dynamics* (MD), are a valuable tool for gaining insight into the behavior of these fluids at the nano and meso-scales, at which it is notably difficult to physically observe phenomena. By definition, molecular dynamics is a computer simulation method to study the movement of individual atoms and molecules by implementing the Newtonian equations of motion. *Atomistic* or *all-atom* (AA) molecular dynamics methods are those that apply the equations of motion at the level of the atom. A number of molecular dynamics simulations have been performed to study the interfacial structure of ionic liquids, providing useful insight about ion orientation, layering, surface tension and other properties [14, 15].

Perhaps the greatest obstacle in applying these algorithms, especially atomistic molecular dynamics, is limitation in time and space, also called *phase space*. As the number of atoms present or the duration of simulation is increased, so is the computational cost. Recent experimental studies suggest that ionic liquid systems with interfaces can induce

structuring at scales of micrometer in simulation space length and over an hour in duration [16–18], significantly larger in space and time than a typical atomistic molecular dynamics simulation. Furthermore, extensive use of atomistic models is inhibited by high viscosity and charge density of ionic liquid species. Manybody polarizability also has a significant influence on ionic liquid properties, and should be incorporated into computation [19, 20]. All of these factors contribute to the computational cost for atomistic simulations of ionic liquids, limiting the simulation length and time, or *scope*, of attainable computation. Consequently, most systems simulated using atomistic molecular dynamics are on the order of nanoscale.

Alternatively, mesoscale-order modeling approaches have been formulated [21] to effectively extend the simulation length and time scale respectively to micrometers and microseconds. For the purpose of modeling systems and calculating typical properties of ionic liquids, an effective method at the mesoscale is *coarse-grained* molecular dynamics (CG-MD). A depiction of the approximate scope of various simulation tools at different length and time scales including the atomistic and coarse-grained methods considered here is shown in Figure 1.1. As the scope travels increasingly through time/length scales, effective simulation tools vary, ranging from subatomic particle physics up to classical continuum mechanics.

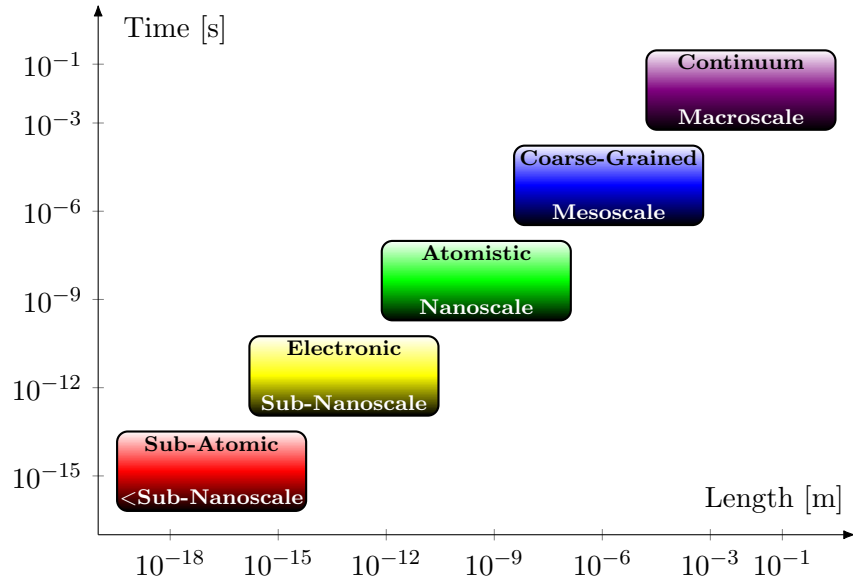


Figure 1.1. Illustration of simulation tool types for the scopes of differing approximate length and time scales.

Coarse-graining of simulated systems involves simplifying models of atoms and molecules by combining them into coarse-grained *sites* reducing the degrees of freedom in the system. Computationally, sites then are treated as particles, just like atoms. Coarse-grained models retain the overall shape and formation of molecular structures, and are known to retain structural and thermodynamic properties when compared to their reliable atomistic counterparts. However, transport properties of coarse-grained systems are known to be generally incorrect. During coarse-graining, the reduction in degrees of freedom eliminates much of the effective friction between coarse-grained sites, making the dynamics artificially fast.

To overcome this problem, Markutsya and Lamm developed the *probability distribution function coarse-graining* (PDF-CG) method, whereby the correct dynamics of the coarse-grained system are implemented through hydrodynamic interactions [23]. By this method, hydrodynamic interactions are derived from the all-atom degrees of freedom

during the coarse-graining procedure. During their work, the method was tested and proven to accurately predict correct dynamics for a system of water molecules, and a water-glucose solution. Thus, a coarse-grained system rigorously derived from an all-atom reference system can retain the correct structure and dynamics while simulating more atoms for a longer amount of time. In the present work, such methodology is applied to ionic liquids of interest. The methods are proven to produce structure and dynamics in agreement with reliable reference systems, and the coarse-grained models are then used to successfully simulate and analyze interfacial phenomena; specifically, at the liquid-vacuum interface.

## 2 Theory

### 2.1 System Trajectories and Averages

Quantitatively speaking, the goal of molecular simulations is to predict properties of the system. Properties are calculated based on the states that a system progresses through. In the near-mesoscale and nanoscale scopes considered here for ionic liquids, states are defined by the momenta  $\mathbf{p}$  and positions  $\mathbf{r}$  of each  $N$  particles in the system, also known as the *trajectory*. The momentum is simply:

$$\mathbf{p} = \mathbf{m} \cdot \mathbf{v}(t) \quad (2.1)$$

Where  $\mathbf{m}$  is the array of particle masses, and  $\mathbf{v}(t)$  is the particle velocity vector. Hence, properties here will simply be found as a result of the trajectory averaged in time. However, as discussed by Leach [24], calculating properties using the exact time average is not feasible in systems of this scope, as it requires integrating the property as a function of all momenta and positions, which themselves are functions of time. Instead, a more practical approach is to implement statistical mechanics and use the *ensemble average*, calculated as:

$$\langle A \rangle = \int \int d\mathbf{p}d\mathbf{r} A(\mathbf{p}, \mathbf{r}) \rho(\mathbf{p}, \mathbf{r}) \quad (2.2)$$

For any general property  $A$ , where  $\rho(\mathbf{p}, \mathbf{r})$  is the probability density of the ensemble. Indicated by use of the arrow brackets, the ensemble average calculates the property's value over a finite number of replications. Such a method of averaging is validated in accordance with the *ergodic hypothesis*, in which case the time average is said to be equal to the ensemble average. In general, any property calculation can be unique depending on the ensemble constraints applied. In the realm of molecular dynamics, these constraints appear prominently as imposed constants when advancing time steps. While there are many ensembles used for different types of computer simulation, only two are applied first-handedly in this work. They are described, along with their application here, in Table 2.1. The ensemble average appears in this work not only when performing simulations, but also in post-processing to effectively calculate other properties during analysis. In application, this means dividing simulations into smaller independent durations in time and averaging data over each.

### 2.2 All-atom Molecular Dynamics

Molecular dynamics, by definition, is a *deterministic* method, meaning that all of the future states of the system can be calculated from the current state. Time steps in the

Table 2.1. The two ensembles first-handedly applied in this work [24].

Name	Conditions (Constants)	Application
Canonical	$N, V, T$	Conventional CG-MD
Microcanonical	$N, V, E$	PDF-CG-MD

system are advanced by applying the Newtonian equation of motion:

$$\mathbf{m} \frac{d\mathbf{v}(t)}{dt} = \mathbf{F}(\mathbf{r}). \quad (2.3)$$

Where  $\mathbf{F}(\mathbf{r})$  is the vector of particle resultant force. If a force between every pair of particles is defined at any particular time step, then velocities at the successive step can be calculated, and positions updated. Naturally, then, defining the force is crucial, and the developed force between all present pairs of particles is called the *force field*. However, until the Newtonian equation is applied, this is often represented alternatively by the potential energy ( $U$ ) between all particle pairs. These quantities are easily related through the equation:

$$\mathbf{F}(r) = -\frac{dU(r)}{dr} \quad (2.4)$$

Which describes the pairwise force or potential energy for any two particles. There are two distinctive components of all potential energy in a molecular dynamics system: *bonded* and *non-bonded*. In equation form this is simply:

$$U = U_b + U_{nb}. \quad (2.5)$$

For the  $U_b$  term, there are three bond types which can be present for any pair of bonded sites: (i) *Bonds* between adjacent sites, (ii) *Angles* between sites with another single bonded site located in-between the pair, and (iii) *Dihedrals* between sites with another two bonded sites in-between the pair. By constraining these three terms, the bonded structure is defined. A common choice of bonded potential for ionic liquids contains harmonic terms for the bonds and angles, and a cosine term for dihedrals [21, 25]:

$$U_b = \sum_{\text{bonds}} k_b (r_b - r_{b,0})^2 + \sum_{\text{angles}} k_a (r_a - r_{a,0})^2 + \sum_{\text{dihedrals}} k_d [1 + \cos(\eta_0 r_d - \delta_0)] \quad (2.6)$$

Where  $r_b, r_a$  and  $r_d$  are the bond, valence angle and dihedral angle distances, respectively,  $k_b, k_a$  and  $k_d$  are force constants, while  $r_{b,0}, r_{a,0}, \eta_0$  and  $\delta_0$  are equilibrium positions. It should be noted that the angle and dihedral type coordinates here and in this work are defined by distances as opposed to angular measurements, which are simply related by triangulation.

The non-bonded potential  $U_{nb}$  is composed of short range van der Waals interactions  $U_{VDW}$ , and for the presence of Coulomb interactions, the long-range term  $U_{el}$ , totaling:

$$U_{nb} = U_{VDW} + U_{el}. \quad (2.7)$$

Van der Waals interactions are commonly implemented using the Lennard-Jones potential form with 12-6 exponents:

$$U_{VDW} = \sum_{i=1}^{N-1} \sum_{j=i+1}^N 4\varepsilon_{ij} \left[ \left( \frac{\sigma_{ij}}{r_{ij}} \right)^{12} - \left( \frac{\sigma_{ij}}{r_{ij}} \right)^6 \right] \quad (2.8)$$

With  $r_{ij}$  being the distance between atom  $i$  and  $j$ , while  $\varepsilon_{ij}$  is the energy minimum depth, and  $\sigma_{ij}$  is the minimum distance of energy. Regarding the Coulomb interactions, the charge  $q_k$  on any unique atom  $k$  of the ions must be found, for example, through ab initio quantum mechanics. Then, the Coulomb interactions can be written as:

$$U_{el} = \sum_{i=1}^{N-1} \sum_{j=i+1}^N \frac{q_i q_j}{r_{ij}} \quad (2.9)$$

At this point, most force fields for atomistic systems are developed. However, an additional concern for the study of ionic liquids is induced dipoles. As shown by Yan et. al [19], these have a significant effect on the behavior of ionic liquid systems. Therefore, polarizable force field modifications are a necessity for this class of fluids.



## 2.3 Coarse-grained Molecular Dynamics

In the context of molecular dynamics, coarse-graining generally involves two steps: (1) Choose CG models by simplifying the atomistic model by combining atoms into sites, and (2) develop force fields for the newly CG models, ensuring they will still predict desired properties. When grouping atoms, sites are located at the center of mass (CoM) of the grouped atoms, with mass and charge equal to the sum from the group. Once coarse-grained models are constructed by strategically performing this grouping, the force fields to be applied are the critical factors at hand. Force fields are developed such that the CG retains properties of the reference system, because CG-MD time steps are then advanced using the average CG force. For example, properly developed CG force fields for ionic liquids will retain the effect of long-range electrostatic interactions if its reference system implemented them.

Three notable methods used to derive coarse-grained force fields (or potentials) are: (i) Fitting of the system’s free energy [26, 27], (ii) structurally-focused reproduction of an anticipated target structure [28–31], and (iii) the force matching approaches, in which coarse-grained forces are fitted to those from all-atom simulations [32–35]. The force matching method generally comes with the benefit of less computational cost in developing the fields. Wang et. al [21] discussed that bonded fields developed with force matching will scale with changes in temperature, but non-bonded fields won’t necessarily do so. Therefore, the present work uses Boltzmann inversion (a structurally-focused method) and fitting of harmonic oscillator potential (HOP) functions [28, 36, 37] to develop bonded force fields, and the multi-scale coarse-graining (MSCG) method with force matching for those that are non-bonded. In-depth discussion of these two methods can be found in the cited literature, but their application in this work is outlined in Chapter 3.

## 2.4 The Probability Distribution Function Coarse-graining Method

As outlined previously, effective methods exist for producing coarse-grained models of ionic liquids which accurately reproduce structure. Such models provide the advantage of increased efficiency when sampling phase space, but have the disadvantage of inaccuracy for time-dependent properties [21, 38]. This represents a significant problem in any situation where dynamical properties are of importance. To regain accurate dynamics, non-bonded interactions must be modified, slowing down the system. Markutsya and Lamm [23] developed a formalized approach beginning with the multidimensional Langevin equation [39] from the generalized Langevin equation (GLE):

$$\mathbf{m} \frac{d\mathbf{v}(t)}{dt} = \mathbf{F}(\mathbf{r}) - \boldsymbol{\zeta}\mathbf{v}(t) + \boldsymbol{\eta}(t) \quad (2.10)$$

With  $\mathbf{m}$  being the particle mass diagonal matrix vector,  $\mathbf{r}$  are the generalized coordinates,  $\boldsymbol{\zeta}$  is the friction tensor,  $\mathbf{v}$  is the velocity vector,  $\mathbf{F}$  is the vector of force exerted on CG sites due to potential energy from interaction with other CG sites, and  $\boldsymbol{\eta}$  is the noise vector. During their work, they implemented hydrodynamic interactions which are scaled by a constant coefficient characteristic time  $\Delta t_0$ . The PDF-CG method differs from conventional CG methods because it extracts the full probability distribution function of forces which are available during the coarse-graining process. It is from this extraction that the previously ignored hydrodynamic interactions are implemented. The final equation, in vector form, is:

$$\mathbf{m} [\mathbf{v}(t + \Delta t) - \mathbf{v}(t)] = \mathbf{F}(\mathbf{r})\Delta t + \mathbf{F}_0(\mathbf{r})\mathbf{N}(0, 1)\sqrt{\Delta t_0\Delta t} + \frac{\mathbf{F}_0(\mathbf{r})\mathbf{F}_0(\mathbf{r})\mathbf{v}(t)}{2k_B T_{ref}}\Delta t_0\Delta t \quad (2.11)$$

Where  $\mathbf{N}(0, 1)$  is the vector of random numbers generated with the standard normal distribution, and  $\mathbf{F}_0(\mathbf{r})$  is a standard deviation matrix for the random term. Because general systems have multiple CG site types, this is applied in component form as:

$$m_i [v_i(t + \Delta t) - v_i(t)] = F_i(r)\Delta t + \sum_j F_{0,ij}^{\mathcal{A}_i,\mathcal{A}_j}(r_{ij})\sqrt{\Delta t_0^{\mathcal{A}_i,\mathcal{A}_j}}\Delta t N_j(0, 1) \\ + \frac{1}{2k_B T_{ref}} \sum_j \sum_k F_{0,ik}^{\mathcal{A}_i,\mathcal{A}_k}(r_{ik})\sqrt{\Delta t_0^{\mathcal{A}_i,\mathcal{A}_k}} \times F_{0,kj}^{\mathcal{A}_j,\mathcal{A}_k}(r_{kj})\sqrt{\Delta t_0^{\mathcal{A}_k,\mathcal{A}_j}}v_j(t)\Delta t \quad (2.12)$$

Where  $\mathcal{A}_i$  and  $\mathcal{A}_j$  represent types of  $i$ th and  $j$ th CG sites. Hence, the aforementioned characteristic time written as  $\Delta t_0^{\mathcal{A}_i,\mathcal{A}_j}$  and the standard deviation matrix components  $F_{0,ij}^{\mathcal{A}_i,\mathcal{A}_j}$  will be different for different CG type pairs. This original derivation, however, assumes a direct correlation between the friction and noise components in  $\Delta t_0$ . Consider the following version of Equation 2.11, where these two components are disconnected from  $\Delta t_0$ :

$$\mathbf{m} [\mathbf{v}(t + \Delta t) - \mathbf{v}(t)] = \mathbf{F}(\mathbf{r})\Delta t + \beta\mathbf{F}_0(\mathbf{r})\mathbf{N}(0, 1)\sqrt{\Delta t} + \alpha\frac{\mathbf{F}_0(\mathbf{r})\mathbf{F}_0(\mathbf{r})\mathbf{v}(t)}{2k_B T_{ref}}\Delta t \quad (2.13)$$

Making  $\beta$  a scaling factor for the noise component, and  $\alpha$  that for the friction component. By the original derivation, then:

$$\beta = \sqrt{\Delta t_0}, \quad \alpha = \Delta t_0 \quad (2.14)$$

By instead applying Equation 2.13, while no longer assuming Equation 2.14, this direct correlation in  $\Delta t_0$  is no longer assumed, and two empirical coefficients must be found (by an almost identical process, however). As shown by Equation 2.12, the terms  $\alpha$  and  $\beta$  will still be different for various CG pairs, and must be empirically determined for each.

Commonly, molecular dynamics simulations advance in time governed by the NVT ensemble, but as Markutsya and Lamm [23] discussed after derivation of Equation 2.12, this calculation during time steps actually serves as a Langevin thermostat. Therefore, all PDF-CG method-based simulations needn't be explicitly progressed by monitoring temperature, and those in this work were instead constrained by the NVE ensemble.

### 3 Methods

In this chapter, the theory previously presented is applied to two ionic liquid chemical pairs, each of which compose the systems of interest for this work. The goal, as with any implementation of molecular modeling, is to compute the properties of systems at hand, and give insight into their behavior on the molecular level [25]. Because all first-hand methods and results compiled in this this work are computational, reference systems for development of models are applied in order to ensure real-world accurate results. The word “calibration” is used frequently in this chapter, emphasizing that force field parameters are tuned and adjusted so that coarse-grained models behave in a manner as similarly to the all-atom reference system as possible.

Two sets (one pair per set) of ionic liquids were selected in particular due to the variable range of ion size, to demonstrate the capabilities of methods employed, and also because of their stability against Lithium metal and graphite anodes, which pose as a valuable potential application [6–8, 40, 41]. These are (a) *N*-methyl-*N*-butylpyrrolidinium bis(trifluoromethylsulfonyl)-imide ([pyr14][TFSI]) and (b) 1-ethyl-3-methylimidazolium boron tetrafluoride ([EMIM][BF<sub>4</sub>]), shorthand-denoted with the cation component of the pair, followed by the anion. For convenience, each set will be referred to using their shorthand notation for the remainder of this work. Graphical representations showing molecular structure of these two ionic liquids can be seen in Figure 3.1. What follows is description of an all-atom system of reference utilized, the coarse-graining process of the molecular structures, and implementation of the PDF-CG method to simulate the coarse-grained system.

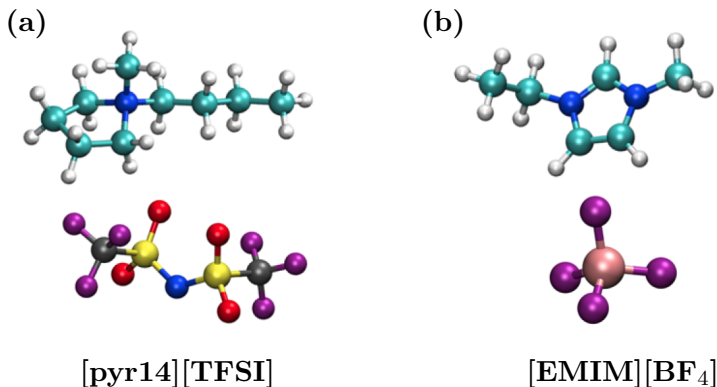


Figure 3.1. Representation of the two ionic liquids considered for this work: (a) *N*-methyl-*N*-butylpyrrolidinium bis(trifluoromethylsulfonyl)-imide ([pyr14][TFSI]) and (b) 1-ethyl-3-methylimidazolium boron tetrafluoride ([EMIM][BF<sub>4</sub>]) (Adapted from [20]).

#### 3.1 All-atom Reference Systems

All-atom molecular dynamics simulation reference data was obtained from ionic liquid investigative work performed by Haskins et al. [20]. During a portion of their work, separate all-atom molecular dynamics simulations containing the aforementioned ionic

liquids were performed. To parameterize the potential energy for each liquid, they implemented the Atomistic Polarizable Potential for Liquids, Electrolytes and Polymers (APPLE&P) force field in the form parameterized by Borodin and co-workers [42–44] to gain the ability of including self-consistent atomic polarization of the highly polarizable atoms in the ionic liquids. As with many other force-fields explicitly designed for ionic liquid simulation [45, 46], this one was chosen to provide accurate results for thermodynamic and transport properties. Simulations were integrated with a 3-2-1 reversible reference propagation algorithm (rRESPA). Calculations were constrained by multiple temperatures. However, this work focuses on two specified temperatures of  $T_{hi} = 363$  K and  $T_{lo} = 298$  K with ambient pressure ( $P$ ) using the Nosé-Hoover [47, 48] thermostat and barostat. Consecutive data was found using a 3 fs time step for long-range charge and dipole interactions, 1.5 fs time step for local charges, and 0.5 fs time step for bonds, angles, and the improper dihedrals [20]. The cutoff radius employed for non-bonded interactions was 12 Å for the [pyr14][TFSI] liquid, and 11 Å for [EMIM][BF<sub>4</sub>]. Each of the sets of ionic liquids considered here composed their own system, and differed in the size of the box-shaped volume containing the liquids, the number of ion pairs present, and the non-bonded interaction cutoff radius. These parameters for each system are displayed in Table 3.1. Visualizations depicting the all-atom reference systems can be found in Figures A.1-A.2 of the Appendix, in which the cation and anion components are represented separately for clarity. From this work, a basis set of data including

Table 3.1. Parameters of all-atom reference systems utilized in this work.

Ionic liquid	Box size (Å)	Number of ions
[pyr14][TFSI]	$42.4432 \times 42.4432 \times 42.4432$	144 pairs
[EMIM][BF <sub>4</sub> ]	$40.6538 \times 42.0393 \times 33.7086$	216 pairs

bonded distributions, radial distribution functions and diffusion coefficients were gathered and noted. This basis data provided reference for development of the CG systems to be described, and also a standard of realistic system behavior with which to conform the CG system. The goal, then, when developing the CG systems, was to match the properties of corresponding all-atom systems as closely as possible.

## 3.2 Construction of Coarse-grained Models

In this section, development of a coarse-grained (CG) model for simulating the ionic liquids at hand is outlined. To begin construction of the CG models, atoms represented in the all-atom models were combined into CG sites. Atoms to be combined were selected, and one CG site of their total mass and charge could be placed at the CoM of the combined atoms. This was done as to not significantly displace masses or charges, while simultaneously acknowledging that the CG sites will produce significantly less friction than the more numerous atoms in the all-atom model [21]. Both the cation and anion’s structures were divided into sites for each ionic liquid set, with a site combining anywhere between 1 and 12 atoms. In the case of symmetry or replicated bonded structures, duplicate sites of the same type were implemented, namely in the case of the [TFSI]<sup>−</sup> anion. Diagrams depicting the CG site construction of the ionic liquids can be seen in Figures 3.2-3.3. These diagrams assign a type number to each distinct site which will be used for denotation during the remainder of this work. A table depicting the elemental components of each CG site, in addition to their masses and charges can be seen in Tables A.1-A.2 of the Appendix.

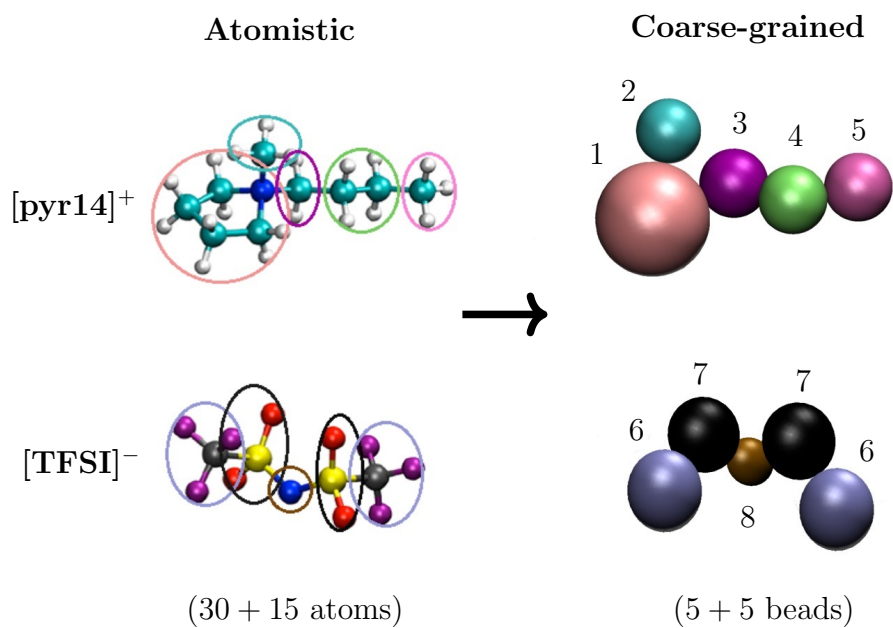


Figure 3.2. Coarse-grained sites of the  $[\text{pyr14}][\text{TFSI}]$  ionic liquid.

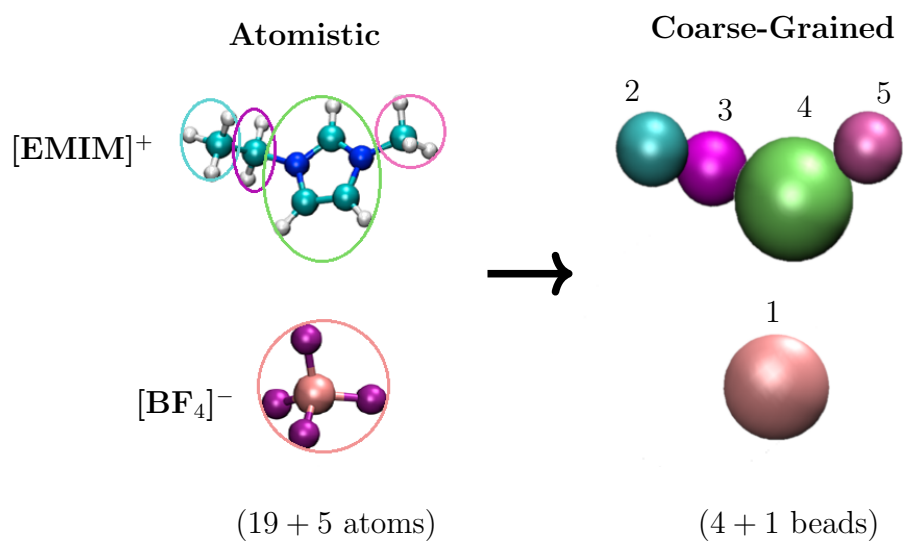


Figure 3.3. Coarse-grained sites of the  $[\text{EMIM}][\text{BF}_4]$  ionic liquid.

### 3.3 Coarse-grained Structure Calibration

The next step in developing the CG systems of ionic liquids was to construct and validate force fields which ensure accurate structural behavior. All systems implemented regarding structure (from this point until Section 3.4) utilize conventional CG simulation procedures, and will only diverge from conventional procedures when the dynamics are considered. The structure is composed of two parts: *bonded* and *non-bonded*. Therefore, this section will be split into two parts. First, though, the sample systems implemented for calibration must be described.

**Structure Calibration Systems** These were initially ran using the force field derived from the reference systems, the bonded component composed of the initial guess found in Section 3.3.1, and the non-bonded component which was found in Section 3.3.2. They were prescribed periodic boundary conditions in all directions, emulating *bulk* of fluid. To save computational cost, these systems were small in total CG sites and ran for a short amount of time relative to the computational power of the machine used. Also, the systems were made to reflect the all-atom reference systems closely in size for ease of transition and simplicity. They advanced time steps with the average pairwise CG force and Newtonian equation of motion (Equation 2.3), and were performed using the Large-scale Atomic/Molecular Massively Parallel Simulator (LAMMPS) [49], under the constraints of an NVT ensemble, ran at two specified temperatures of  $T_{hi} = 363$  K and  $T_{lo} = 298$  K, utilizing the Nosé-Hoover [47, 48] thermostat. Ionic liquid pairs were placed inside of a box of varying side lengths with initial conditions representative of predicted equilibrium positions. Besides realistic positioning of sites to emulate the bulk fluid, velocities were chosen and scaled to the specified temperature, and the system was always allowed to equilibrate from initial conditions before calibration was performed. To reflect the reaching effects of long distance interactions accurately, the cutoff radius used here was similar to that of the reference systems, at 11 Å. The time step was 4 fs, which was significantly longer than the largest used by collaborators when simulating the reference systems [20]. This is because CG simulations act across larger time/length scales, meaning that less fineness in time steps is not required to maintain accurate behavior of the models. The time step used here was also verified independently in simulations before full implementation. Finally, configurations and force data were saved every 1 ps to provide sufficient sampling for the analysis to be discussed. Table 3.2 shows parameters which varied between the sets of ionic liquids. Figures A.3-A.4 of the Appendix depict visualizations of the structure calibration systems, with cation and anion components shown again independently. Also, the CG sites shown are shrunk in size with artificial bonds depicted between bonded sites for clarity, as opposed to the depictions found in Figures 3.2-3.3 where the CG process was implemented.

Table 3.2. Varied parameters of the structure calibration systems.

Ionic liquid	Box size (Å)	Number of ions
[pyr14][TFSI]	$42.4432 \times 42.4432 \times 42.4432$	144 pairs
[EMIM][BF <sub>4</sub> ]	$40.6538 \times 42.0393 \times 33.7086$	216 pairs

#### 3.3.1 Bonded Structure Calibration

**The Bonded Distribution** The relevant property used for quantifying bonded structure was the *bonded distribution*, denoted  $b(r)$ . This is a normalized probability-distribution function, depicting the probability of finding any specific bonded pair of sites at a par-

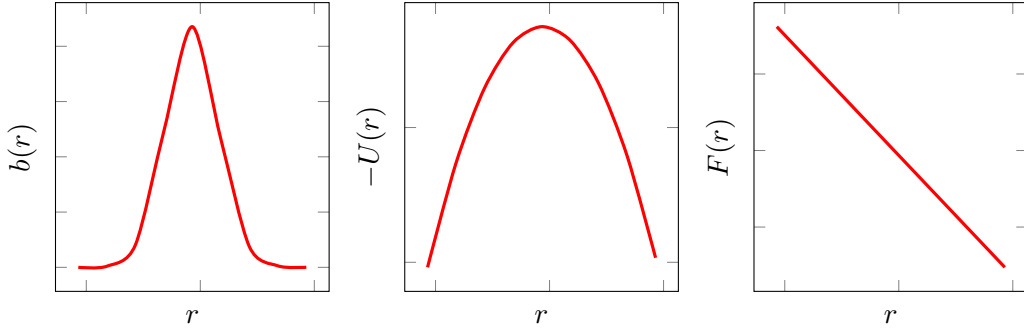


Figure 3.4. Typical Boltzmann inversion process:  $b(r) \rightarrow -U(r) \rightarrow F(r)$ .

ticular radial distance from one another. The bonded structure of the ions modeled here was constrained in all degrees of freedom (DoF's) by providing force fields  $F(r)$  for each present pair of these bonded types.

**Boltzmann Inversion** To begin, the reference all-atom bonded distributions had to be generated. To do so, the positions of all  $N$  CG sites were calculated as the CoM's of grouped all-atom positions, by computing:

$$\bar{\mathbf{r}}_{\text{site}} = \frac{\sum_{i=1}^{n_a} m_i \mathbf{r}_i}{\sum_{i=1}^{n_a} m_i} \quad (3.1)$$

For each site, where  $n_a$  is the number of atoms in the site,  $m_i$  is the mass of the  $i$ th atom of the site, and  $\mathbf{r}_i$  is the position vector of each  $i$ th atom. This provided the “ghost” positions of the CG sites in the all-atom systems. Bonded distributions at each discrete radial interval bin of size  $\Delta r$  were then calculated by counting the number of bonds in each bin through space and time, which was normalized by taking the ensemble average. Once these all-atom bond distributions were calculated, they were applied for two purposes: As the reference with which to match the bonded distributions of the CG system, and also to derive the initial guess for iterative matching. The initial guess was derived using Boltzmann inversion [28, 36, 37] as follows. The potential energy was found as:

$$U(r) = -k_B T \ln b(r) \quad (3.2)$$

For any particular bonded pair, where  $k_B$  is the Boltzmann constant,  $T$  is the constrained temperature, and  $b(r)$  is the bonded distribution probability as a function of bond radius. Usually, this reference potential energy is fit with an approximation matching a respective term (bond, angle or dihedral) from equation 2.6. A diagram of this typical process can be seen in Figure 3.4. However, a couple of obstacles hindered such a direct implementation.

**Harmonic Oscillator Potential Fitting** To illustrate the problems at hand, Figure 3.5 shows three bonded distributions. Although such issues were present for both ionic liquids in this work, all-atom reference distributions from [pyr14][TFSI] are used as examples. First shown is the 6-7 bond type distribution, which in form is typical to the bonded distributions of any atomistic molecular dynamics environment. In other words, the potential energy correlating to this distribution (found through Equation 3.2) is easily fit with a harmonic oscillator potential (HOP), as in the first two terms of Equation 2.6. Keeping in mind, though, that these represent desired coarse-grained

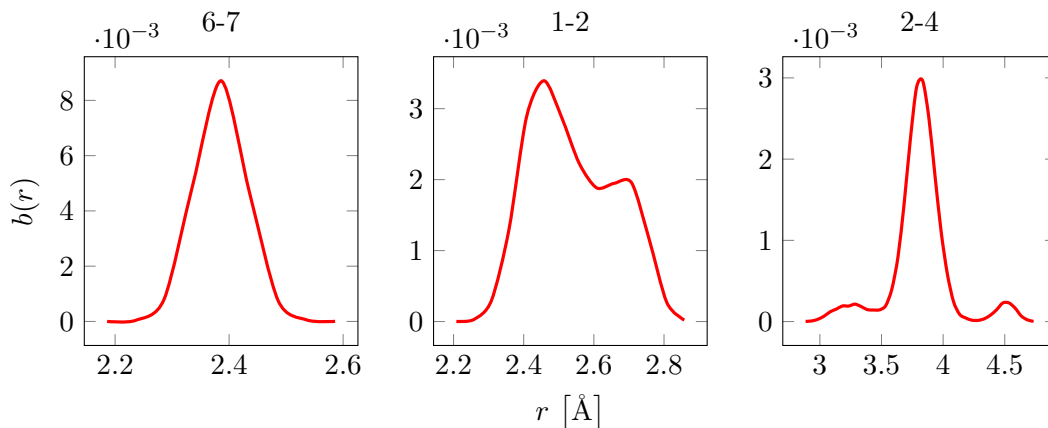


Figure 3.5. Example all-atom reference bonded distributions of the [pyr14][TFSI] ionic liquid: a bond-type (left), angle-type (middle), and dihedral-type (right).

structures. Due to the extended bonded configuration possibilities that coarse-grained models produce, however, such simple fits are not always achievable. Often times, there exists multiple peaks in a distribution, especially for dihedral types. For example, in the dihedral-type bonded structures presented by Wang et. al [21], two symmetric peaks existed for the coarse-grained model. Shown secondly in Figure 3.5 is the 1-2 bond type distribution, and lastly is the 2-4 dihedral type. As is clearly seen, these structures produce multiple peaks, and in addition, are asymmetric. This presents a notable problem when accurately fitting their associated potential energy using the form of Equation 3.2. To approach this issue, multiple HOPs were fit where more than one distribution/potential energy peak existed. Where this was done, smooth transitions were added between the functions. If necessary, this was done for all types of bonded distributions, including dihedrals. Since the all-atom bonded distributions of all dihedrals considered here effectively contained more than one peak, this resulted in no use of the cosine term mentioned in Equation 2.6. Hence, the bonded potential energies here were approximately:

$$U_b = \sum_{\text{bonds}} k_b(r_b - r_{b,0})^2 + \sum_{\text{angles}} k_a(r_a - r_{a,0})^2 + \sum_{\text{dihedrals}} k_d(r_d - r_{d,0})^2 \quad (3.3)$$

Which terms were piecewise for any distribution with multiple peaks. Once this was accomplished, the derivative of potential energy was found, producing the force for that pair as per Equation 2.4. This was calculated for every bonded pair and every radius increment at which an all-atom bonded distribution probability was produced. Hence, an initial guess force-field was generated, with which to start iterative calibration. The bonded structure calibration system was then run, starting with simulation time lengths of 1ns after equilibration. All bonded distributions were calculated using a radius discretization of  $\Delta r = 0.025 \text{ \AA}$ . In every iteration, the system would be run, the CG bonded distributions would be calculated, and the force-field would be manually adjusted to improve the all-atom reference match. For example, if a bond showed a lower probability of existing at a higher radius, the force for that bond in the vicinity of such a radius would be decreased, allowing the bond to exist there at a higher probability. As the match increased in accuracy, simulation time length was increased to provide more data samples, and thus improve the precision of the bonded distributions. This was repeated until a sufficiently close match was found, and the bonded structure calibration was complete.



### 3.3.2 Non-bonded Structure Calibration

**Force Matching** Non-bonded CG force-fields were derived based on the respective all-atom reference systems using the multi-scale coarse-graining method with force matching [32–35]. Again, the positions of each  $N$  coarse-grained sites are given from the all-atom reference system calculated earlier by Equation 3.1, and the net forces  $\mathbf{F}_i^{\text{ref}}$  acting on them are computed. The net force on any particular CG site  $i$  is due to the sum of all the effective forces between the pairs of CG sites, giving the function:

$$\mathbf{F}_i^{\text{ref}} = \sum_{j=1}^N \mathbf{f}_{ij}(\mathbf{r}_i, \mathbf{r}_j, g_1, g_2, \dots, g_k) \quad (3.4)$$

Where  $\mathbf{f}_{ij}$  is defined as the force on the  $i$ th CG site due to the  $j$ th CG site. Since  $\mathbf{f}_{ij}$  is not known analytically, cubic splines are chosen to write each pairwise force as a function of  $k$  unknown parameters  $(g_1, g_2, \dots, g_k)$ . Since  $N > k$ , the resultant system of equations is over-determined, and was solved using the singular value decomposition (SVD) method [50]. All of the atomistic configurations were split into equally-sized blocks and SVD was applied to each. The CG force versus radial separation was obtained by averaging outcomes of all the blocks.

**The Radial Distribution Function** In the same way that the bonded structure of each ionic liquid was verified by comparison of the quantitative bonded distribution, the non-bonded structure considered in this sub-section utilized the *radial distribution function* (RDF), denoted  $g(r)$ . This quantity is a non-normalized probability-distribution function which depicts the probability of finding a pair of particles, or group of particles, at a certain radial distance from one another. In other words, it describes how density varies as a function of distance from a reference particle or group of particles. For the purposes of this work, the groups of particles examined were individual ions. Due to their pairwise composition, there were only three radial distribution functions required for each type of ionic liquid: Comparing the cation to the cation (++) , the cation to anion (+-) (or vice-versa), and the anion to anion (- -). The non-bonded structure of the CG systems was compared and validated, then, by these three functions. The structure calibration system was run for 1ns after equilibration to gain enough phase space samples for calculation of RDF’s. The RDF’s of the all-atom reference and CG systems both again required a version of Equation 3.1, modified for calculating the CoM’s of each ion, as opposed the their individual CG sites:

$$\bar{\mathbf{r}}_{\text{ion}} = \frac{\sum_{i=1}^{n_s} m_i \mathbf{r}_i}{\sum_{i=1}^{n_s} m_i} \quad (3.5)$$

For each ion, where  $n_s$  is the number of sites in the ion,  $m_i$  is the mass of the  $i$ th site of the ion, and  $\mathbf{r}_i$  is the position vector of each  $i$ th site. Once the CoM position of each ion was found, pairs of ions at certain discrete radial distances could be numbered in distance bins of size  $\Delta r = 0.025 \text{ \AA}$  (for sufficiently smooth results), producing the non-normalized RDF’s. These calculations were cut off at a radius of  $16 \text{ \AA}$ , which is typical to non-bonded MD analysis, as it provides ample useful neighbor information below the cutoff. This was calculated for each ionic liquid, and comparisons to the all-atom reference system were made to validate accurate non-bonded structure.

### 3.4 Coarse-grained Dynamics Calibration

With force-fields in place which produce accurate structural behavior, the conventional CG model of each system was complete. At this point, conventional coarse-graining processes end, and a CG model is applied to phenomena of interest. In contrast, this work has aimed to further improve CG models by fixing inaccurate dynamics. The rest of this chapter will outline the development of systems simulating the ionic liquids dynamically modified using the PDF-CG method, while comparing with the results of conventional coarse-graining (C-CG) in addition to the all-atom (AA) reference systems. The PDF-CG method, being designed to modify only dynamics, was expected and found to have negligible effect on structure. Hence, the structural behavior of the PDF-CG systems is assumed equivalent to that when ran with C-CG. The dynamics of the C-CG systems, then, was generally much higher than the reference AA ones, and the PDF-CG systems were tuned to match the reliable AA references.

**Dynamics Calibration Systems** To reach the desired size of the systems of application, the structure calibration systems of section 3.3 were each expanded in volume and number of sites eight times. In other words, the systems’ periodic box sizes were multiplied by two in length in the  $x, y$  and  $z$  directions. The new systems were again implemented in LAMMPS, with the similar parameters, aside from the ensemble constraint of NVE, as discussed in Section 2.1. This being the case, initial velocities from the smaller structure calibration system were again scaled to run at the two focus temperatures of  $T_{hi} = 363$  K and  $T_{lo} = 298$  K, and the system was allowed to equilibrate before calibrating. The conditions at the boundary of each box were again periodic (bulk), with a potential cutoff radius of 11 Å. The time step was 4 fs, and configurations were saved every 1 ps. The parameters which varied between ionic liquids were the box size and number of ions in the box. These parameters can be seen in Table 3.3, and visual representations of each of the dynamics calibration systems can be seen in Figures A.5-A.6 of the Appendix.

Table 3.3. Varied parameters of the dynamics calibration systems.

Ionic liquid	Box size (Å)	Number of ions
[pyr14][TFSI]	$84.8864 \times 84.8864 \times 84.8864$	1152 pairs
[EMIM][BF <sub>4</sub> ]	$81.3076 \times 84.0786 \times 67.4172$	1728 pairs

**Coefficient Groupings** To advance time steps, Equation 2.13 was used, as opposed to Equation 2.12, as per the discussion in that section. However, the dynamically-correct  $\alpha$  and  $\beta$  needed to be found for any particular system configuration before the equation could be properly applied. Therefore, calibration systems of the same configuration as those in which the models would be applied had to be generated. This way, sets of coefficients for each CG type pairs could be iteratively determined. Before beginning the iterative process of determining the dynamically-correct coefficients, an assumption was made. Since there was a significant amount of CG site types (up to eight, namely for the case of [pyr14][TFSI]), the amount of available non-bonded pairs was large, totaling 36 for [pyr14][TFSI] and 15 for [EMIM][BF<sub>4</sub>], making these the amount of  $\alpha$  and  $\beta$  coefficients to be found for each ionic liquid. Calibrating dynamics while tuning such a large amount of coefficients independently would be cumbersome. To make the iterative method of dynamics calibration more feasible, then, these pairs were grouped together and assumed equal by their ionic association, producing only three necessary  $\alpha$  coefficients and three  $\beta$  for each ionic liquid:  $\alpha^{++}$ ,  $\beta^{++}$ ,  $\alpha^{+-}$ ,  $\beta^{+-}$ ,  $\alpha^{--}$ , and  $\beta^{--}$

(coefficient pairs between cation-cation, cation-anion, and anion-anion). Table 3.4 notes all of the non-bonded pairs that were grouped to each of the three coefficients by each liquid.

Table 3.4. Non-bonded pair group assumptions for  $\Delta t_0$ .

Ionic liquid	Coefficient group	Non-bonded pairs
[pyr14][TFSI]	$\alpha^{++}, \beta^{++}$	1-1,1-2,1-3,1-4,1-5,2-2,2-3,2-4,2-5,3-3,3-4,3-5,4-4,4-5,5-5
	$\alpha^{+-}, \beta^{+-}$	1-6,1-7,1-8,2-6,2-7,2-8,3-6,3-7,3-8,4-6,4-7,4-8,5-6,5-7,5-8
	$\alpha^{--}, \beta^{--}$	6-6,6-7,6-8,7-7,7-8,8-8
[EMIM][BF <sub>4</sub> ]	$\alpha^{++}, \beta^{++}$	2-2,2-3,2-4,2-5,3-3,3-4,3-5,4-4,4-5,5-5
	$\alpha^{+-}, \beta^{+-}$	1-2,1-3,1-4,1-5
	$\alpha^{--}, \beta^{--}$	1-1

**The Diffusion Coefficient** The comparative property implemented for dynamics was the *diffusion coefficient* ( $D$ ). This was calculated for each ion according to the Einstein relation [51] as:

$$D = \frac{\langle (\mathbf{r}(0) - \mathbf{r}(t))^2 \rangle}{(2d)t} \quad (3.6)$$

where  $\mathbf{r}$  was again found according to Equation 3.5, and  $\langle (\mathbf{r}(0) - \mathbf{r}(t))^2 \rangle$  is the mean-square displacement (MSD) during a time interval  $t$  within a space of dimension  $d$  (here,  $d = 3$ ). To begin the iterative determination of correct coefficients, all-atom reference diffusion coefficients were calculated. The MSD based on the CoM of each ion was calculated for all available data, and a least-squares linear-fit of the MSD versus time was found. The fit's slope was equal to the product of the numerator and  $1/t$  portion of Equation 3.6, namely:  $\langle (\mathbf{r}(0) - \mathbf{r}(t))^2 \rangle / t$ . This result could then simply be divided by  $2d$  to provide the respective diffusion coefficient. The same process could also be applied to the PDF-CG system. To begin, initial-guess values were chosen, and the dynamics calibration system was ran starting with a 1 ns duration after equilibration. After the dynamics calibration system ran and diffusion coefficients were calculated and compared to those of the all-atom data, the coefficients could be modified, and the system ran again to repeat. Since  $\Delta t_0$  has a dampening effect on dynamics according to Equation 2.12, it can be treated as inversely proportional to the diffusion coefficient:

$$\Delta t_0 \sim \frac{1}{D} \quad (3.7)$$

In a similar way, it could be said that  $\alpha$  scales the dampening effect, and  $\beta$  scales random noise, or temperature fluctuations in Equation 2.13 implemented here. When empirically finding the correct coefficients, treatment was then loosely as follows:

$$\beta \sim \Delta T, \quad \alpha \sim \frac{1}{D} \quad (3.8)$$

Where  $\Delta T$  is the magnitude of fluctuation in temperature. However, according to Equation 2.14,  $\alpha$  and  $\beta$  are related. Because of this, their determination required continual modification through iterations. For example, if the PDF-CG anion's diffusion coefficient ( $D^-$ ) was significantly smaller than that of the all-atom system,  $\alpha^{--}$  could be decreased to roughly increase the value of  $D^-$ . After this, stability of temperature would be checked. If fluctuations in temperature greatly exceed those from the C-CG system,  $\beta$  could be decreased. Because of the decrease in  $\beta$ , diffusion likely increased, and the

process could be repeated. Using such reasoning, the preceding process was repeated until  $D^+$  and  $D^-$  were sufficiently close to the all-atom reference values, at which point the duration of the calibration simulations would be increased to gain more sampling. Once the diffusion coefficients matched sufficiently at an acceptable sample size, the sets of coefficients were accepted, and the dynamics of each system was calibrated.

### 3.5 Summary of Calibration

The preceding processes were performed on the calibration systems described at both  $T_{hi} = 363$  K and  $T_{lo} = 298$  K, rendering the systems of both liquids and temperatures calibrated. Hence, all model construction and calibration of parameters for developing the structure and dynamically-accurate CG models was complete. This rendered the models ready for application in varying interfaces, and to observe phenomena of interest. To summarize, Table 3.5 shows the parameters, methods and properties used for calibration to the all-atom reference systems.

Table 3.5. Summary of calibration processes.

Component	Method	Parameter	Property
Bonded Structure	HOP fitting	$U_b$	$b(r)$
Non-bonded Structure	MSCG w/force matching [21]	$U_{nb}$	$g(r)$
Dynamics	PDF-CG [23]	$\alpha, \beta$	$D$

## 4 Results

This chapter contains results of the calibration processes employed in Chapter 3: bonded structure, non-bonded structure and dynamics. The results and commentary provided here should prove that the CG systems developed in this work are accurately derived from their reference systems, and therefore are reflective of reality to the extent that coarse-graining can produce. Most of the results to be referenced are located in the Appendix for flow of text, but examples of data are provided in-text for context.

### 4.1 Bonded Structure

The bonded distributions calibrated for the CG model, and of the all-atom reference system can be found for the [pyr14][TFSI] ionic liquid in Figures A.9-A.12, and for the [EMIM][BF<sub>4</sub>] ionic liquid in Figures A.13-A.14 of the Appendix. For purposes of the current discussion, Figures 4.1 and 4.2 depict example bonded distributions sampled from the results. Shown are the bond, angle and dihedral-type distributions respectively, first at the elevated temperature of 363K, then at 298K. For the case of 298K, the CG bonded distribution results are compared against the all-atom reference system at 363K due to unavailability of data at room temperature. This was deemed an acceptable comparison, as bonded structure is minimally affected by temperature because bonded force fields are significantly stronger.

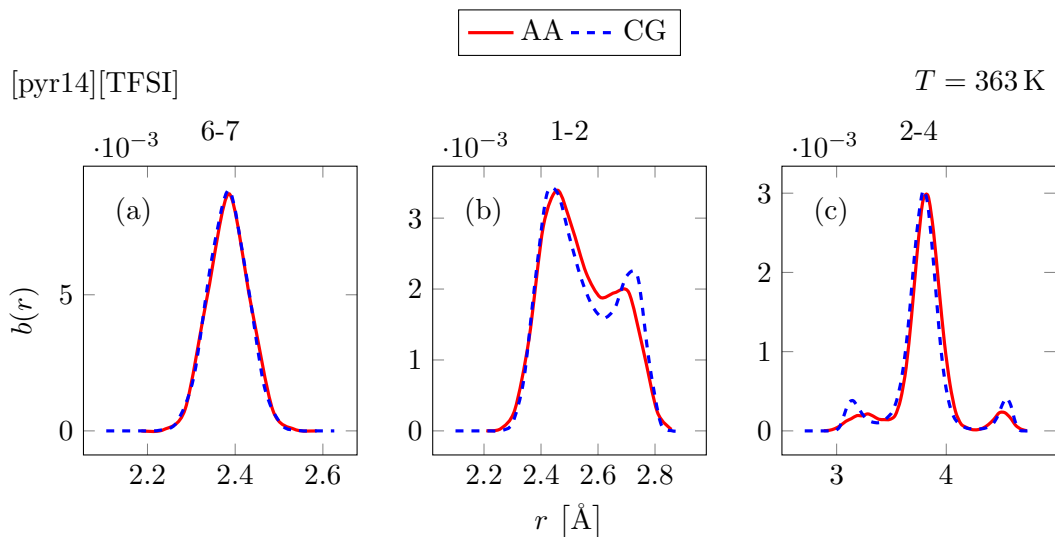


Figure 4.1. Example [pyr14][TFSI] bonded distribution results, bond (left), angle (middle), and dihedral (right)-types, sampled from  $T = 363\text{K}$ .

**Peak/trough Locations** For the purposes of developing these bonded distributions and for comparing results, it is worth noting that emphasis was placed on matching *locations* ( $r$ ) of peaks and troughs, as opposed to their *magnitudes* ( $b$ ). Since the bonded distribution is a normalized probability, a peak/trough that matches loosely in mag-

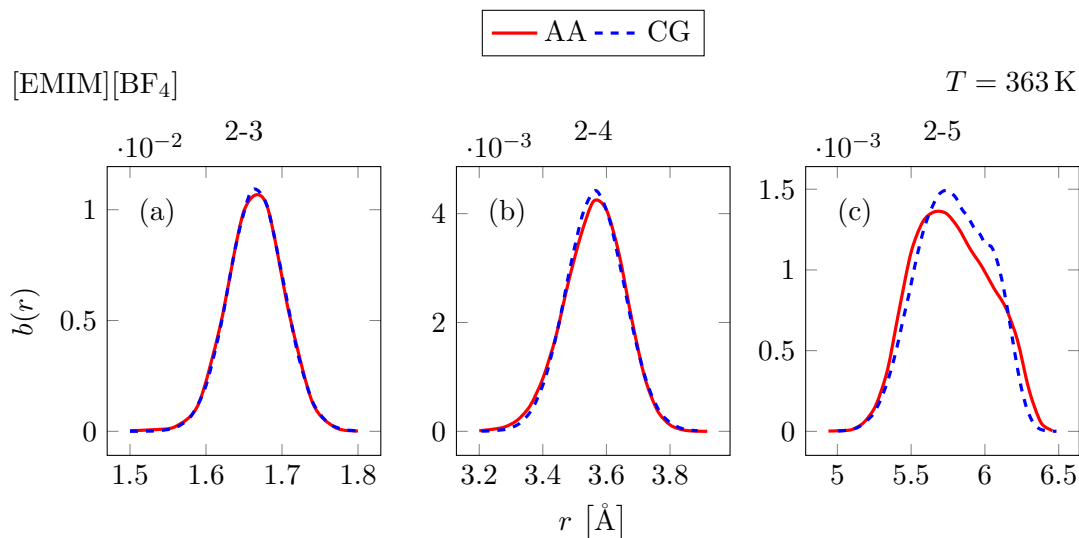


Figure 4.2. Example [EMIM][BF<sub>4</sub>] bonded distribution results, bond (left), angle (middle), and dihedral (right)-types, sampled from  $T = 363\text{K}$ .

nitude, but precisely in location will produce bonds at the correct structural radii (on average).

**Treatment of Multiple Peaks** At first glance, it is seen that symmetric, single peak distributions of the coarse-grained models had relatively accurate fits to the all-atom reference. These fits were quickly achieved, as the associated all-atom potential energies (Equation 3.2) were well represented as harmonic oscillators, which then produced a simple linear force-distance relation (Equation 2.4). The difficulty, then, was found when approaching reference distributions that were asymmetric (e.g. Figure 4.1b,A.9a) and/or contained more than one peak (e.g. Figure 4.1c,A.10g). Treatment of these two conditions was similar in approach, as asymmetry seemed to be caused by the presence of non-prominent concavity changes.

**Fits Achieved** In some of these cases, the precise magnitude and location of secondary/tertiary peaks and/or asymmetries was difficult to match, which should be attributed to the loss of DoF's inherent to coarse-graining. When this dilemma was encountered, focus was given instead to matching the distribution endpoints, such that the range of bond existence at certain radii was preserved. This occurred mostly when calibrating dihedrals, such as in the case of [EMIM][BF<sub>4</sub>]. However, the pyrrolodinium ring and anion size of [pyr14][TFSI] allowed secondary peaks to appear even in the bond and angle-types (1-2, 1-3, 3-5 and 6-8), precluding a tertiary peak of the dihedral type (2-4). Nonetheless, it can be seen that the location of most peaks also match, causing the majority of high-probability radii to match the all-atom reference. For [EMIM][BF<sub>4</sub>], all but one of the cation's bonded distributions had a single peak, despite presence of the imidazolium ring. Its dihedral (2-5), though, contains a sharp change in concavity on the positive side, indicating a minor configuration alteration which was available between the end-sites. This was the most difficult bonded distribution to replicate, as can be seen by the accurate fit on the positive side.

## 4.2 Non-bonded Structure

Radial distribution functions can be seen for the [pyr14][TFSI] and [EMIM][BF<sub>4</sub>] ionic liquids in Figures A.15 and A.16 of the Appendix respectively, depicting results at 363K and 298K. For completeness, non-bonded force fields are included in this document in addition to radial distribution functions. The complete force fields developed for each ionic liquid, sampled for the case of 363K, can be seen in Figures A.17-A.19. Also, Figure 4.3 depicts three example force sets sampled from the [pyr14][TFSI] liquid at 363K. Most depict a convergence towards zero force near 11 Å, justifying the value chosen as a cutoff radius for this work. These show the wide range of complex non-bonded site-site interactions generated by the MSCG method which are required to produce accurate non-bonded behavior, ranging from inverse-type functional form (Figure 4.3a) to decaying radial oscillation (Figure 4.3b), and others (Figure 4.3c).

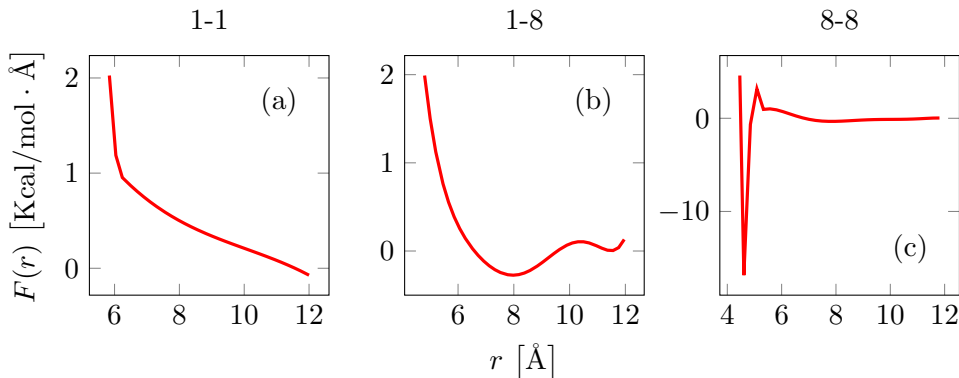


Figure 4.3. Example non-bonded force fields, depicting results for a cation-cation (left), cation-anion (middle) and anion-anion (right)-type, sampled from the [pyr14][TFSI] ionic liquid at  $T = 363\text{K}$ .

**Peak/trough Locations** For immediate reference, Figure 4.4 shows example radial distribution functions at a sample temperature of 363K, namely of the cation-cation (++) for both liquids. As with bonded structure, it is worth considering that radial distribution functions are non-normalized probabilities, and the locations of peaks and troughs are again more significant than their magnitude. That being mentioned, the RDFs of CG systems presented here occasionally produced minor changes in concavity not present in the reference systems, namely the [pyr14][TFSI] (++) distribution at 298K (Figure A.15d), and the [EMIM][BF<sub>4</sub>] (++) distributions at both temperatures (Figure A.16a,d). While these discrepancies are noticeable when observing the plots, major peaks/troughs are still matched, and on the distribution patterns still reflect overall patterns. Notably enough, these discrepancies all occur in cation-cation (++) distributions, indicating that they could have been induced by simplification of pyrrolodinium and imidazolium rings. As discussed by Wang et. al [21], the intrinsic assumption of radially symmetric interactions in CG systems ignores those that are orientation-dependent, and can have a notable effect when sites have been “aggressively” coarse-grained, like the case of such ring-type molecular structures. The possibility that these rings would be significantly better represented with multiple coarse-grained sites is apparent.

**Fits Achieved** At a glance, the fits achieved in development of non-bonded structure for the CG models match an overall pattern. A good sign regarding the scaling of non-

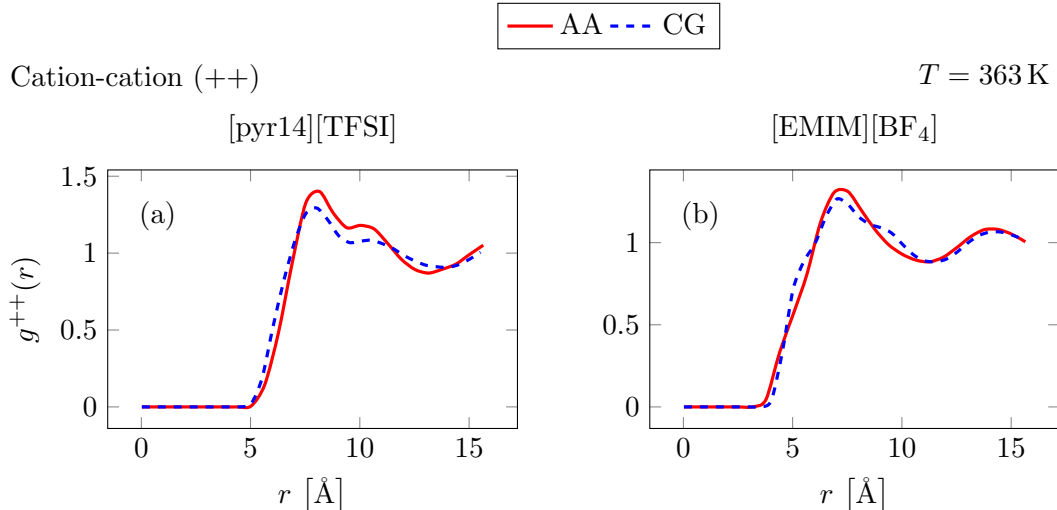


Figure 4.4. Example radial distribution function results, [pyr14][TFSI] (left), and [EMIM][BF<sub>4</sub>] (right)-types, sampled from cation-cation (++) pairs at  $T = 363\text{K}$ .

bonded forces at different temperatures is that locations which are over/underestimated in probability are consistently over/underestimated at the opposing temperature, for example the (+-) and (-) distributions for [pyr14][TFSI] (Figure A.15b,e and A.15c,f) and the (+-) distribution for [EMIM][BF<sub>4</sub>] (Figure A.16b,e). Also, the distributions start/end points match well, indicating that neighbors at extremely close and far distances are well reproduced. The case of [pyr14][TFSI]'s (+-) distributions produced a shift in the 5-10Å range not present in other distributions which is unaccounted for, though. This again could be attributed to simplification of pyrrolodinium and imidazolium rings, as not this problem, nor presence of extra concavity changes are present in any (-) distribution produced. While the bonded structure, produced by manual fitting of harmonic oscillators, provided easy access to fine-tuning to iteratively assess such discrepancies, MSCG with force matching developed force-fields in one iteration, and therefore was applied as-is.

### 4.3 Dynamics

Table 4.1 notes the values of  $\alpha$  and  $\beta$  found for each liquid, while Tables 4.2 and 4.3 compare the all-atom reference diffusion coefficients, those of the conventional CG system, and those of the calibrated PDF-CG system for each ionic liquid. While diffusion coefficients are seen here, their corresponding mean-square displacement plots can be seen in Figures A.20 and A.21 of the Appendix.

**Empirical Coefficients Determined** Immediate examination of Table 4.1 is admittedly confusing. The difference in magnitudes between  $\alpha$  and  $\beta$  coefficients determined for [pyr14][TFSI] and [EMIM][BF<sub>4</sub>] is notable. Also, the coefficient values of zero for [EMIM][BF<sub>4</sub>]'s (++) pairs appears inconsistent. However, the design of the PDF-CG method (as implied in Equation 2.12) implies no existence of unique sets of dampening coefficients. Hence, many drastically different sets of coefficients may still produce correct dynamical behavior. In this work, coefficients were then simply determined by the seemingly easiest and most convenient progression of terms. For [pyr14][TFSI], this was done by modifying all terms of  $\beta$  equally, and for [EMIM][BF<sub>4</sub>], both  $\alpha^{++}$  and  $\beta^{++}$



were assumed as zero, expecting cation-cation dissipation and fluctuation to derive from cation-anion interaction.

**Fits to Mean-Square Displacement** As mentioned in Section 3.4, the diffusion coefficient can be found as proportional to the slope of a mean-square displacement curve in time. Hence, the diffusion coefficients listed in Tables 4.2 and 4.3 are all proportional to the slopes of the curves in Figures A.20 and A.21 of the Appendix. Any possible concern regarding this method for determining diffusion would likely be attributed to the goodness of fit for such slopes. Examination of the Figures, however, shows obvious goodness in linear fits.

**Diffusion Coefficients** The reality of dynamics when using C-CG methods can be seen immediately by the diffusion coefficients of [pyr14][TFSI] in Table 4.2. At the elevated temperature of 363K, C-CG produced diffusion coefficients four to five times higher than the AA reference system did. However, the modification provided by the PDF-CG method remedied these values to nearly five percent error. At room temperature (298K), the results are even more exaggerated. Here, diffusion coefficients were more than ten times higher for C-CG, and implementation of PDF-CG corrected them to about 50 percent error. The same pattern can be seen for [EMIM][BF<sub>4</sub>] in Table 4.3, where diffusion was again four to five times higher using C-CG, then corrected significantly by PDF-CG. It should be noted that the 298K values using PDF-CG were not necessarily less accurate than those at 363K for any methodical reason, but were simply not calibrated as accurately due to time constraints. The systems are a work in progress, and the PDF-CG method provides opportunity to modify dampening coefficients, improving diffusivity, at any time. In any case, diffusion was corrected drastically, and the effects of such can be seen during application of the systems in the proceeding chapter.

Table 4.1. Values of  $\alpha$  and  $\beta$  determined by dynamics calibration.

Ionic liquid	$T$	$\alpha^{++}$	$\beta^{++}$	$\alpha^{+-}$	$\beta^{+-}$	$\alpha^{--}$	$\beta^{--}$
[pyr14][TFSI]	363K	0.230	8.33	0.130	8.33	0.040	8.33
	298K	0.153	5.78	0.039	5.78	0.012	5.78
[EMIM][BF <sub>4</sub> ]	363K	0.00	0.00	3.40	39.6	6.08	44.3
	298K	0.00	0.00	1.30	23.1	6.56	72.8

Table 4.2. Diffusion coefficients of the [pyr14][TFSI] ionic liquid.

$T$	Method	$D^+ \times 10^{10}$ [m <sup>2</sup> /s]	$D^- \times 10^{10}$ [m <sup>2</sup> /s]
363K	AA	1.243	1.061
	C-CG	5.367	4.102
	PDF-CG	1.208	0.994
298K	AA	0.121	0.100
	C-CG	1.626	1.016
	PDF-CG	0.190	0.155

Table 4.3. Diffusion coefficients of the [EMIM][BF<sub>4</sub>] ionic liquid.

$T$	Method	$D^+ \times 10^{10}$ [m <sup>2</sup> /s]	$D^- \times 10^{10}$ [m <sup>2</sup> /s]
363K	AA	2.032	1.951
	C-CG	8.364	7.727
	PDF-CG	2.437	2.217
298K	AA	0.471	0.359
	C-CG	2.458	2.219
	PDF-CG	0.506	0.398

# 5 Application

## 5.1 Vacuum-interface Systems

With structurally and dynamically-accurate CG models successfully created, computational experiments at interface could be performed. Specifically, the interface of a vacuum with the ionic liquids considered here was chosen. To create the interface, periodic boundary conditions in the  $z$ -direction were first removed. The size of the periodic box in that direction was then expanded, namely by three times. This way, the length of the periodic box in the  $z$ -direction was three times as long as the length occupied by the bulk fluid recently calibrated in Section 3.4, exposing the surfaces of the bulk fluid on both ends in the  $z$ -direction to free space. When time steps were then advanced, an interaction with the vacuum-interface surface ensued in the  $z$ -direction. To illustrate the conditions, visualization of the vacuum-interface system after advancing time steps for 20 ns for each ionic liquid are shown in Figures A.7 and A.8 of the Appendix. Besides the move of the interface boundary in the  $z$ -direction, the vacuum-interface systems were identical to the dynamics calibration systems from Section 3.4, and were ran at both  $T_{hi} = 363\text{K}$  and  $T_{lo} = 298\text{K}$ . For the sake of clarity, Table 5.1 shows the modified box sizes and number of pairs present for each of these systems. To collect data, the

Table 5.1. Varied parameters of the vacuum-interface systems.

Ionic liquid	Box size ( $\text{\AA}$ )	Number of ions
[pyr14][TFSI]	$84.8864 \times 84.8864 \times 254.6592$	1152 pairs
[EMIM][BF <sub>4</sub> ]	$81.3076 \times 84.0786 \times 202.2516$	1728 pairs

systems were run for 40ns each at vacuum-interface. In both cases, slight evaporation of ionic liquid components was observed in simulation. In the case of [pyr14][TFSI], only cations evaporated, while anions did so for [EMIM][BF<sub>4</sub>]. Table 5.2 shows the number of ions evaporated for each liquid and temperature combination after an elapsed simulation time of 35ns. The number of evaporated ions is relevant, as it had a noticeable effect on CG site density, which is discussed in the next section.

Table 5.2. The number of ions evaporated out of the interface at 35ns for each liquid and temperature.

Method	$T$	[pyr14][TFSI]	[EMIM][BF <sub>4</sub> ]
		# Cations evaporated	# Anions evaporated
C-CG	363K	106	39
	298K	91	37
PDF-CG	363K	82	18
	298K	90	27

## 5.2 Interfacial Properties

Besides evaporation of ions, vacuum-interface phenomena were not easy to observe visually. Therefore, properties had to be calculated in order to note the behavior of the generated systems at interface. The property chosen to do so in this work was the *density profile*, generated by each CG site type. The reasons for this being: (1) Fluctuations in density could be observed in the  $z$ -direction, (2) Focus could be given to particular, possibly dominant/non-dominant sites on any ion, and (3) Ion orientation in the  $z$ -direction could be observed based on density peaks. These density profiles were calculated by dividing the system's box into sections of depth  $l$ , counting the number of CG sites of any particular type within that section, and taking the ensemble average of the number of sites counted. By implementing a small enough value of  $l$  and averaging over enough system snapshots, smooth density profiles were generated. A density profile value near zero indicates presence of the vacuum, bulk fluid is then in the middle, and variations from the bulk fluid density indicates interface-induced behavior. The value found to be small enough for creation of smooth and meaningful plots was  $l = 0.170\text{\AA}$ , and 10ns worth of samples were taken after 30ns of simulation time had elapsed. Figures A.22-A.31 of the Appendix incorporate density profiles generated in this manner, and progressive commentary follows from here on.

**Control Comparison** Figures 5.1-5.2 in-text, and also Figures A.22-A.23 of the Appendix depict density profiles for both liquids with all available CG site types present at 298K, with profiles generated not only in the direction of the vacuum-interface ( $z$ ), but also in a direction with the conventional bulk boundary conditions for control samples ( $x$ ). A temperature of 298K for these plots was chosen due to its more prominent structuring at the interface, as will be discussed promptly. Visual comparisons of the interface fluctuations in  $z$  compared to those in  $x$  show a significant layering structure. For [pyr14][TFSI], at least one layer is present (Figure 5.1a), while [EMIM][BF<sub>4</sub>] indicates more than one layer penetrating into the surface (Figure 5.2a). When compared side-by-side, the fluctuations at the bulk fluid in the  $z$  direction are similar to those found in the  $x$ , indicating that the vacuum in  $z$  effects the near-immediate interface, then the fluid returns to bulk behavior as depth is increased. Also, inspection of the two Figures reveals significantly lower density profile magnitudes for the [pyr14][TFSI] cation components and [EMIM][BF<sub>4</sub>] anion components. This can be attributed to the evaporation noted in Table 5.2.

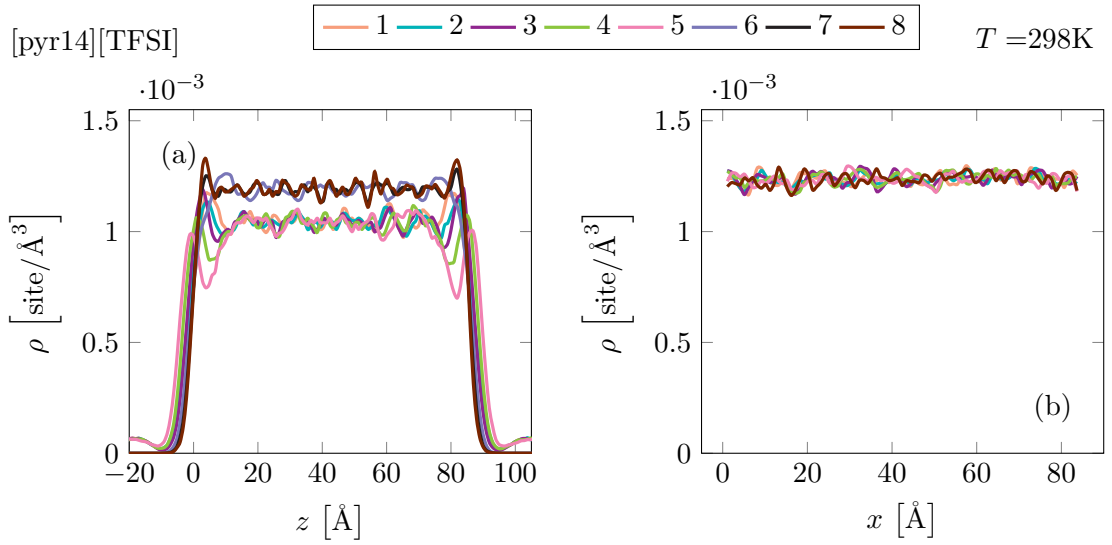


Figure 5.1. By-type number density profiles of the [pyr14][TFSI] ionic liquid at 298K, using the PDF-CG method: (left)-(right) in the  $z$  and  $x$ -directions respectively.

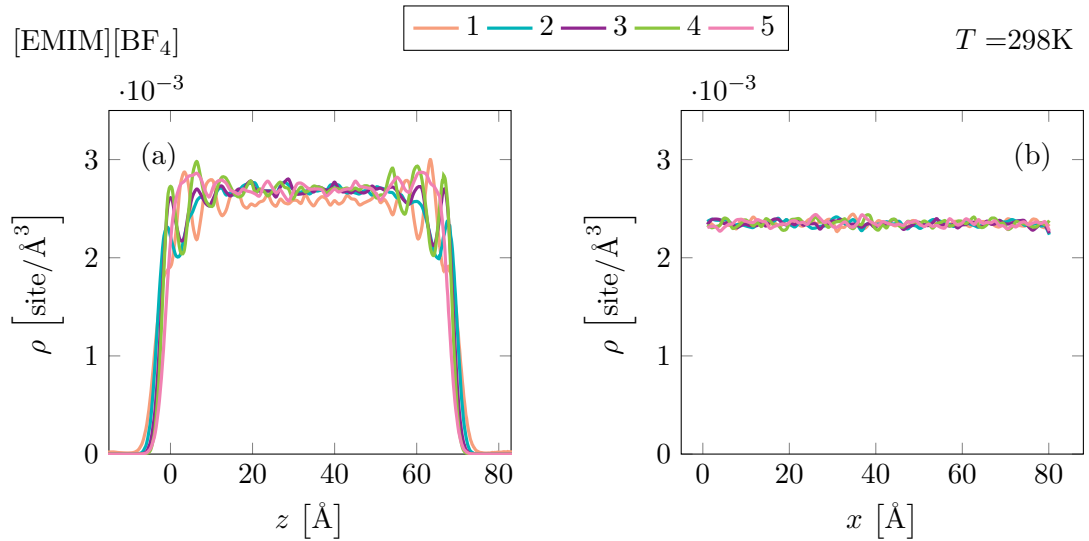


Figure 5.2. By-type number density profiles of the EMIM ionic liquid at 298K, using the PDF-CG method: (left)-(right) in the  $z$  and  $x$ -directions respectively.

**Effect of Temperature** As might be expected, the two constrained temperatures at which this system was run produced significantly different behavior at interface. This is illustrated by samples in Figures 5.3-5.4 of the text, and in-full within Figures A.24-A.25 of the Appendix. At interface, the lower temperature produced more prominent structure for both liquids. This can be explained by the opposing effects of structure and dynamics. At the higher temperature, the system is more dominated by its kinetic energy, and hence has less opportunity to produce structured layering at the interface, but when the temperature is decreased, ionic interaction becomes dominant, affording enhanced near-interface layering. In both cases of the liquids presented here, results show the significance of considering vacuum-interface effects at room temperature.

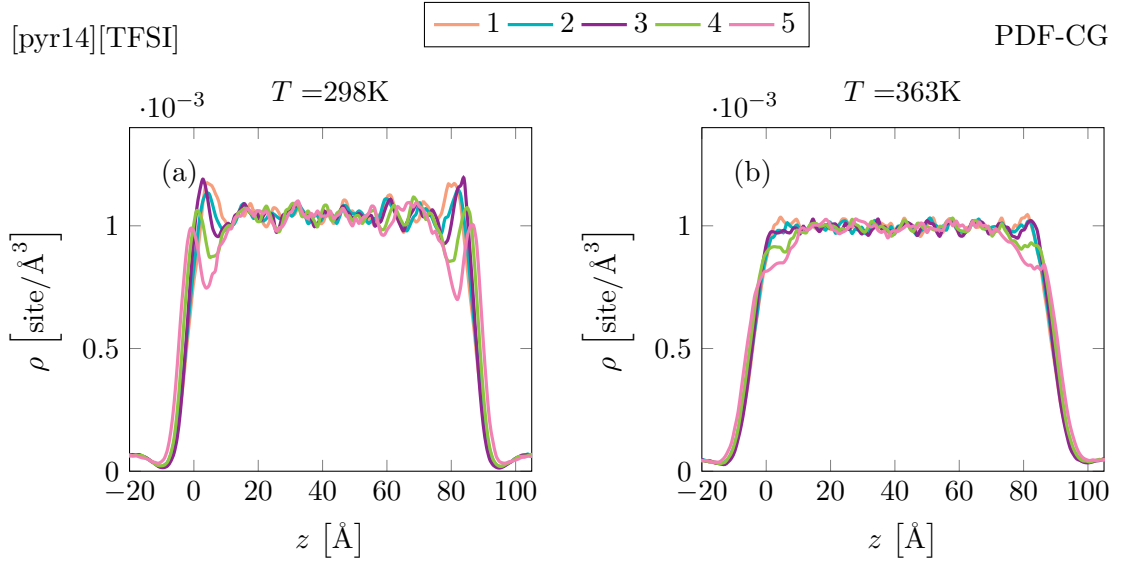


Figure 5.3. The effect of temperature on  $z$ -direction  $[\text{pyr14}]^+$  cation density profiles: (left)-(right) at 363K and 298K, respectively.

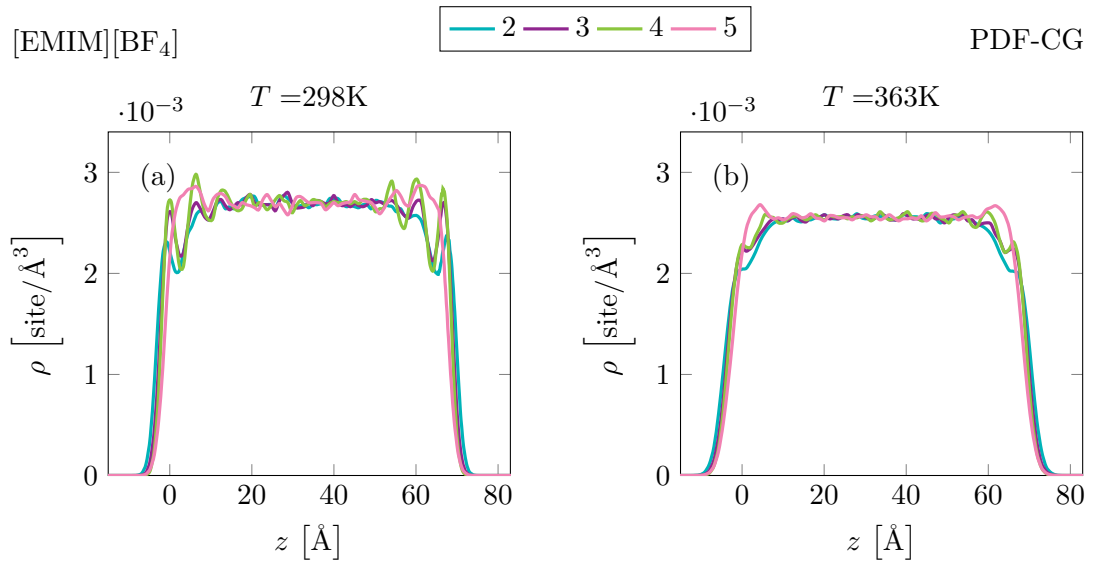


Figure 5.4. The effect of temperature on  $z$ -direction  $[\text{EMIM}]^+$  cation density profiles: (left)-(right) at 363K and 298K, respectively.

**Cation Orientations** By more closely examining the density peaks generated at the interface, it is possible to see how sites statistically orient themselves in the  $z$ -direction. Figures 5.5 and 5.6 depict the profiles for each liquid, zoomed in near the interface at the positive end. In the case of [pyr14][TFSI], the peaks travel from site 1 to 2,3,4 and 5 consecutively as  $z$  is increased. Based on this, it can be inferred that the cation often orients itself with its alkyl chain perpendicular to the interface, as depicted visually on the left-hand side. This is further implicated by measurements shown in the Figure. The distances between furthest peaks of the profile is  $6.11 \text{ \AA}$ , while the total length of the cation from bonded distributions is  $6.22 \text{ \AA}$ . These measurements being almost exactly the same, the cation is then often orienting itself at a near-perfect 90-degree angle. A similar principle can be examined for the [EMIM][BF<sub>4</sub>] cation. In its case, three out of four profile peaks are in the same  $z$  vicinity. Hence, it is often orienting itself parallel to the interface. This result is similar to that found by Sloutskin et. al [11], where the similar [BMIM][PF<sub>6</sub>] ionic liquid was experimentally exposed to a vacuum in the lab, and measured using X-ray reflectivity. The cation here was similar, and their work deduced that it was likely oriented in the same fashion.

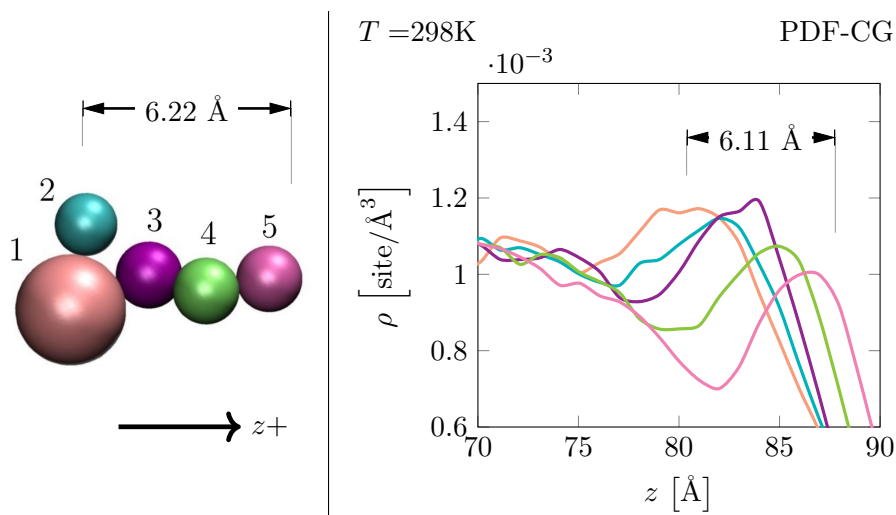


Figure 5.5. Orientation of [pyr14]<sup>+</sup> cation from density plots: predicted  $z$  orientation (left) and supporting density profile (right).

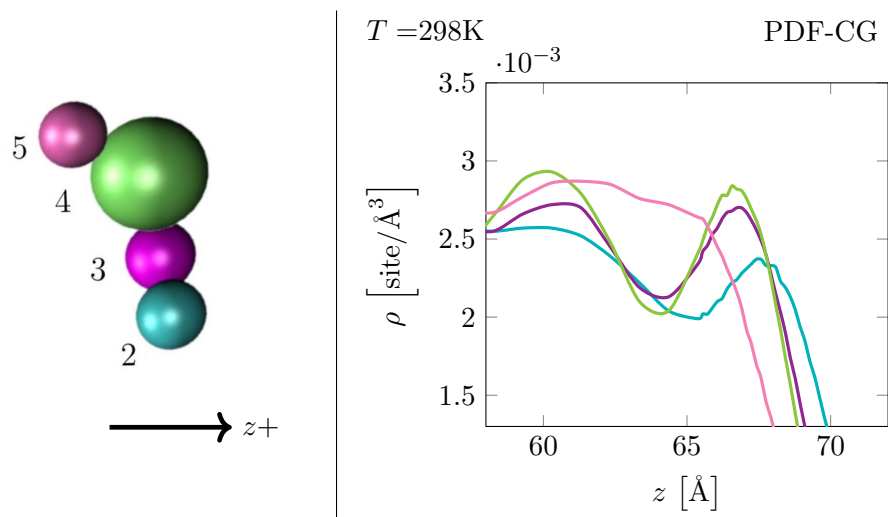


Figure 5.6. Orientation of  $[\text{EMIM}]^+$  cation from density plots: predicted  $z$  orientation (left) and supporting density profile (right)



**Effect of Coarse-graining Method** Similarly to how temperature affected interfacial ordering of the liquids studied here, the coarse-graining method employed also had an effect. In the Appendix, Figures A.26 and A.27 of the Appendix depict this for [pyr14][TFSI], while Figures A.28 and A.29 do so for [EMIM][BF<sub>4</sub>]. Samples of these plots can be seen in the text in Figures 5.7-5.8. For both liquids, little significant structure is again present at 363K regardless of method. At 298K, though, a difference in results between C-CG and PDF-CG methods is clearly seen. A similar explanation is offered: the PDF-CG method inhibits fast dynamics which otherwise would dominate the kinetic versus ionic interaction opposition, allowing the accurate structural behavior to be observed.

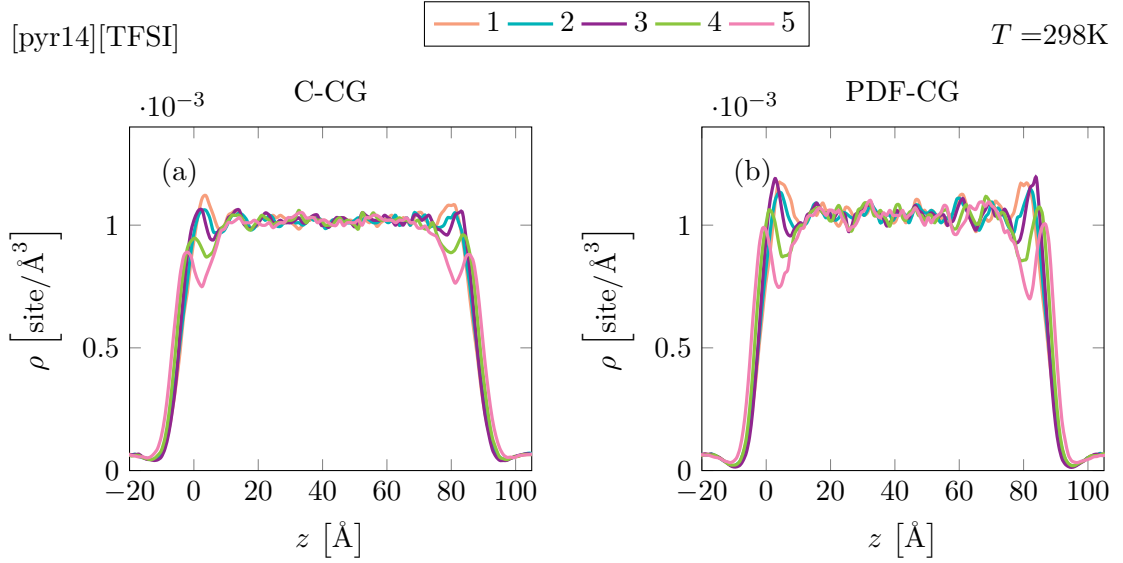


Figure 5.7. The effect of CG method on  $z$ -direction [pyr14]<sup>+</sup> cation density profiles at 298K: (left)-(right) using C-CG and PDF-CG methods, respectively.

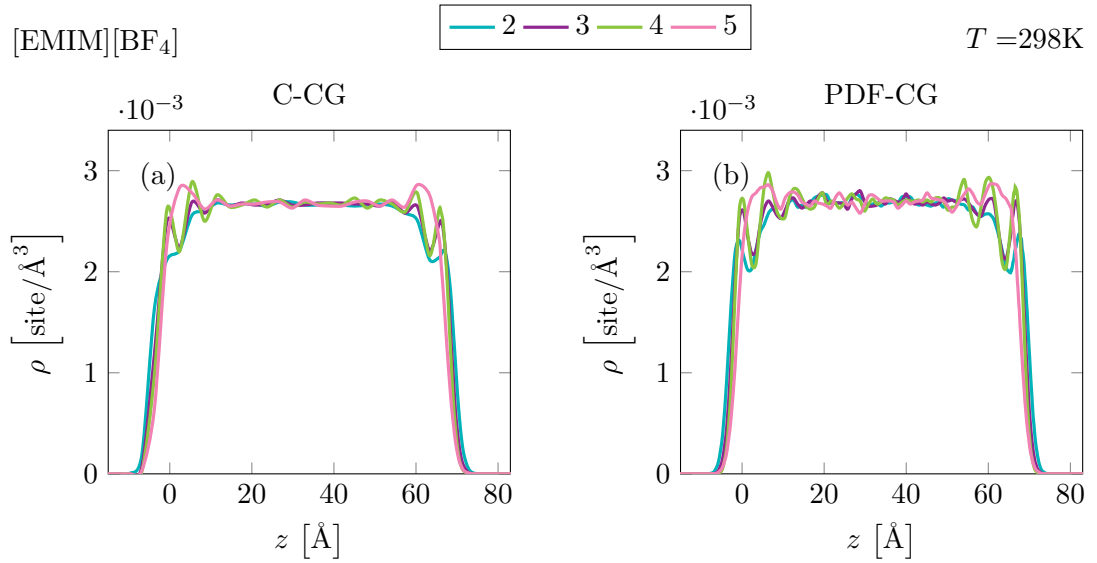


Figure 5.8. The effect of CG method on  $z$ -direction [EMIM]<sup>+</sup> cation density profiles at 298K: (left)-(right) using C-CG and PDF-CG methods, respectively.

**Multilayer Ordering** Finally, Figures A.30 and A.31 of the Appendix show the main sites, representing the dominant behavior of cation and anion, for each liquid plotted together. These are sampled in Figure 5.9 of the text. For both liquids, the site containing the pyrrolidinium or imidazolium ring was chosen as a main representative, along with the [pyr14][TFSI] anion’s central site, and the [EMIM][BF<sub>4</sub>] anion’s only available site. Examination of these two figures clearly reveals how layers penetrated below the vacuum-interface surface. As was previously noted, the most obvious effects are present while using the PDF-CG method at lower temperatures. This case for the [EMIM][BF<sub>4</sub>] liquid revealed significant multilayer ordering that penetrated two, if not three layers deep, oscillating between cation and anion. In this case, the effects are present for approximately 50 percent of the fluid present. Surprisingly, however, this effect was not nearly as prominent for the [pyr14][TFSI] liquid. Both experimental and computational studies have suggested that longer alkyl chains in ionic liquids leads to more prominent and multilayer ordering [52, 53]. This [pyr14][TFSI] cation, having an alkyl chain with one more alkyl component compared to [EMIM][BF<sub>4</sub>], didn’t hold fast to such an observation. These cations though, having different chemical structures, may not provide a viable comparison.

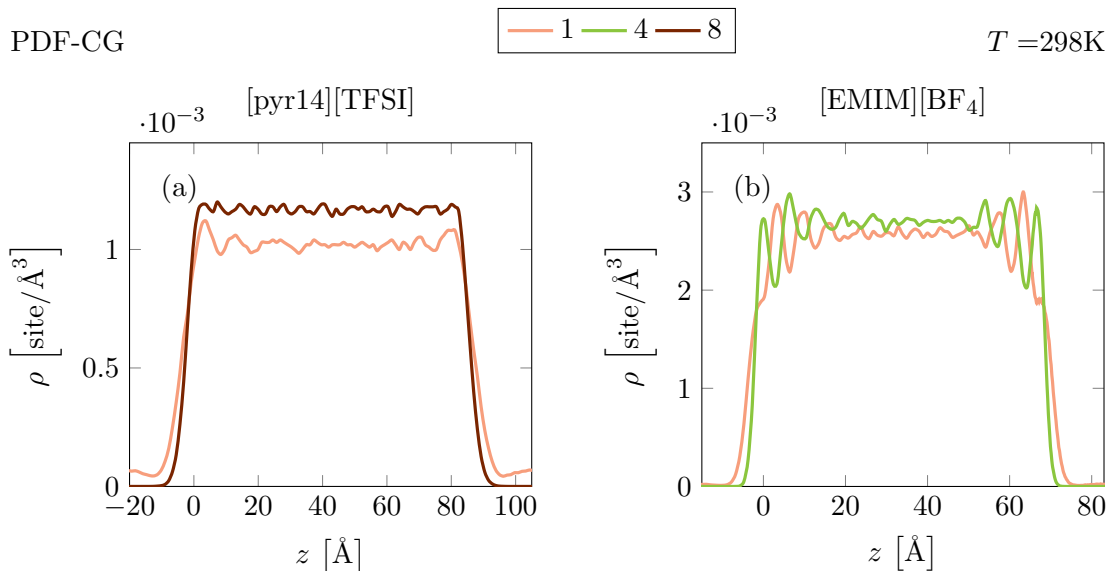


Figure 5.9. Density profiles in  $z$ -direction of the main sites of [pyr14][TFSI] (left) and [EMIM][BF<sub>4</sub>] (right) at 298K using PDF-CG.

## 6 Conclusions

Ionic liquids possess improved properties in many areas of technical application, making them attractive as components in development of next-generation technology. If used as electrolytes, they could aid in developing ultra-high energy batteries. Pertaining to this work, the conjunction of imidazolium or sulfonium-based cations and complex halide anions with Lithium-air electrode materials has potential to produce batteries with significantly higher energy density than concurrent technologies. Such advancements could help pave the way for electrically-powered mobile technology, like the interest-gathering sector of hybrid-electric aircraft for space travel. If ionic liquids were thus applied, however, any selected ionic configuration would likely need extensive analysis at any exposed interfaces, some aspects of which are difficult to complete in the lab. This work has endeavored to develop coarse-grained molecular dynamics (CG-MD) systems of two ionic configurations, one of which specifically having the properties critical for implementation in Lithium batteries. Because of its relative simplicity, yet pertinence in modern technology development as described, the vacuum-interface is an excellent place to begin application of MD models. The overarching goals of this work were then twofold: (1) Develop and validate CG-MD systems of the chosen ionic liquid pairs, and (2) expose the developed systems to vacuum-interface for analysis.

Both chosen liquid pairs, abbreviated [pyr14][TFSI] and [EMIM][BF<sub>4</sub>], were proven to match well in bonded and non-bonded structure when compared to all-atom (AA) MD reference systems. Bonded distributions and radial distribution functions often showed near-exact matches, while others portrayed satisfactory resemblance of expectation for CG models. For further improvement, the probability distribution function coarse-graining (PDF-CG) method was implemented to correct the inaccurate dynamics usually present in coarse-grained models. By this method, diffusion coefficients which were 4 to 16 times higher when using conventional coarse-graining (C-CG) matched with low errors. At this work's most developed case of 363K, error was near to five percent. The constraints of time simply limited the case of 298K to decreasing error as much, with no other limitations known.

Previously developed systems were then exposed to vacuum in the  $z$ -direction, allowing analysis along that axis. Density profiles were calculated by CG site type, allowing analysis of density fluctuations, and also prediction of interface ion orientations. The systems were found to vary significantly from bulk behavior in all cases, while notable effects were found due to varying temperatures and the CG method used (either C-CG or PDF-CG). Interface layering was exaggerated at lower temperatures, illustrating the role of contributions between kinetic energy and ionic interaction, and demonstrating the enhanced significance of vacuum-interface effects for these liquids at room temperature. This temperature, then, was more closely examined. Close examination and measurement of by-site density profile peaks showed likelihood that the [pyr14][TFSI] cation was oriented with its alkyl chain perpendicular to the interface, and the cation of [EMIM][BF<sub>4</sub>] was likely oriented parallel to the interface. As with temperature, significant effects of CG method were found. The PDF-CG method revealed the presence of more prominent layering than C-CG could produce, again likely induced by kinetic energy/ionic interaction contributions. Hence, the importance of correcting dynamics is exemplified and proved possible using PDF-CG. Finally, while [pyr14][TFSI] only showed effects to the monolayer at interface, [EMIM][BF<sub>4</sub>] portrayed multilayer order-

ing at 298K, especially while using the PDF-CG method. Oscillations between high cation/anion densities in opposite phases are observed, penetrating at least two layers deep.

Further work may include enhanced coarse-graining of the described pairs, exposure to other interfaces of interest, further examination of anion behavior, simulation with variation of anions, and improvement in determination of PDF-CG method dampening coefficients. Further investigation by the contributors to this work continues. The conclusions found here are hoped and anticipated to aid during development of technologies applying the two ionic pairs considered, and also further development of CG models for ionic liquids.

# A Appendix

## A.1 Coarse-graining Information

Table A.1. Elemental components and properties for the coarse-grained sites of the [pyr14][TFSI] ionic liquid.

Site	Components	Mass (amu)	Charge (e)
1	N,CH <sub>2</sub> ,CH <sub>2</sub> ,CH <sub>3</sub> ,CH <sub>2</sub>	70.115	-1.000
2	CH <sub>3</sub>	15.035	0.0761
3	CH <sub>2</sub>	14.027	0.2344
4	CH <sub>2</sub> ,CH <sub>2</sub>	28.054	0.4695
5	CH <sub>3</sub>	15.035	0.2200
6	CF <sub>3</sub>	69.005	0.0000
7	SO <sub>2</sub>	64.063	0.0000
8	N	20.947	0.0000

Table A.2. Elemental components and properties for the coarse-grained sites of the [EMIM][BF<sub>4</sub>] ionic liquid.

Site	Components	Mass (amu)	Charge (e)
1	BF <sub>4</sub>	86.802	-1.000
2	CH <sub>3</sub>	15.035	0.0761
3	CH <sub>2</sub>	14.027	0.2344
4	N,CH,N,CH,CH	67.071	0.4695
5	CH <sub>3</sub>	15.035	0.2200

## A.2 Representations of Systems

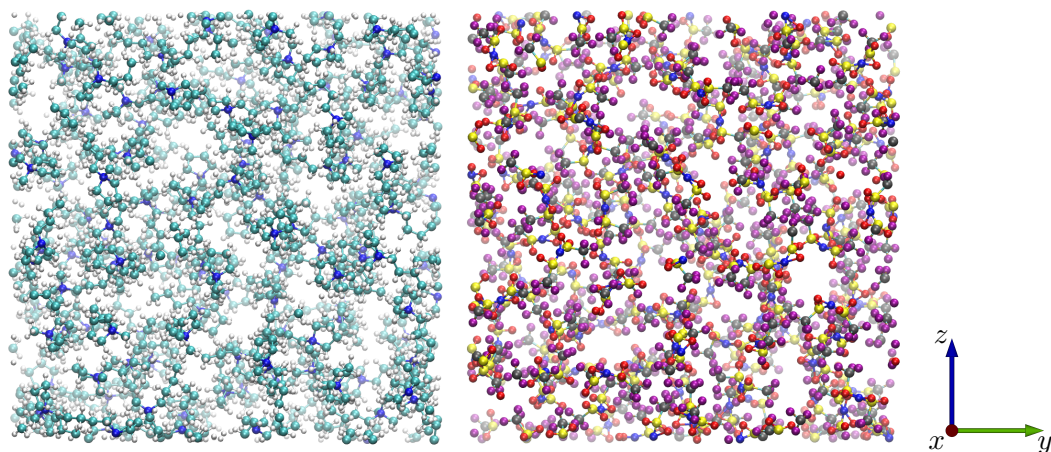


Figure A.1. All-atom reference system visualization for the [pyr14][TFSI] ionic liquid, components: cation (left) and anion (right).

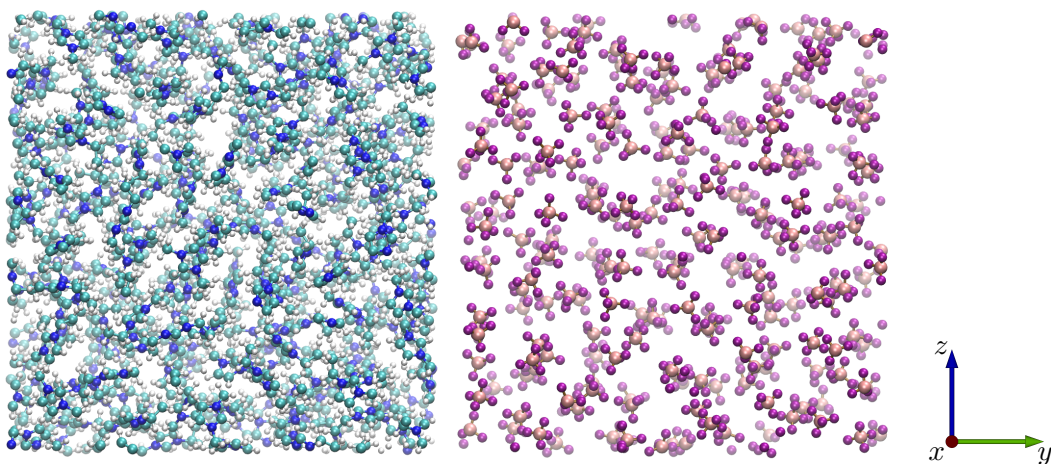


Figure A.2. All-atom reference system visualization for the [EMIM][BF<sub>4</sub>] ionic liquid, components: cation (left) and anion (right).

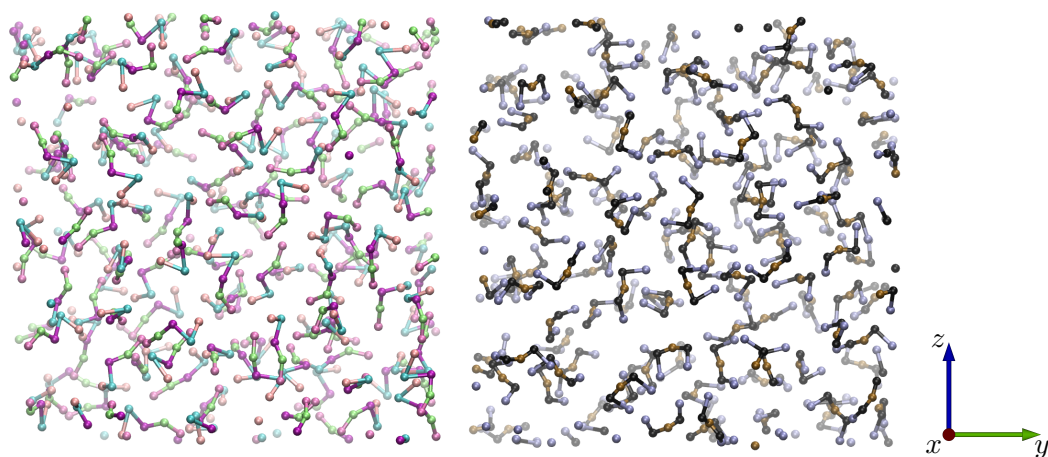


Figure A.3. Structure calibration system visualization for the [pyr14][TFSI] ionic liquid, components: cation (left) and anion (right).

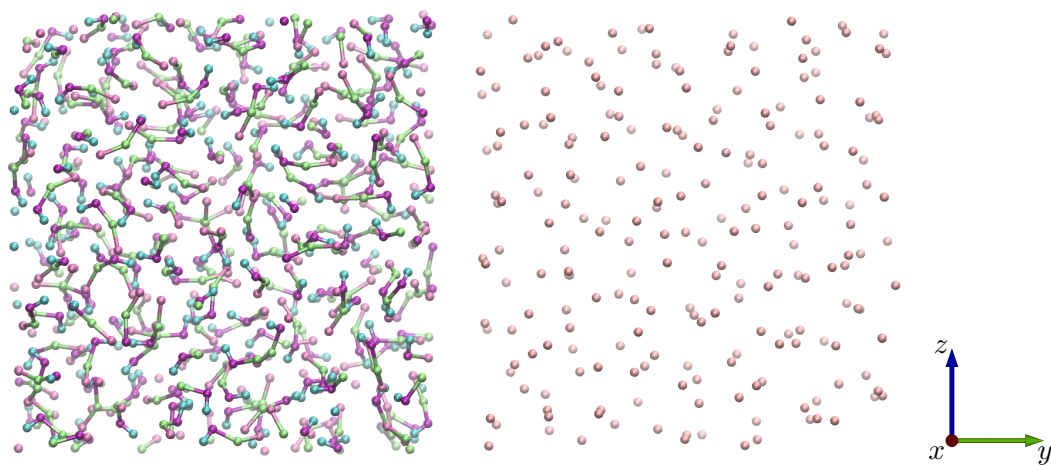


Figure A.4. Structure calibration system visualization for the [EMIM][BF<sub>4</sub>] ionic liquid, components: cation (left) and anion (right).

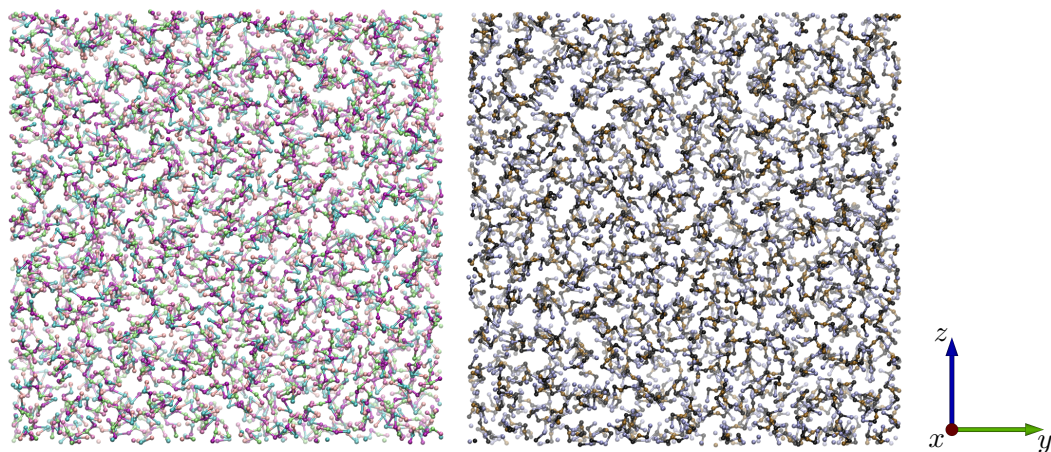


Figure A.5. Dynamics calibration system visualization for the [pyr14][TFSI] ionic liquid, components: cation (left) and anion (right).

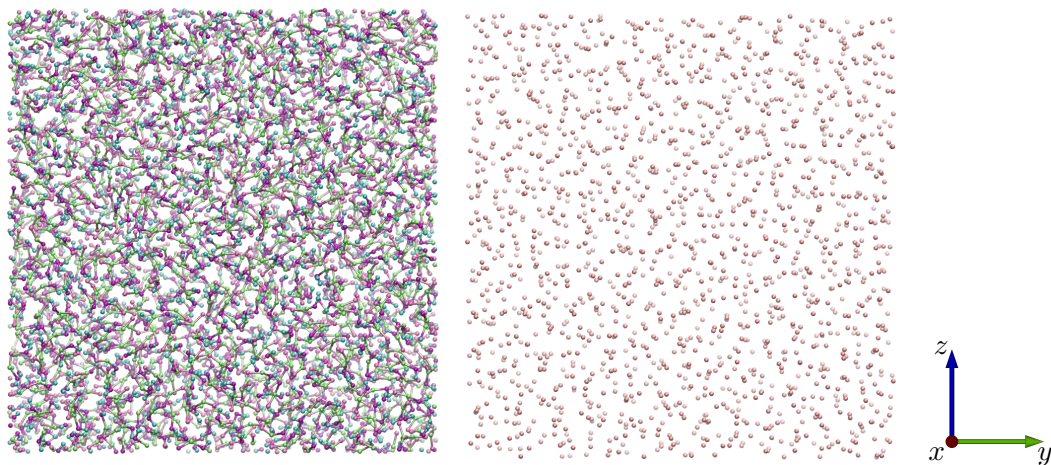


Figure A.6. Dynamics calibration system visualization for the [EMIM][BF<sub>4</sub>] ionic liquid, components: cation (left) and anion (right).



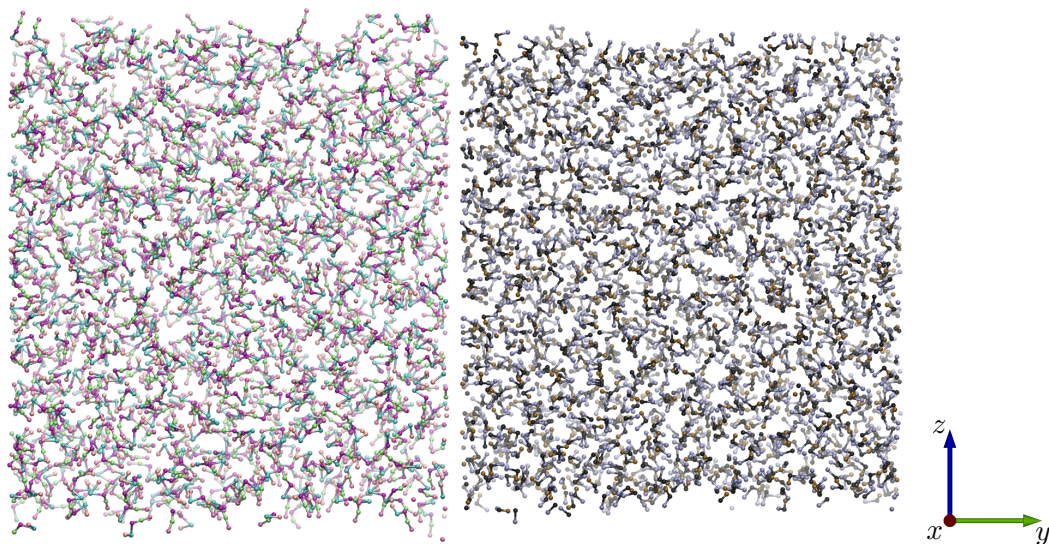


Figure A.7. Vacuum-interface system visualization for the [pyr14][TFSI] ionic liquid, components: cation (left) and anion (right).

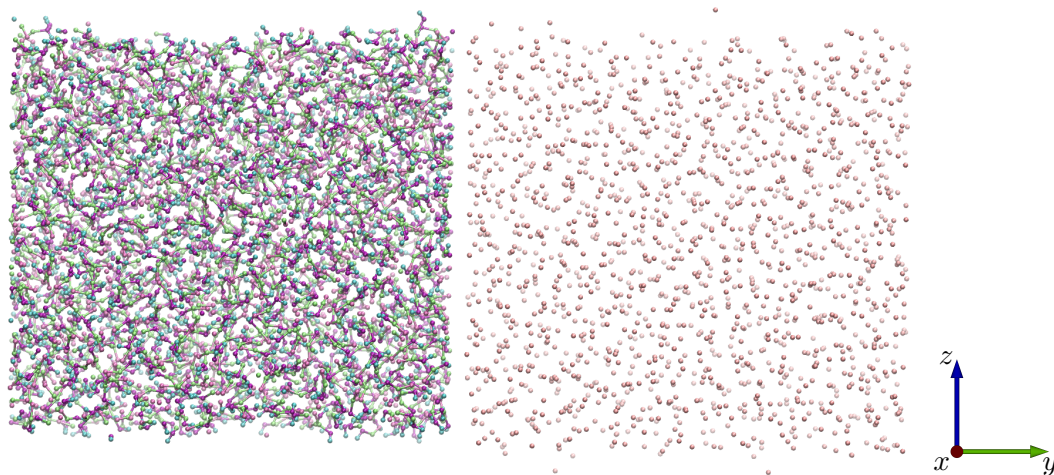


Figure A.8. Vacuum-interface system visualization for the [EMIM][BF<sub>4</sub>] ionic liquid, components: cation (left) and anion (right).

### A.3 Bonded Distributions

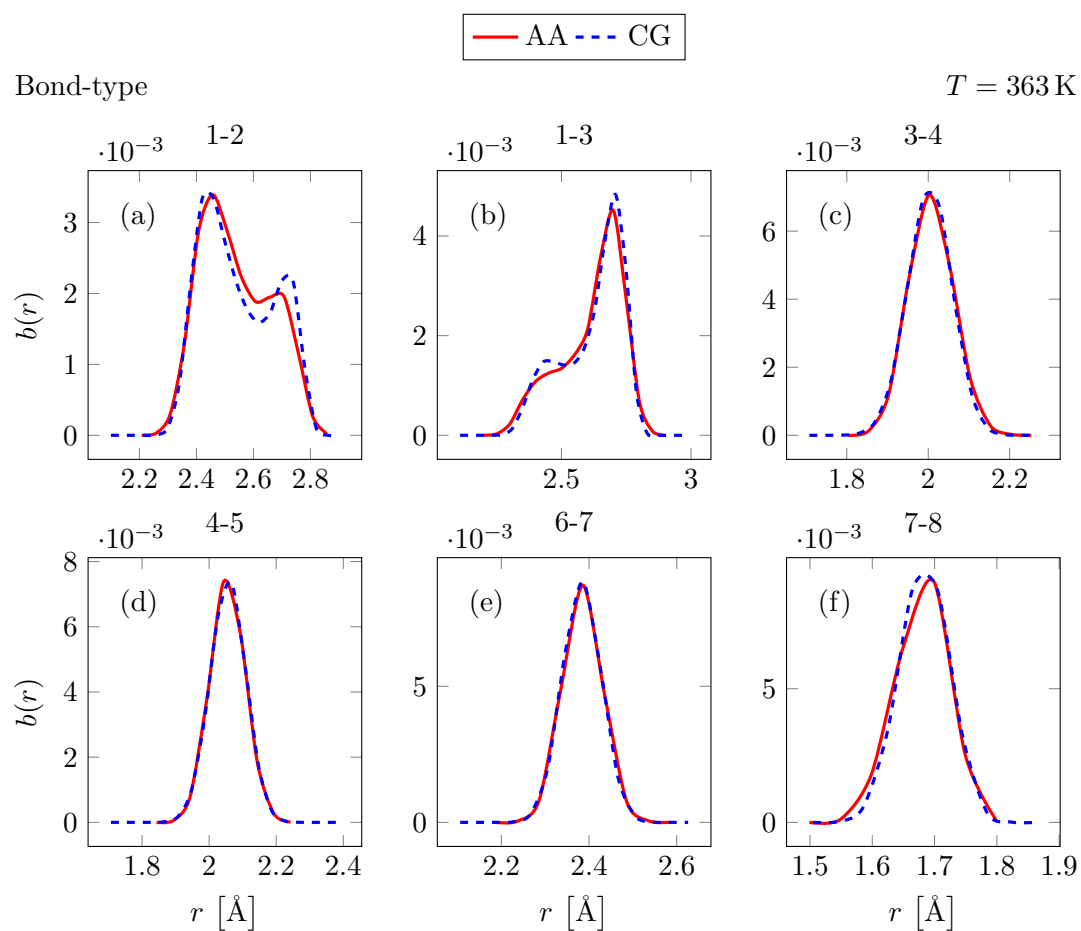
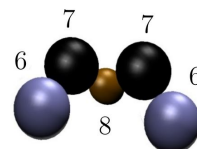
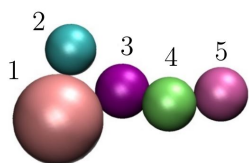


Figure A.9. “Bond”-type bonded distributions of the [pyr14][TFSI] ionic liquid at 363K.



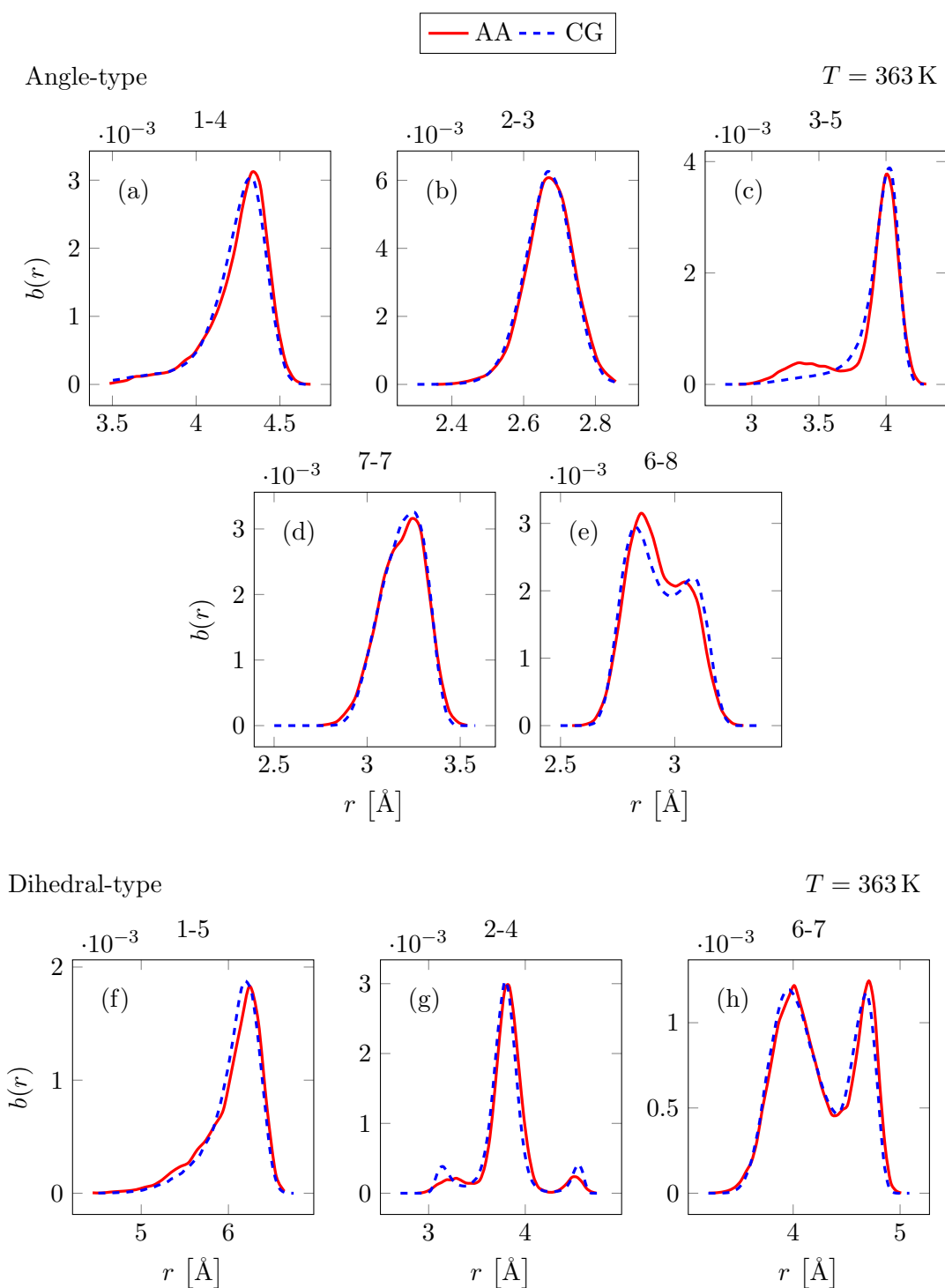
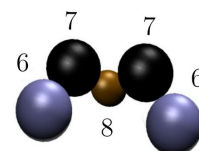
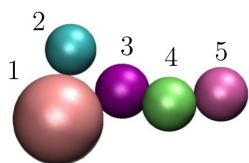


Figure A.10. “Angle” and “dihedral”-type bonded distributions of the [pyr14][TFSI] ionic liquid at 363K.



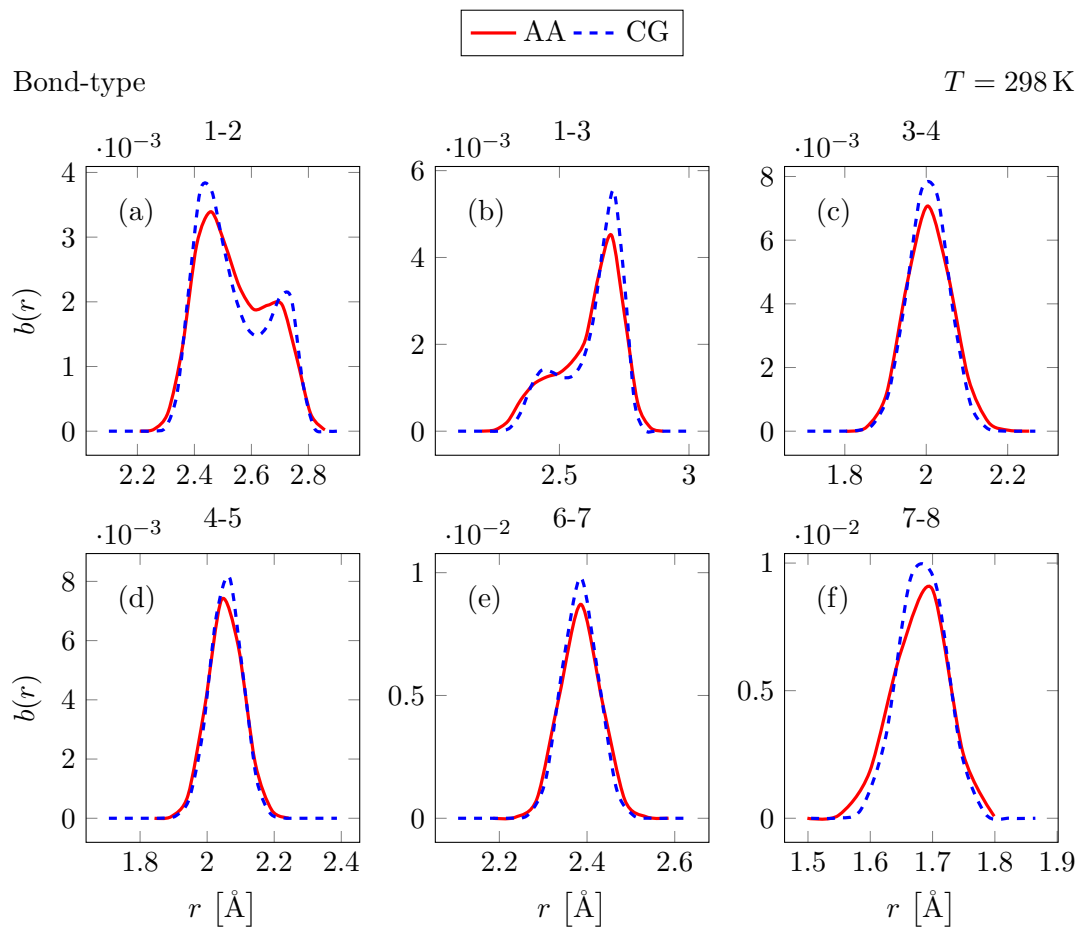
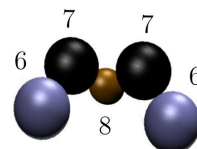
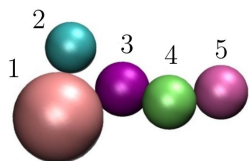


Figure A.11. “Bond”-type bonded distributions of the [pyr14][TFSI] ionic liquid at 298K.



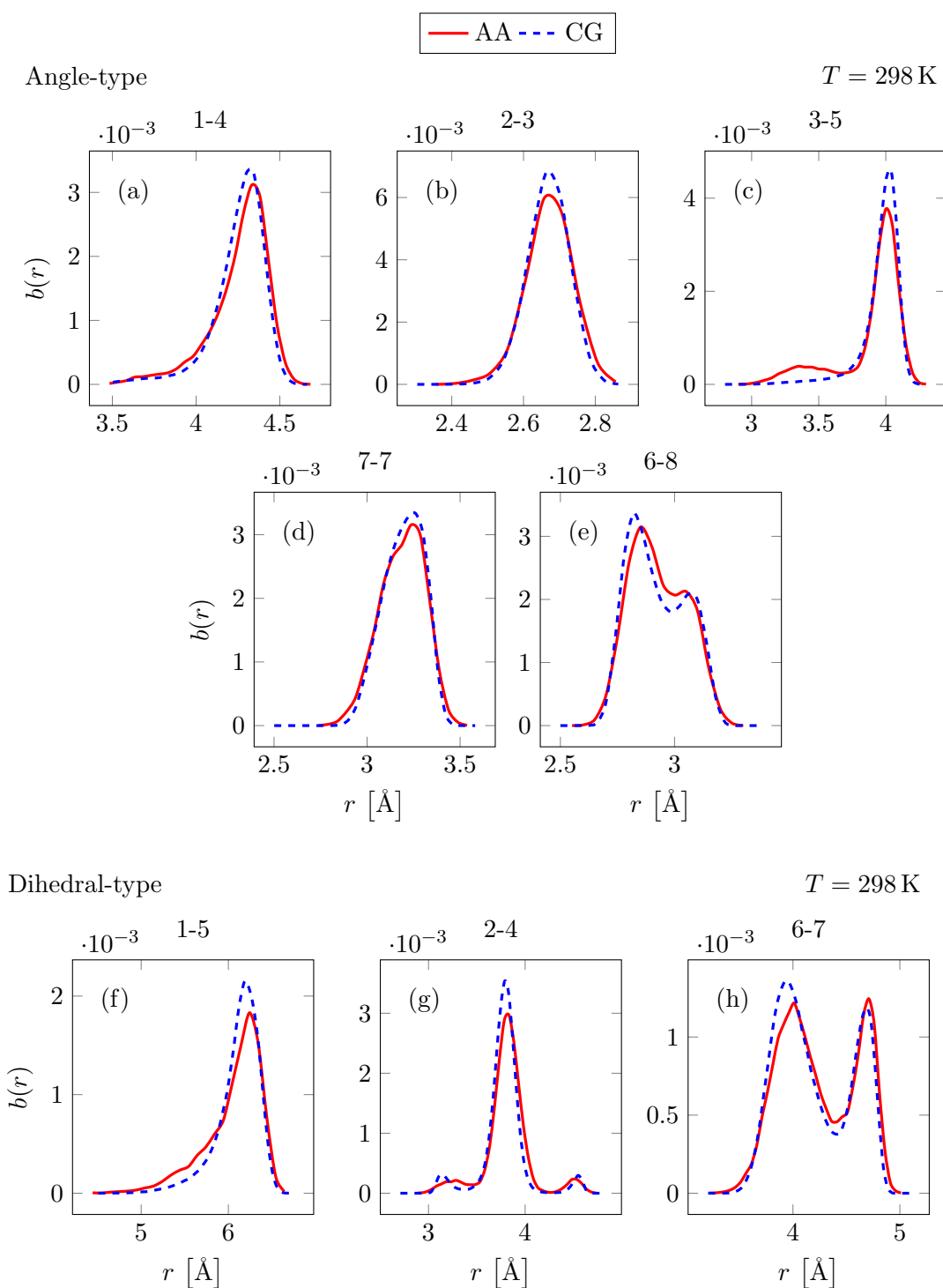
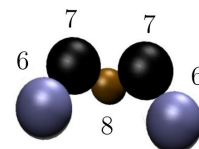
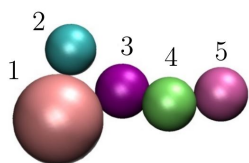


Figure A.12. “Angle” and “dihedral”-type bonded distributions of the [pyr14][TFSI] ionic liquid at 298K.



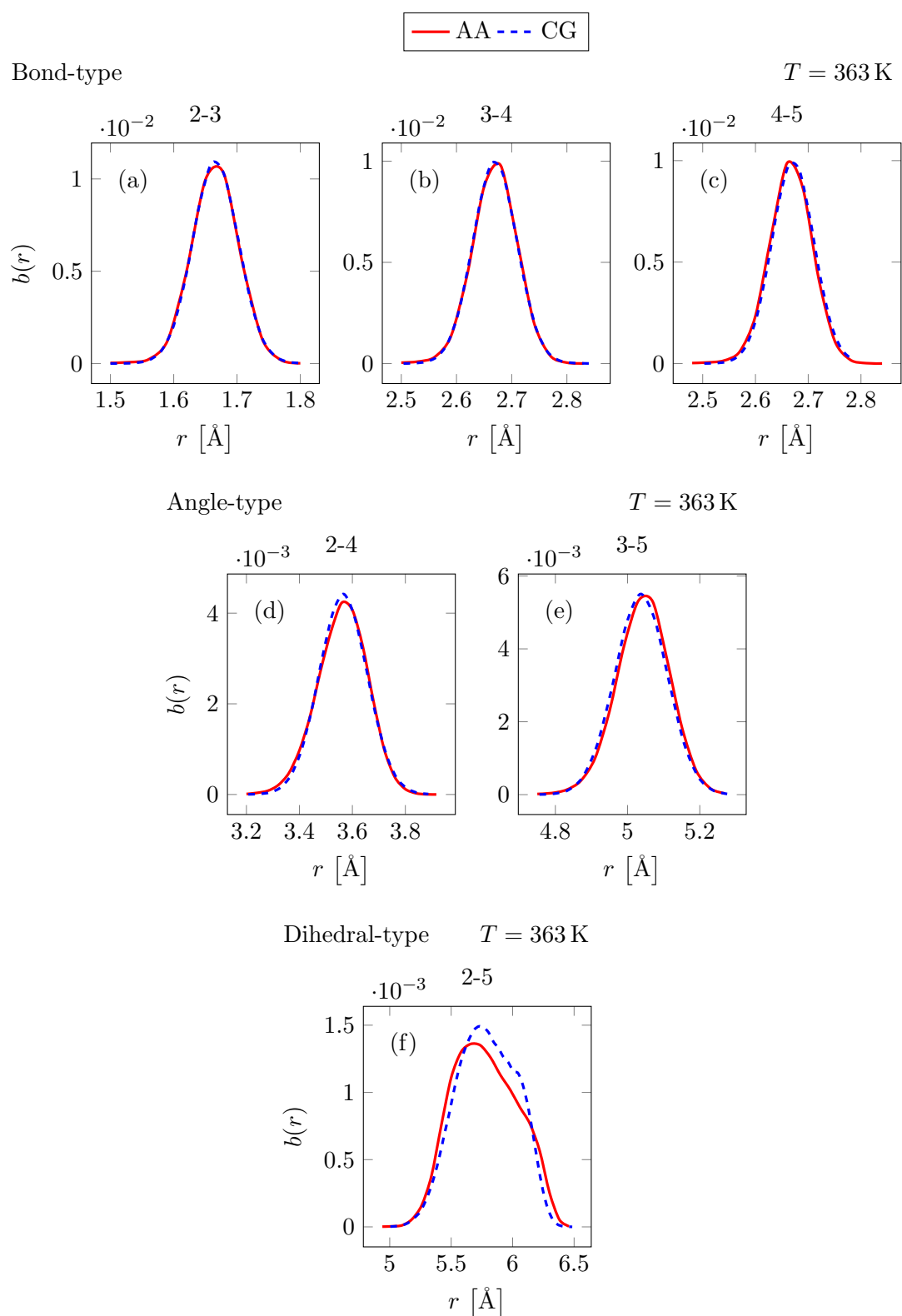
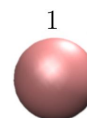
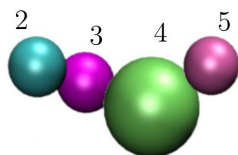


Figure A.13. Bonded distributions of the [EMIM][BF<sub>4</sub>] ionic liquid at 363K.



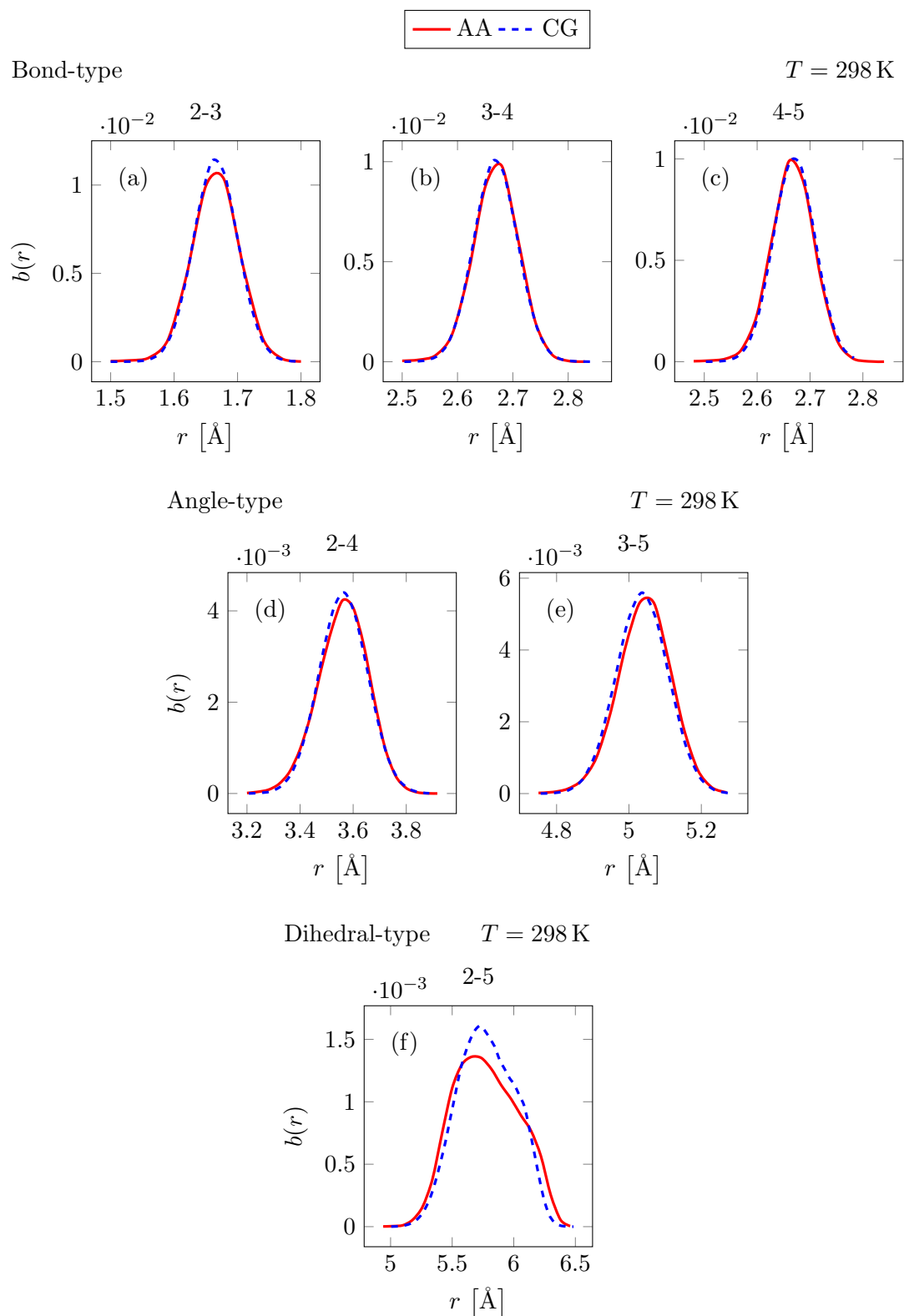
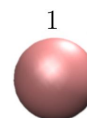
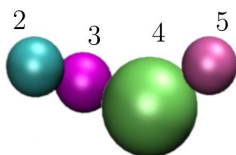


Figure A.14. Bonded distributions of the [EMIM][BF<sub>4</sub>] ionic liquid at 298K.



## A.4 Radial Distribution Functions

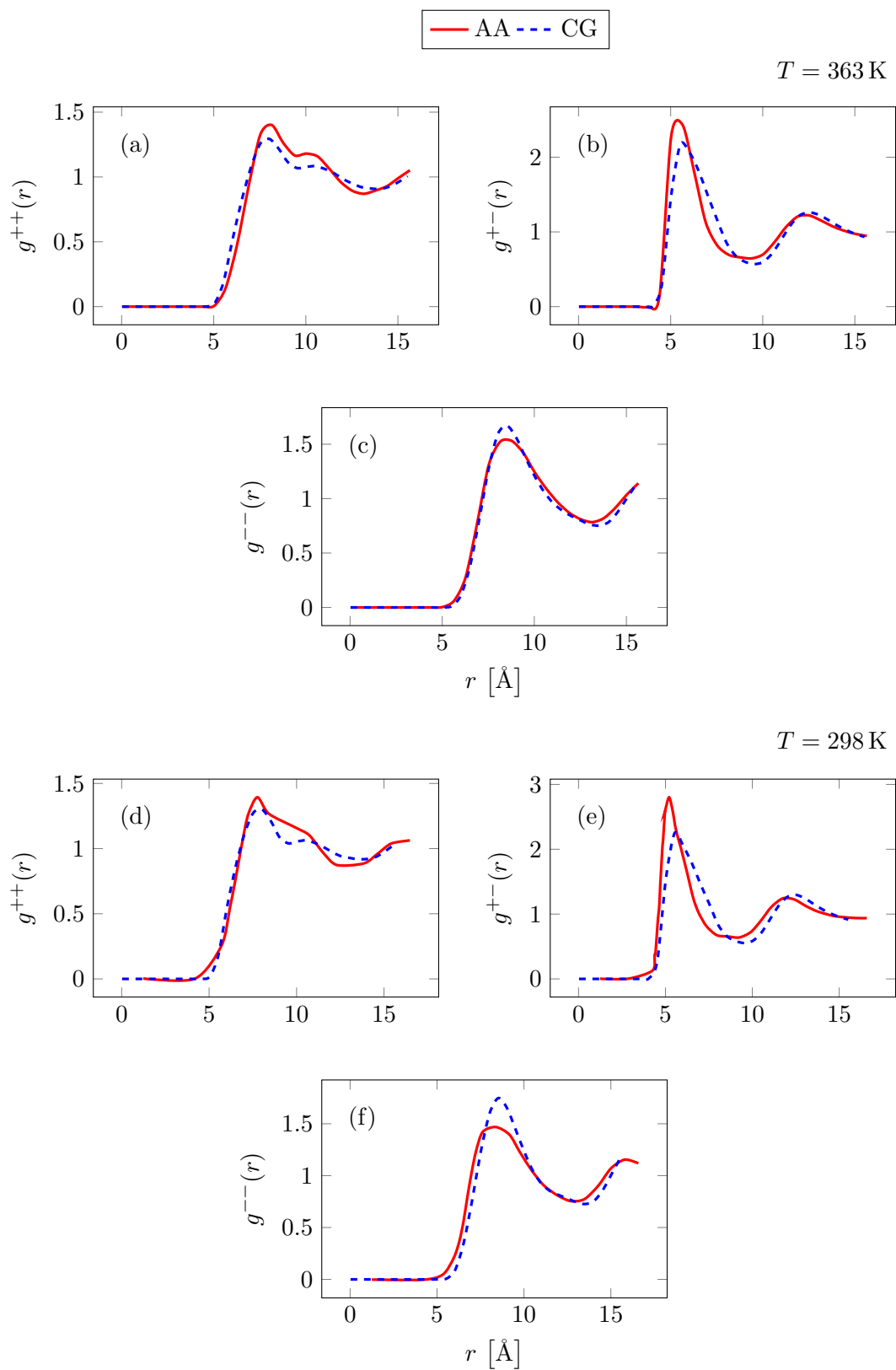
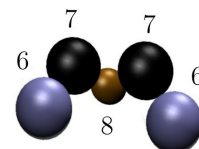
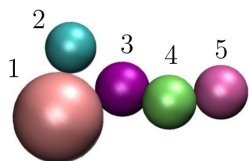


Figure A.15. Radial distribution functions of the [pyr14][TFSI] ionic liquid.





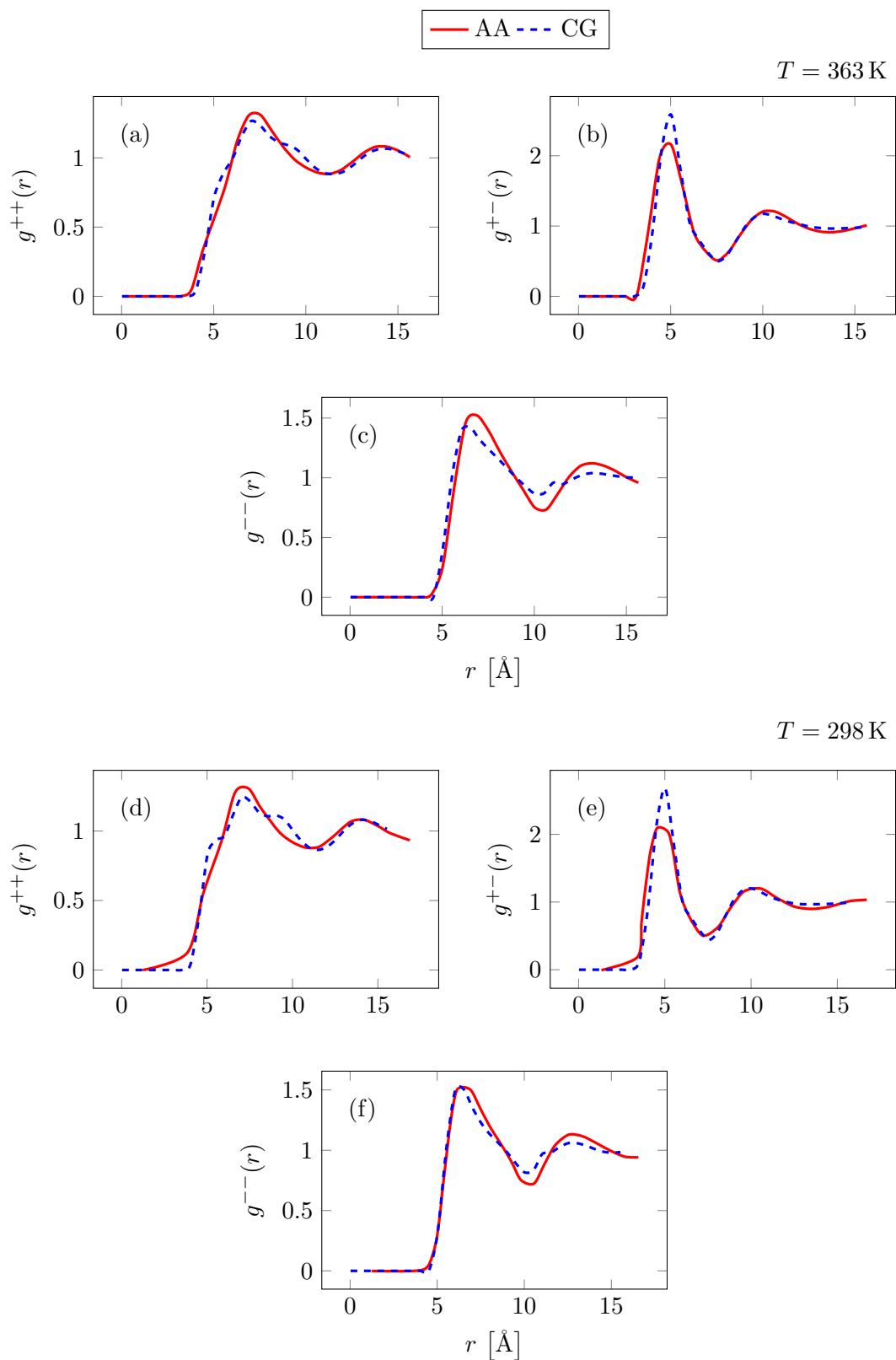
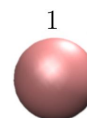
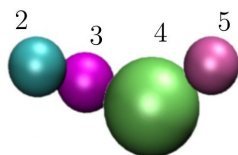


Figure A.16. Radial distribution functions of the [EMIM][BF<sub>4</sub>] ionic liquid.



## A.5 Non-bonded Forces

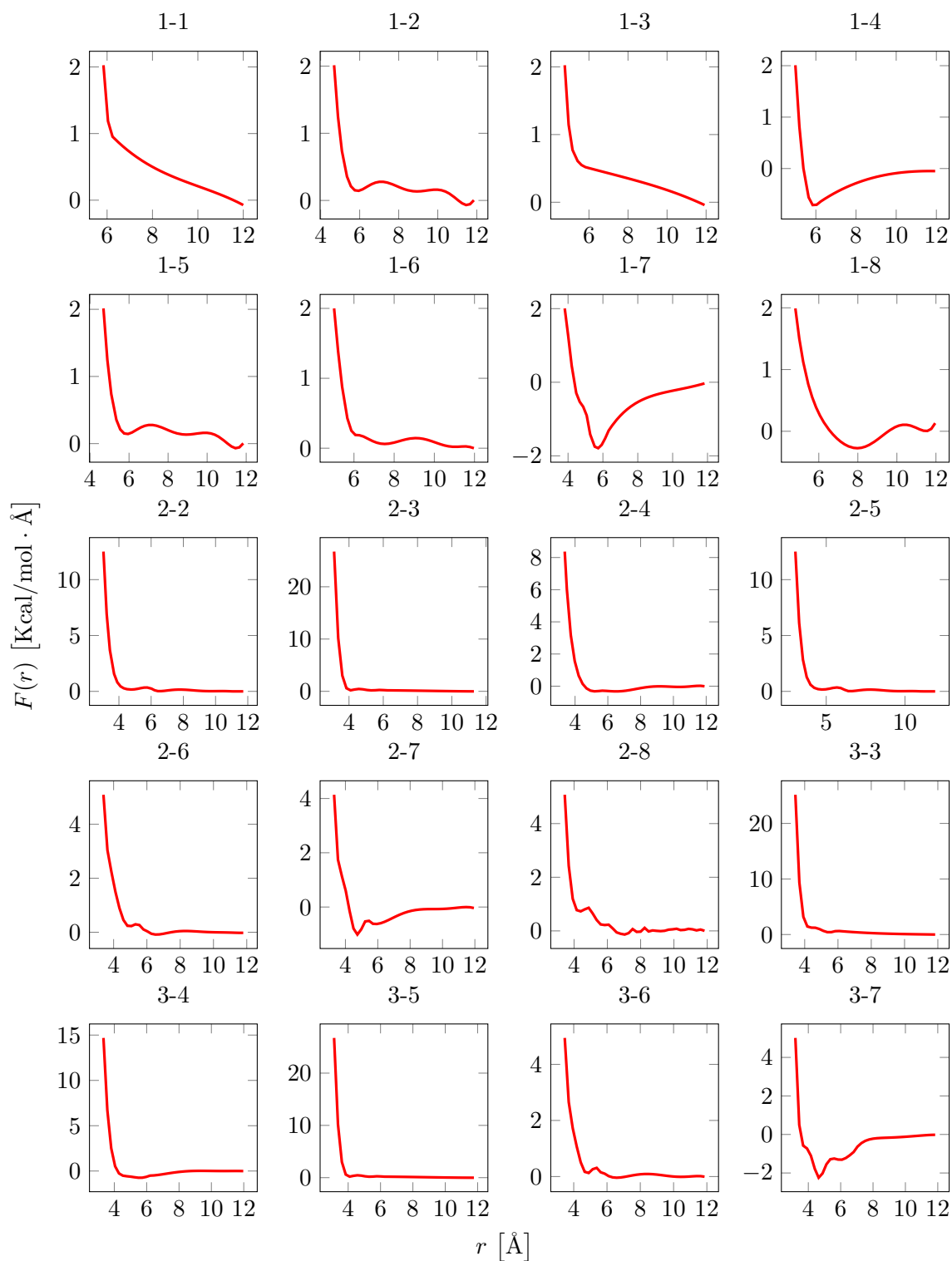
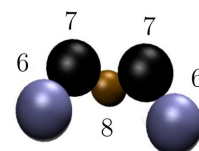
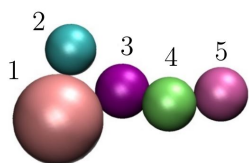


Figure A.17. Non-bonded force fields developed for the [pyr14][TFSI] ionic liquid, sampled from 363K (part 1).



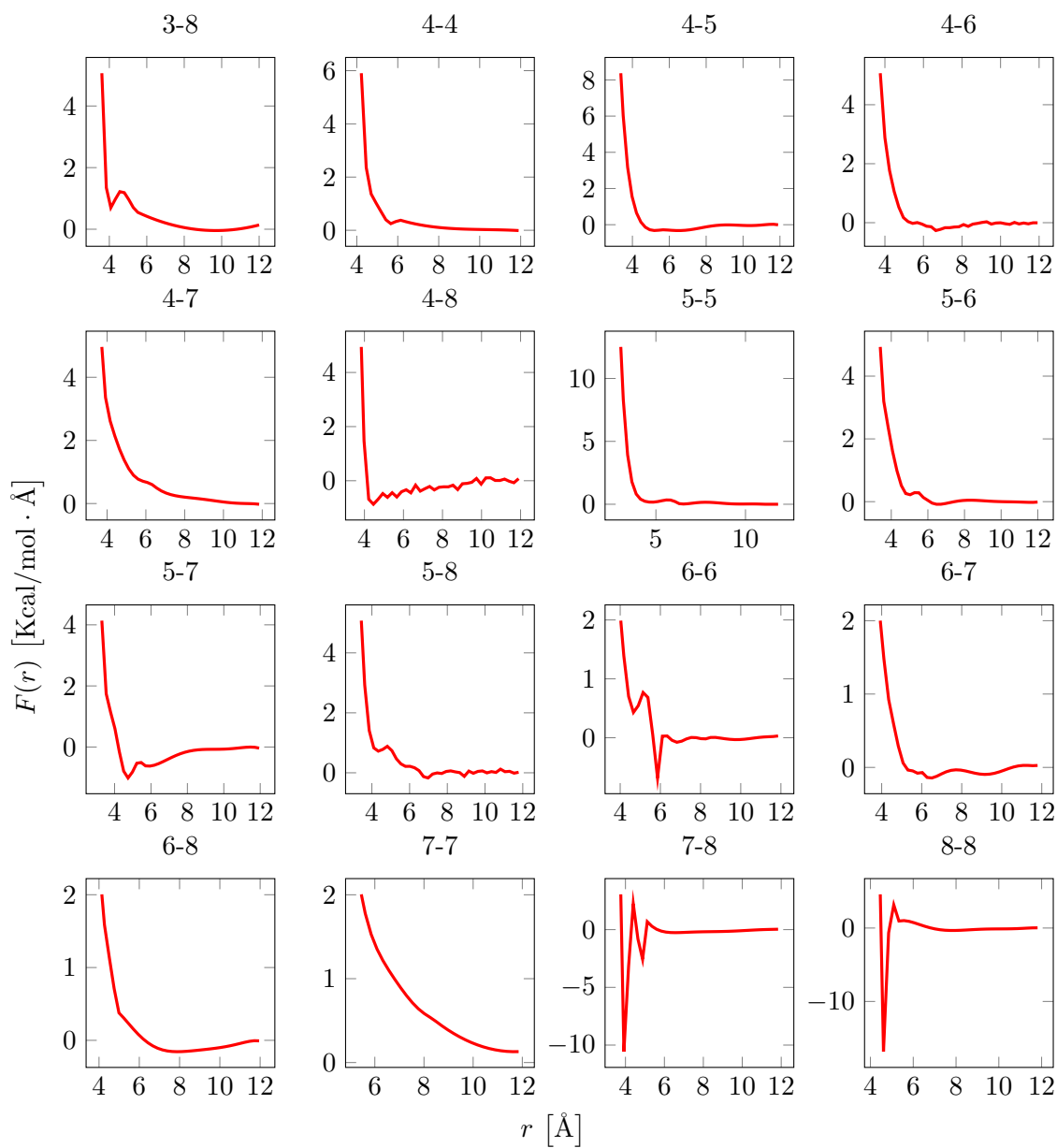
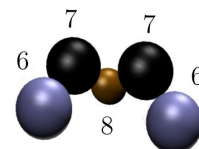
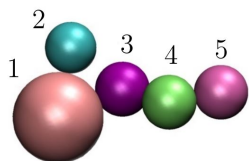


Figure A.18. Non-bonded force fields developed for the [pyr14][TFSI] ionic liquid, sampled from 363K (part 2).



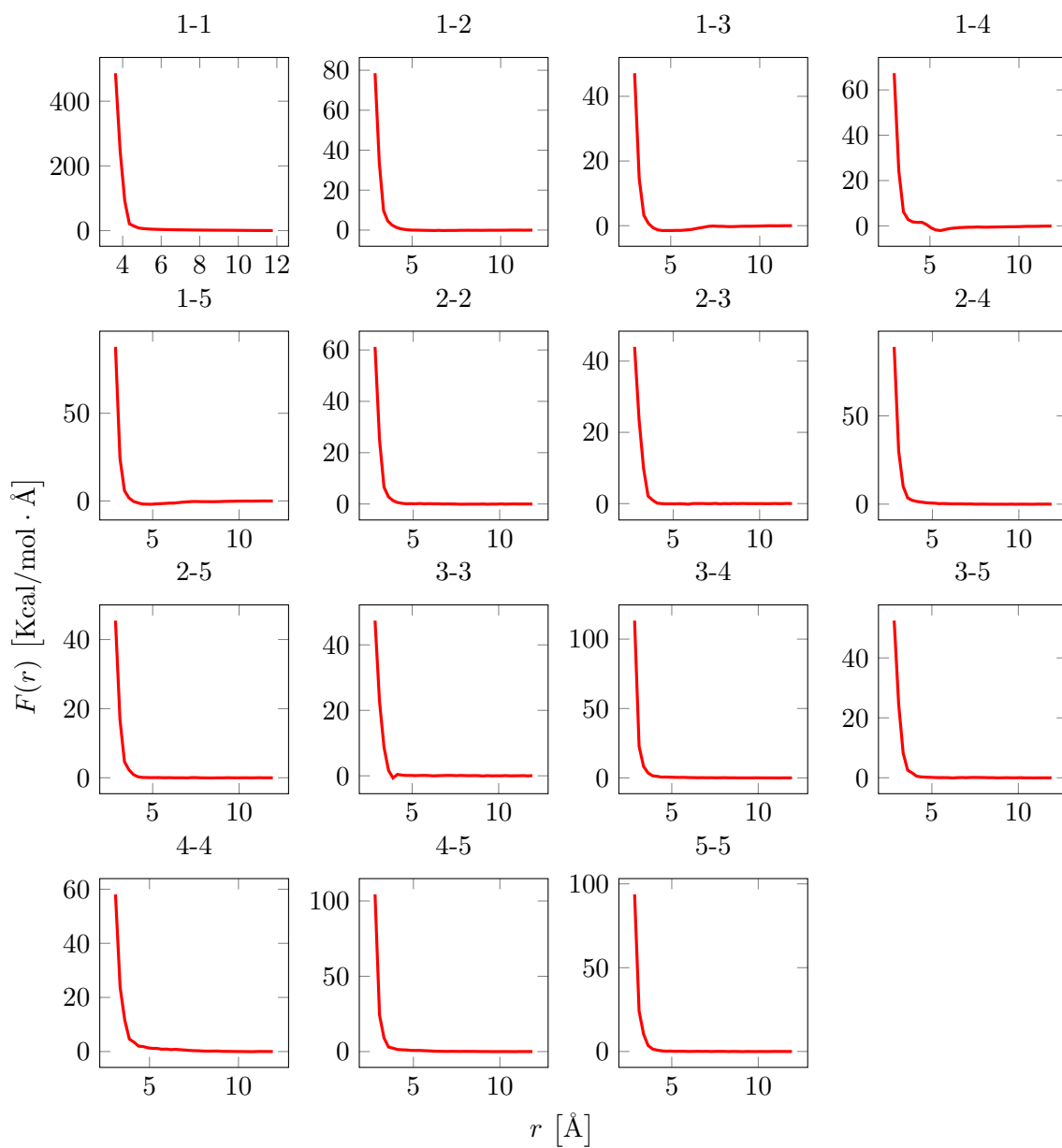
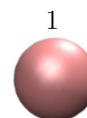
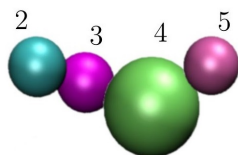


Figure A.19. Non-bonded force fields developed for the [EMIM][BF<sub>4</sub>] ionic liquid, sampled from 363K.



## A.6 Mean-square Displacements

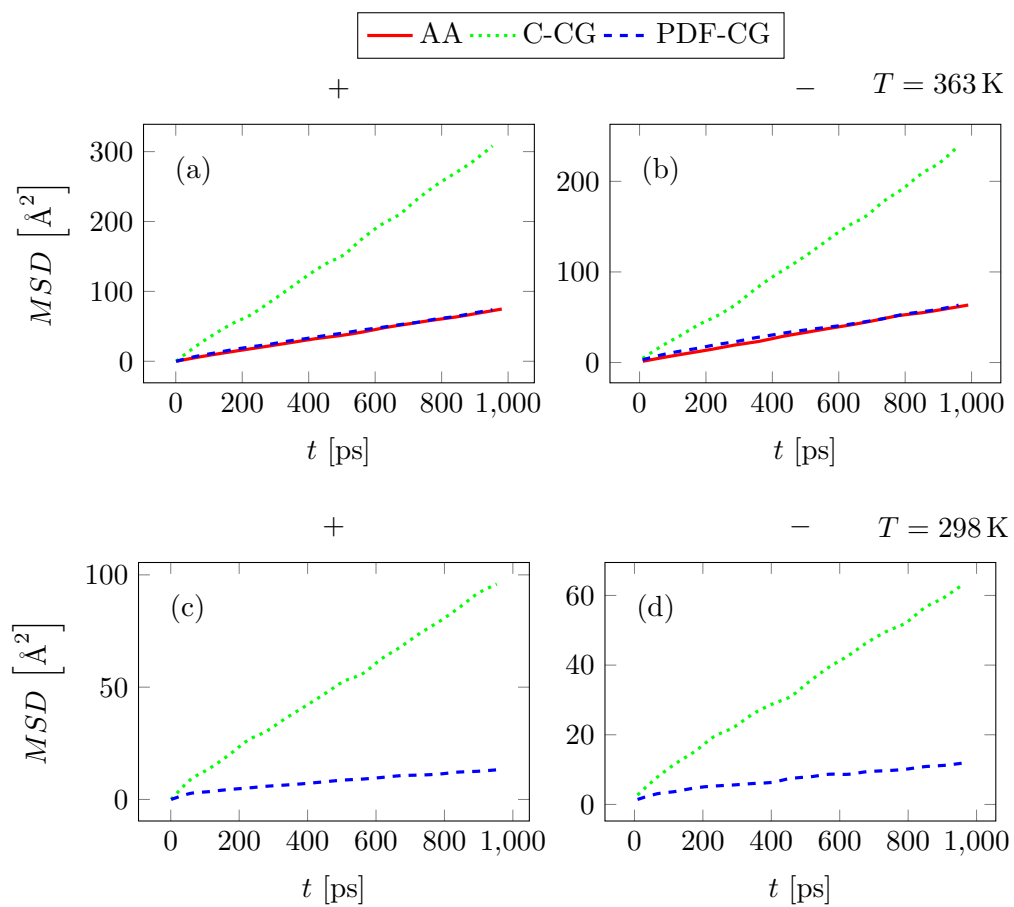
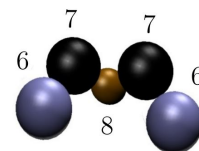
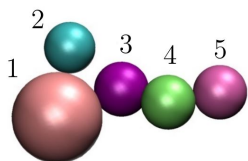


Figure A.20. Mean-square displacement of the [pyr14][TFSI] ionic liquid.



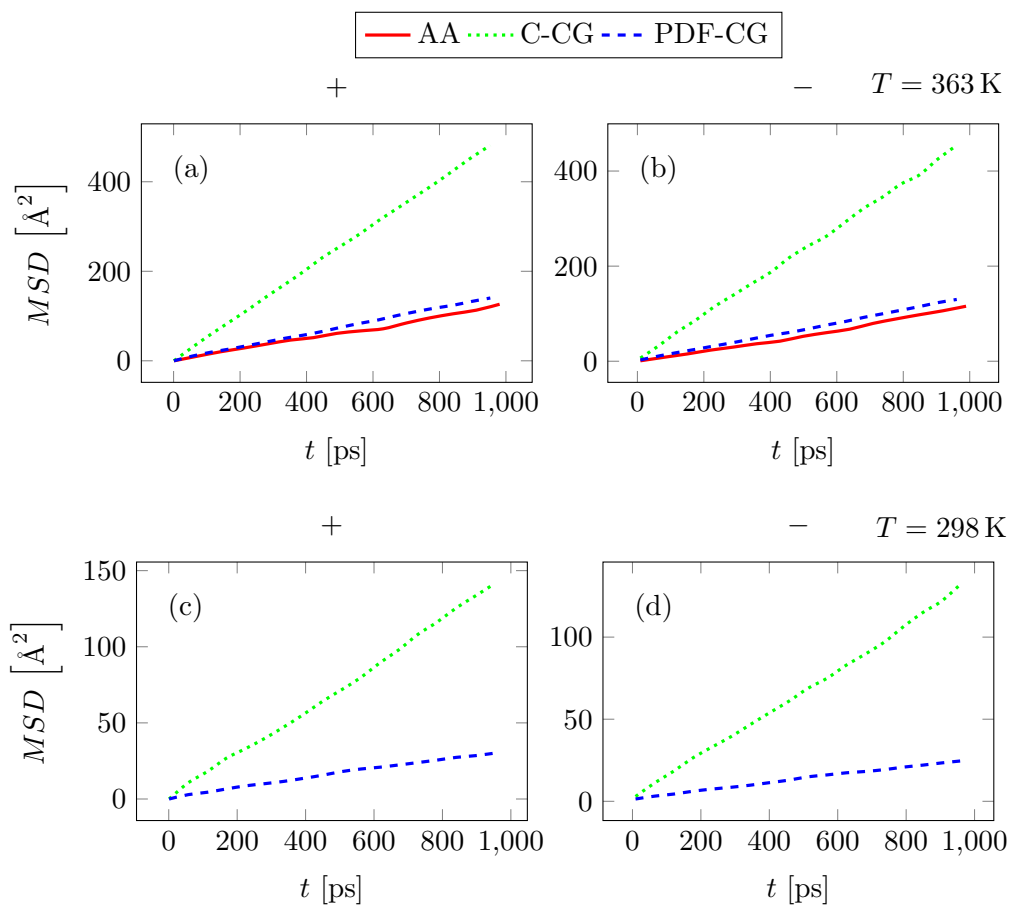
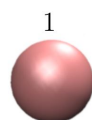
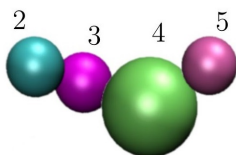


Figure A.21. Mean-square displacement of the [EMIM][BF<sub>4</sub>] ionic liquid.



## A.7 Density Profiles

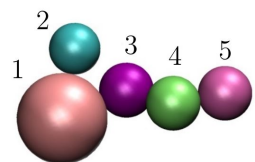
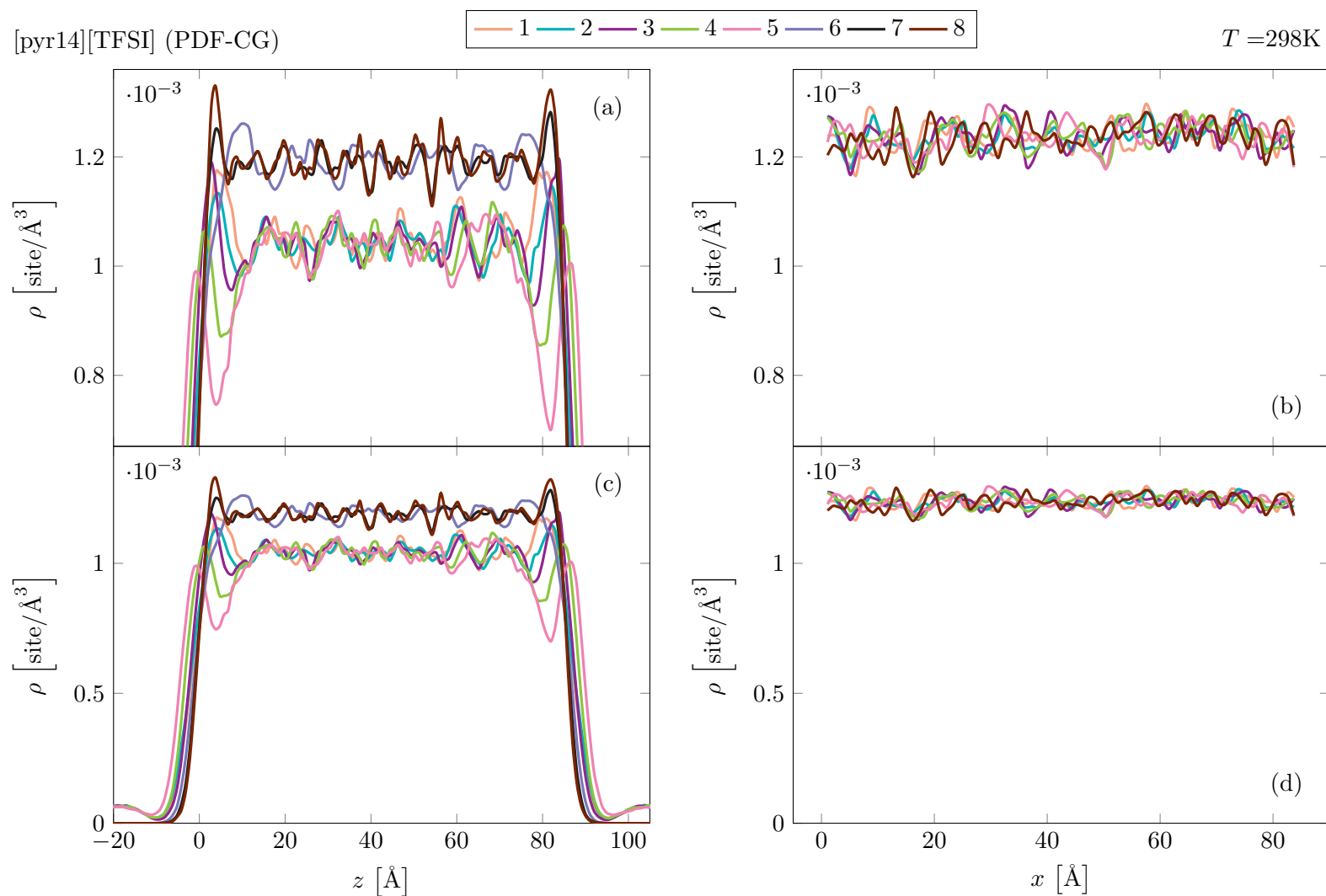
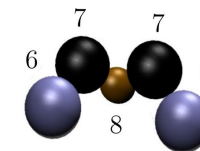


Figure A.22. All by-type number density profiles of the [pyr14][TFSI] ionic liquid at 298K: (a)-(b) in the  $z$  and  $x$ -directions respectively, zoomed in; (c)-(d) in the  $z$  and  $x$ -directions respectively, showing all data.





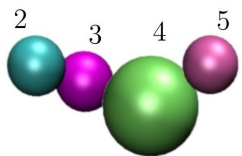
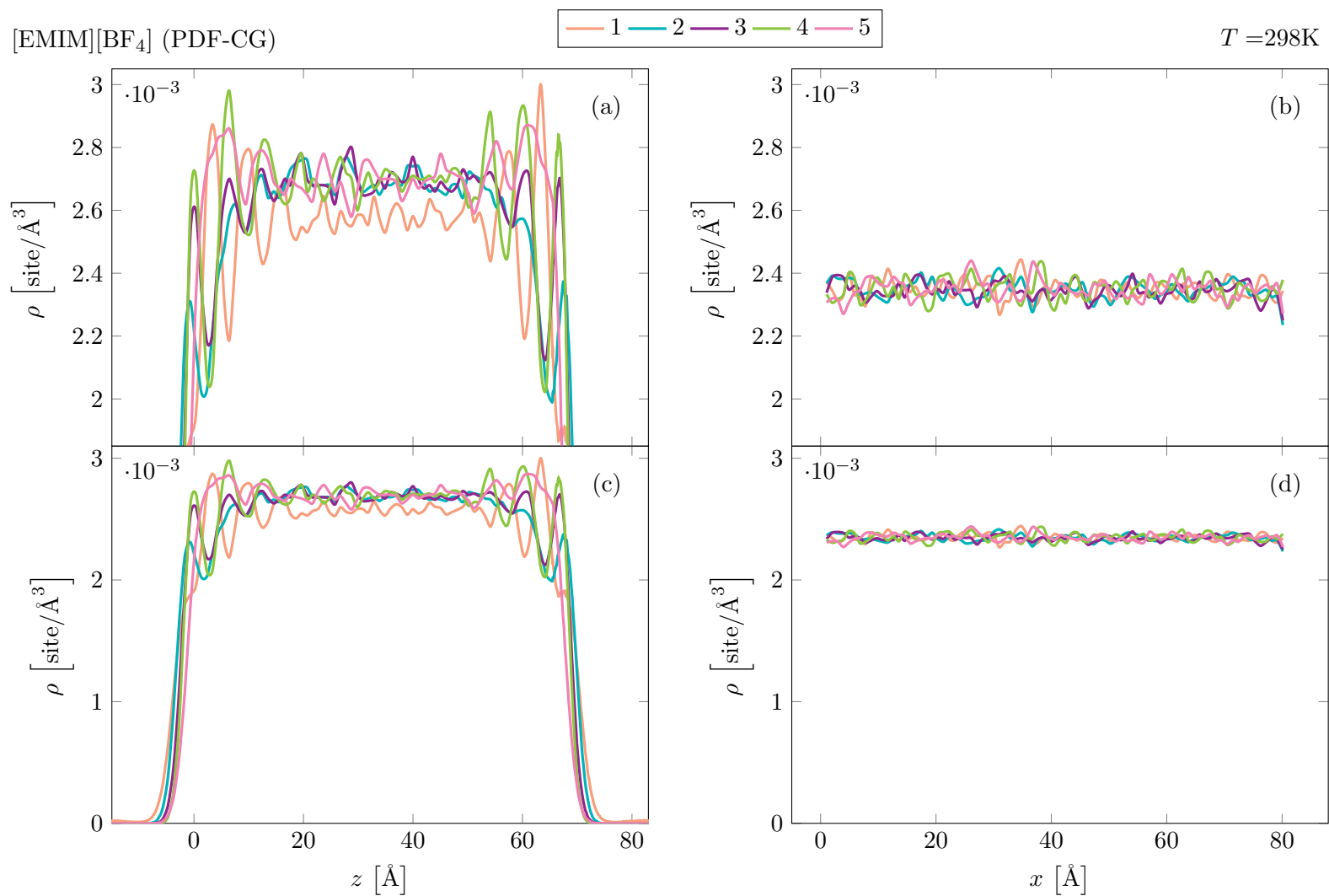
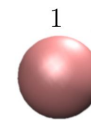


Figure A.23. All by-type number density profiles of the [EMIM][BF<sub>4</sub>] ionic liquid at 298K: (a)-(b) in the  $z$  and  $x$ -directions respectively, zoomed in; (c)-(d) in the  $z$  and  $x$ -directions respectively, showing all data.



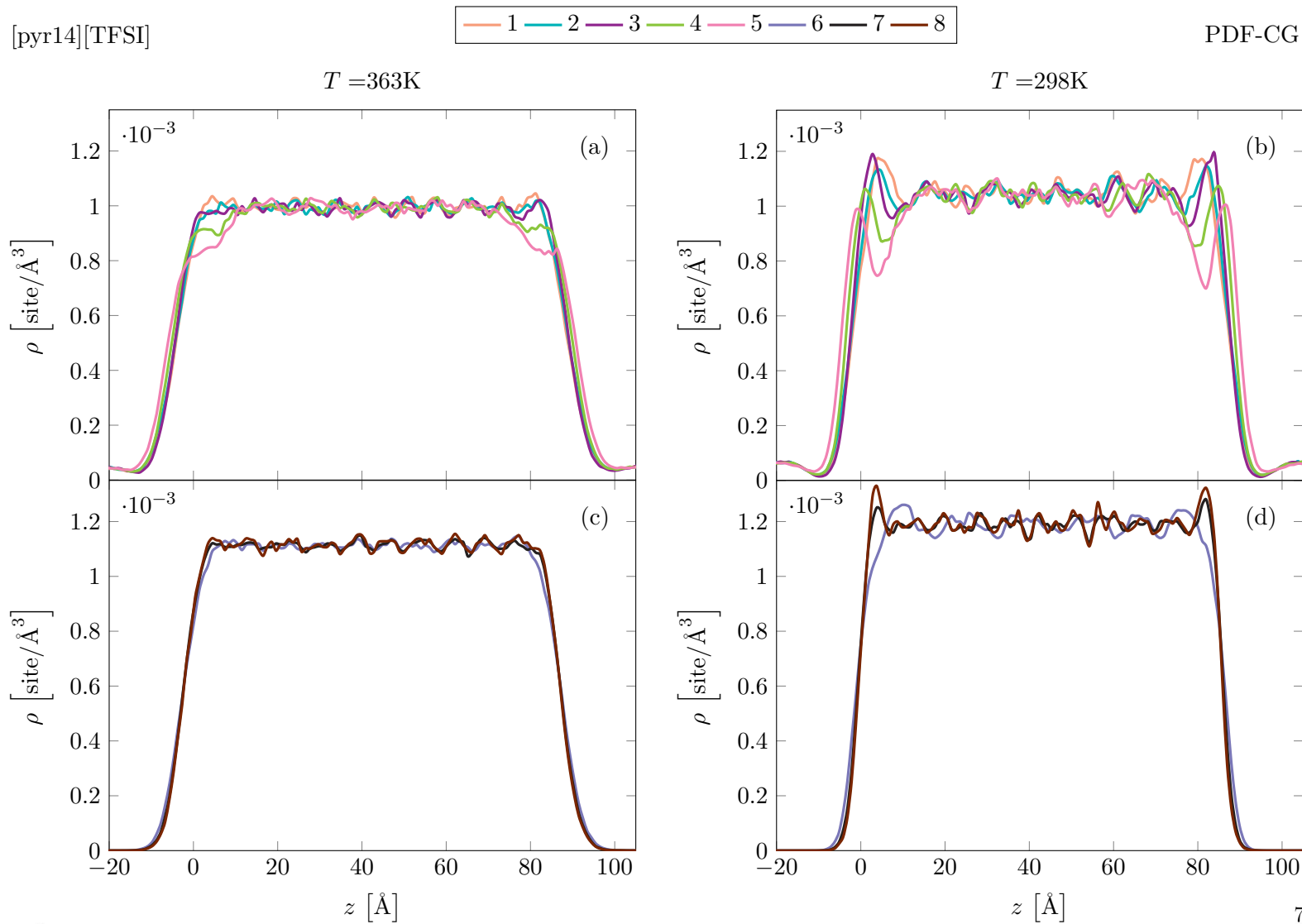
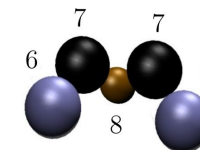
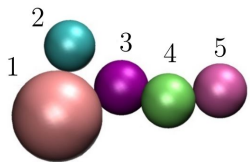


Figure A.24. The effect of temperature on  $z$ -direction [pyr14][TFSI] density profiles: (a),(c) cation and anion, respectively at 363K; (b),(d) cation and anion, respectively at 298K.



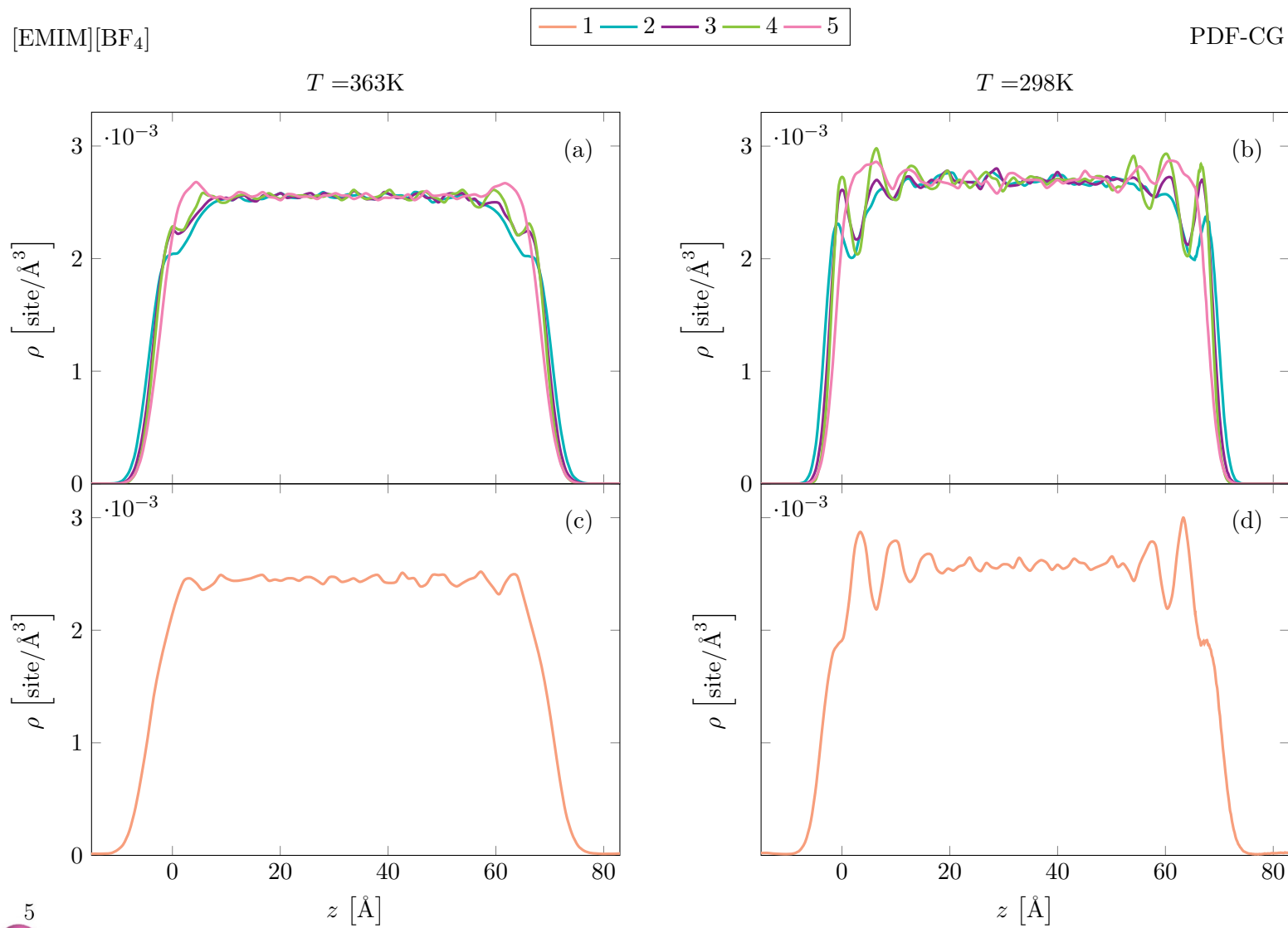


Figure A.25. The effect of temperature on  $z$ -direction [EMIM][BF<sub>4</sub>] density profiles: (a),(c) cation and anion, respectively at 363K; (b),(d) cation and anion, respectively at 298K.

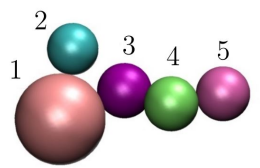
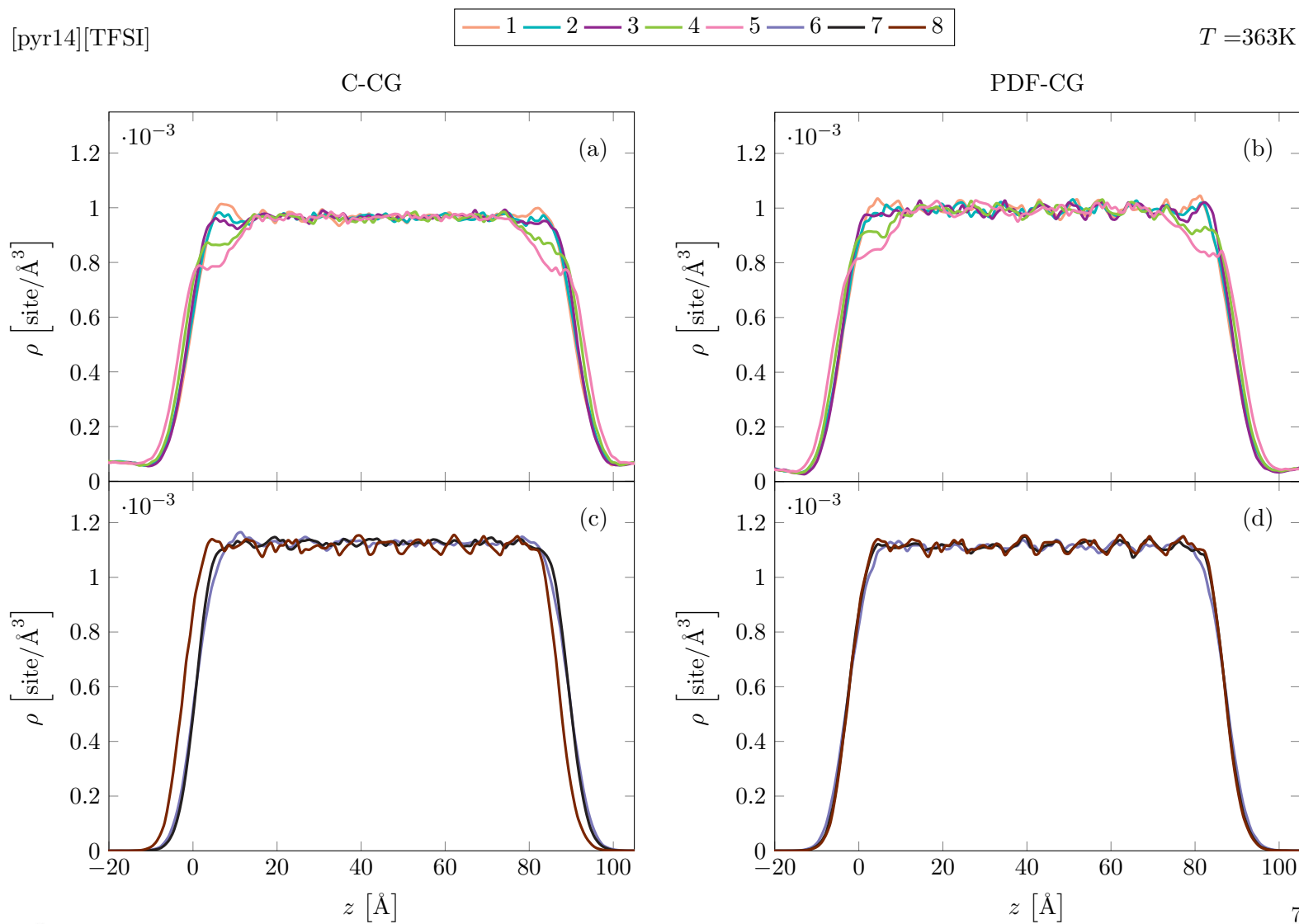
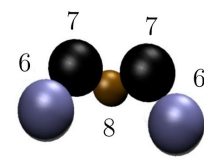


Figure A.26: The effect of CG method on  $z$ -direction [pyr14][TFSI] density profiles at 363K: (a),(c) cation and anion, respectively using C-CG; (b),(d) cation and anion, respectively using PDF-CG.



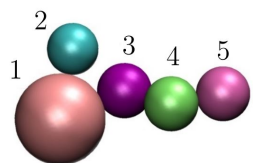
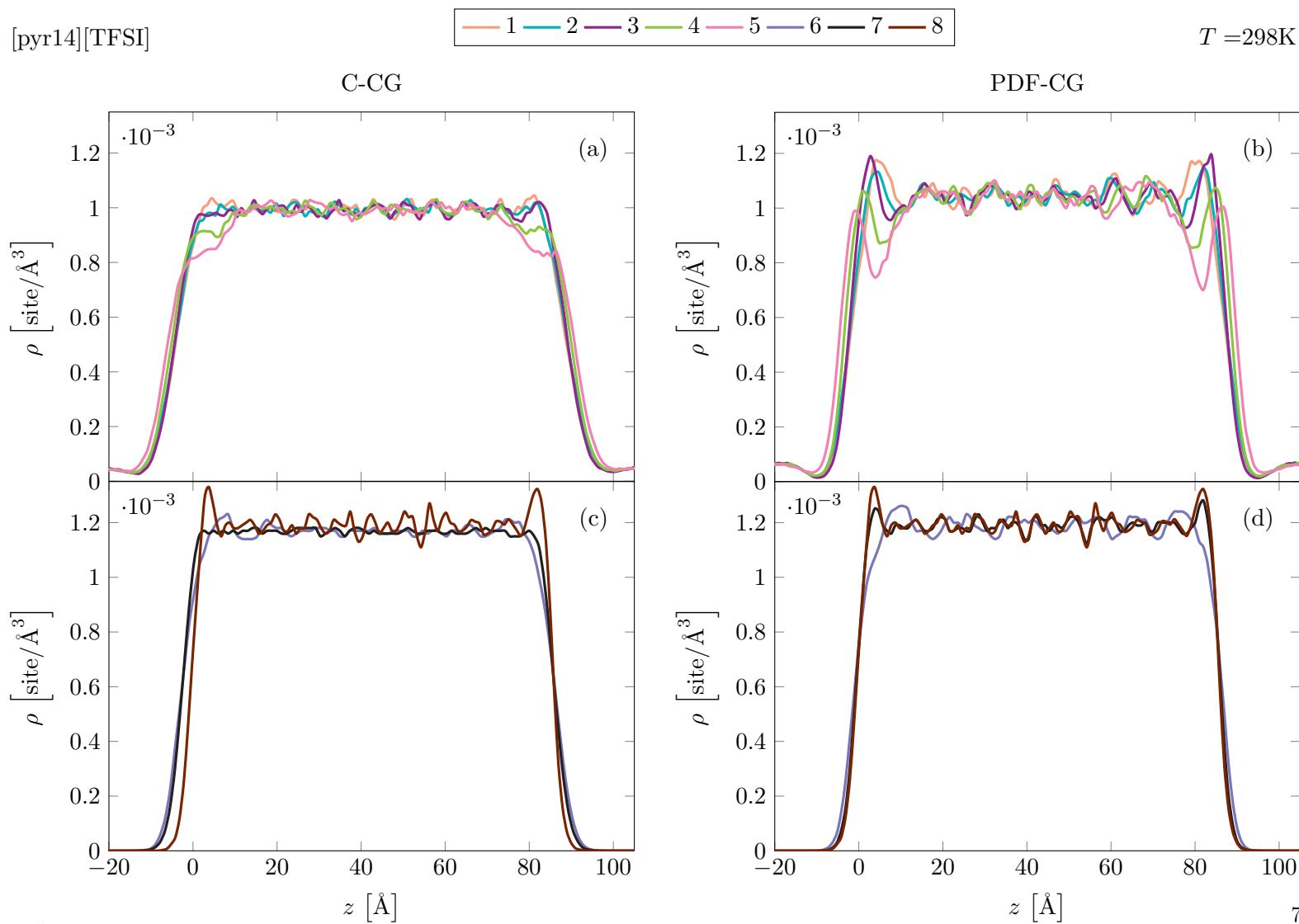
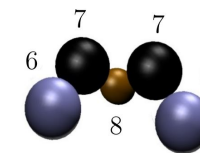
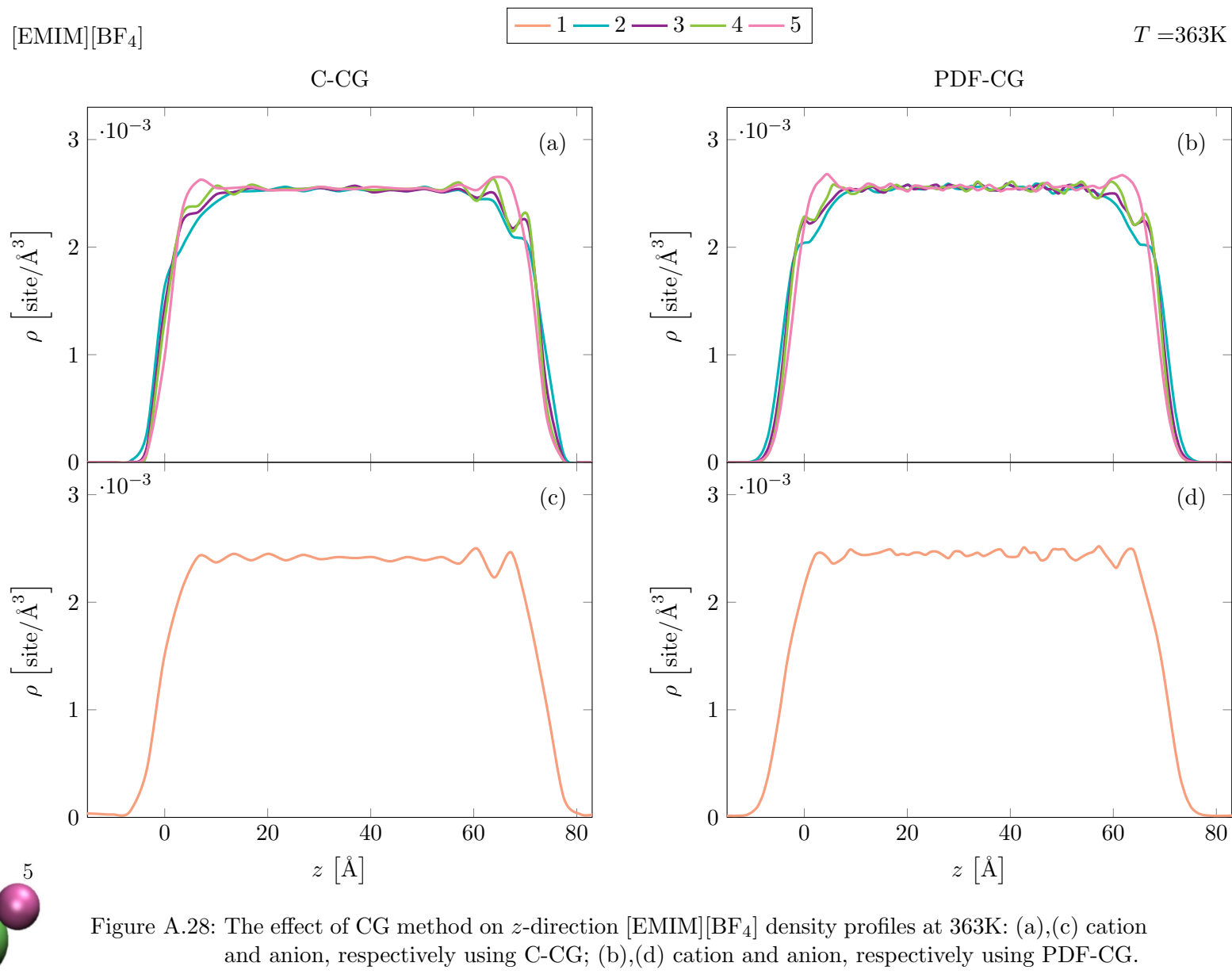


Figure A.27: The effect of CG method on  $z$ -direction [pyr14][TFSI] density profiles at 298K: (a),(c) cation and anion, respectively using C-CG; (b),(d) cation and anion, respectively using PDF-CG.





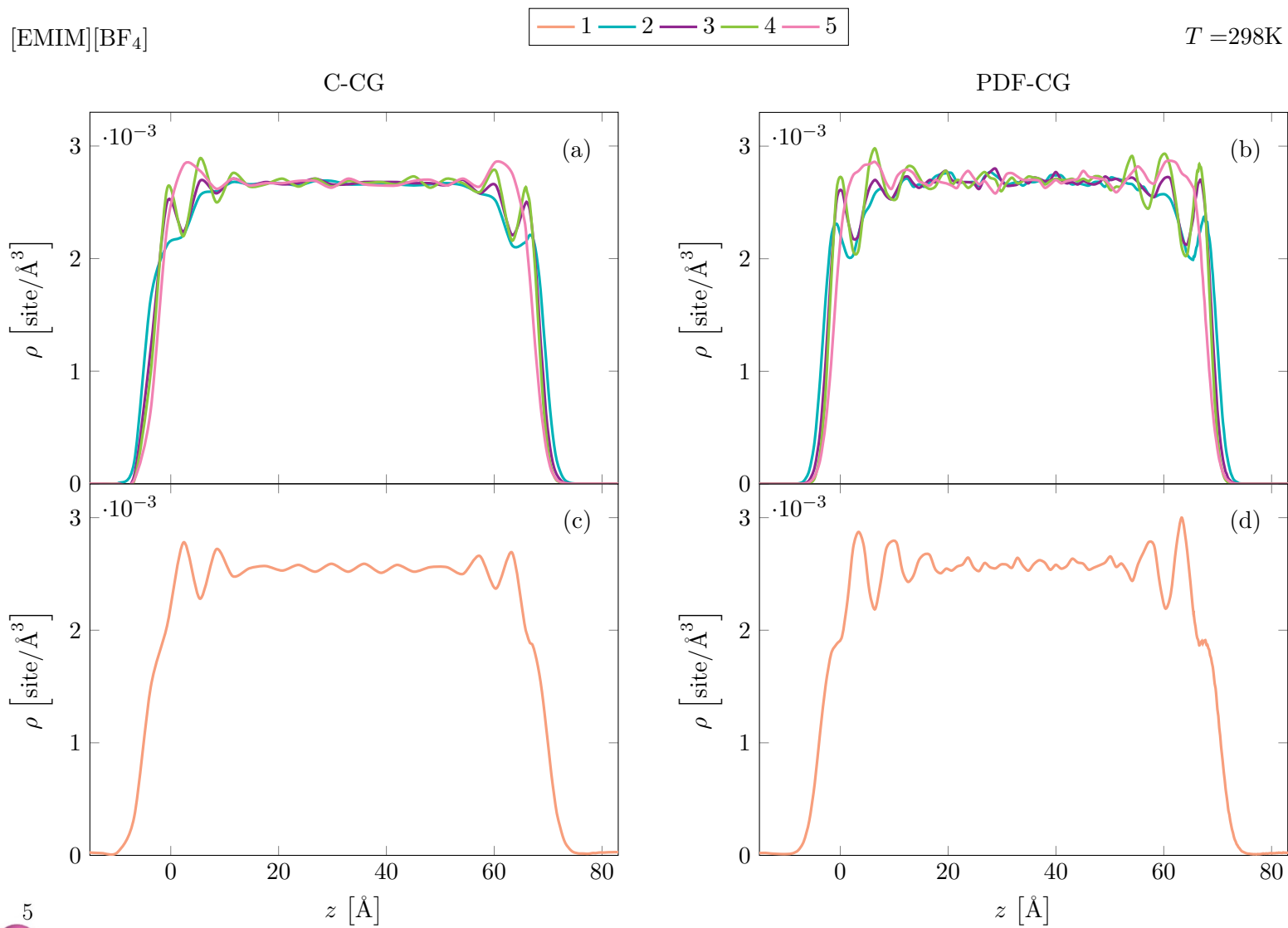
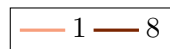


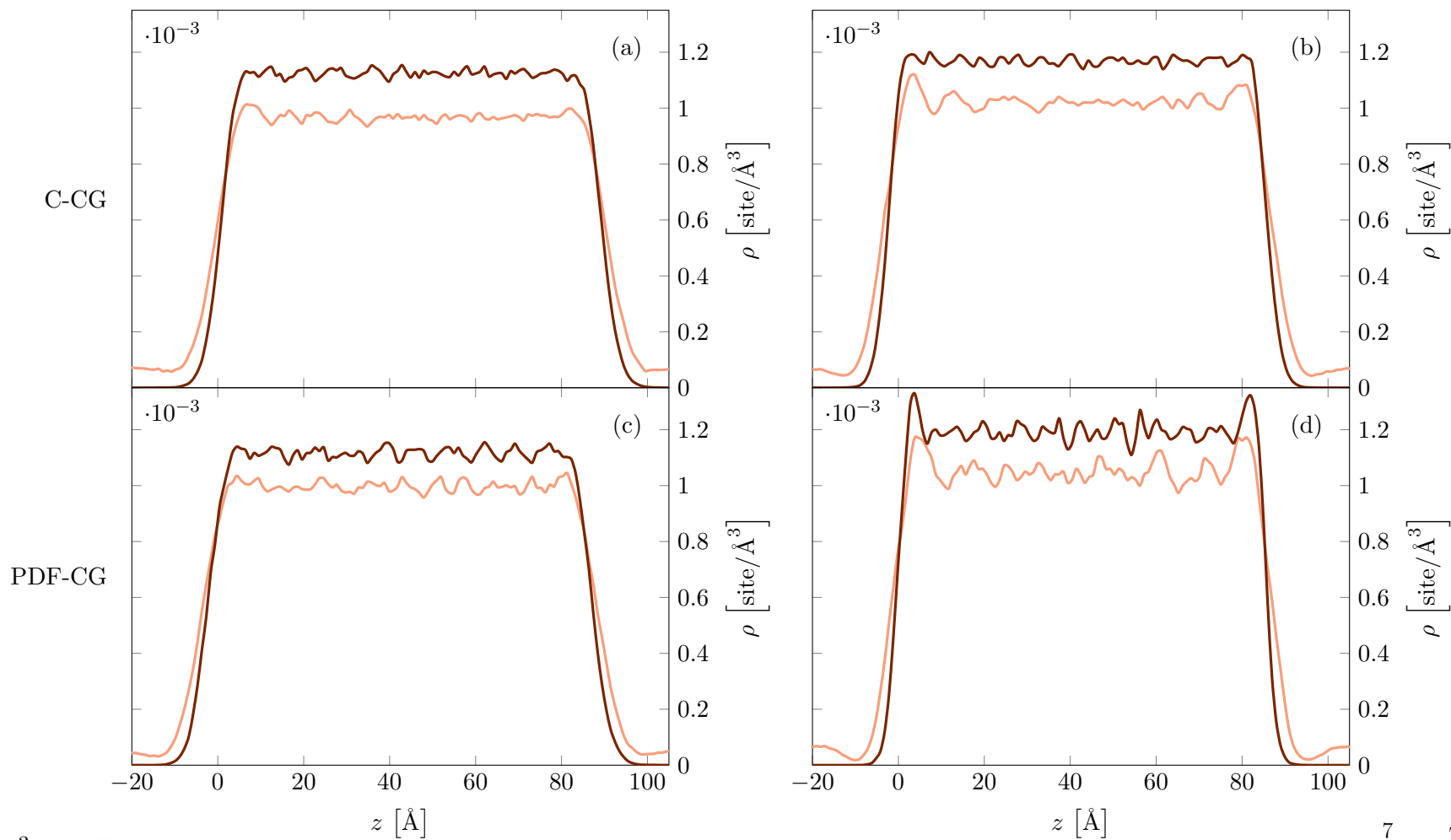
Figure A.29: The effect of CG method on  $z$ -direction [EMIM][BF<sub>4</sub>] density profiles at 298K: (a),(c) cation and anion, respectively using C-CG; (b),(d) cation and anion, respectively using PDF-CG.

[pyr14][TFSI]



$T = 363\text{K}$

$T = 298\text{K}$



19

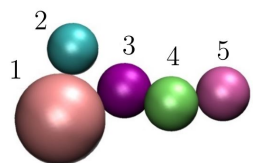
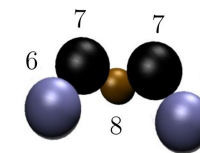
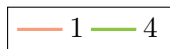


Figure A.30: Density profiles in  $z$ -direction of the main sites of [pyr14][TFSI]: (a)-(b) at 363K and 298K, respectively using C-CG; (c)-(d) at 363K and 298K, respectively using PDF-CG.



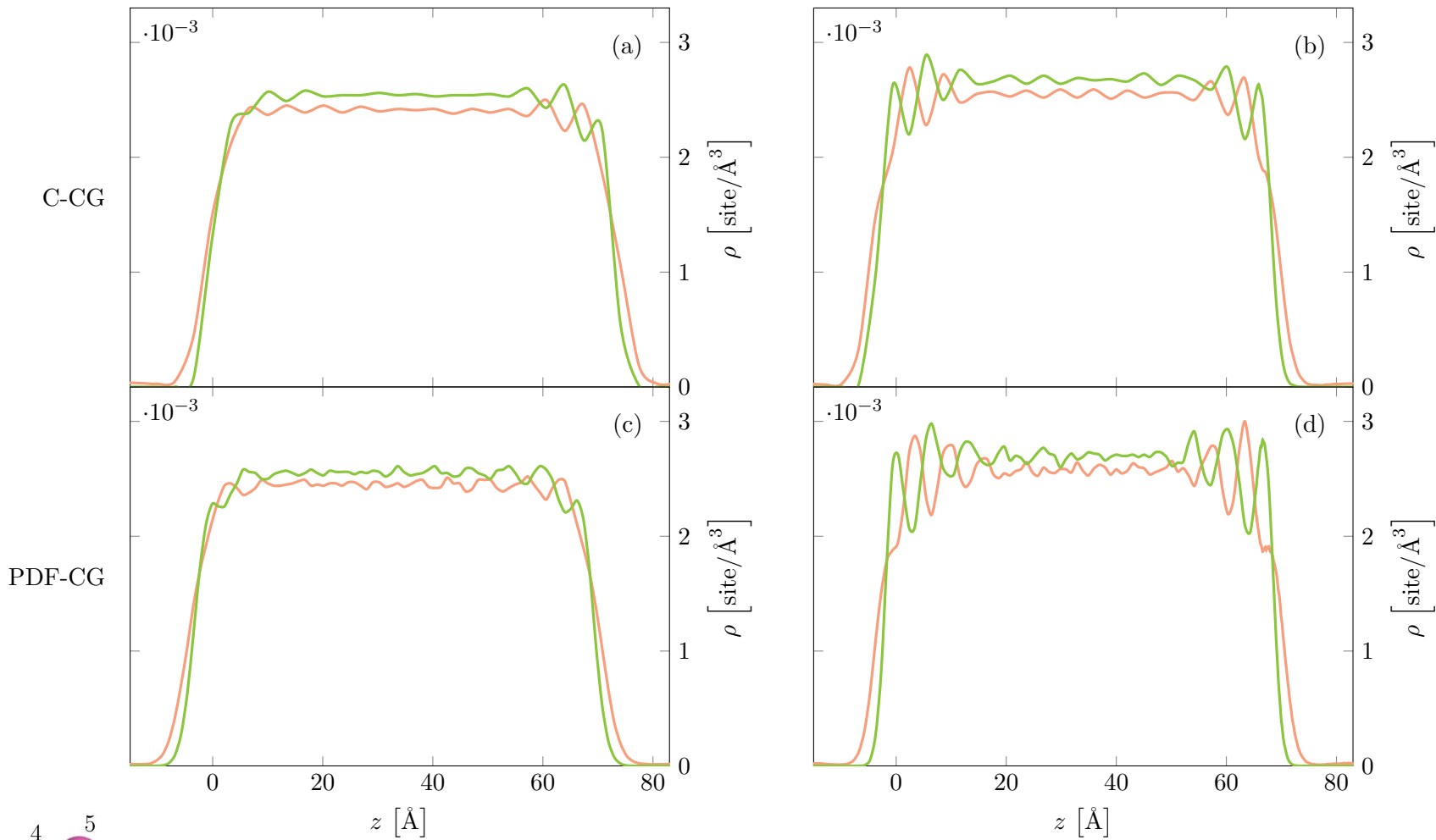


[EMIM][BF<sub>4</sub>]



$T = 363\text{K}$

$T = 298\text{K}$



62

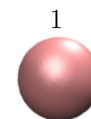
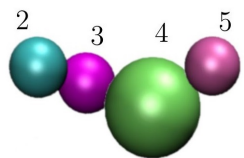


Figure A.31: Density profiles in  $z$ -direction of the main sites of [EMIM][BF<sub>4</sub>]: (a)-(b) at 363K and 298K, respectively using C-CG; (c)-(d) at 363K and 298K, respectively using PDF-CG.

# Bibliography

- [1] K. R. Seddon. “Ionic liquids for clean technology”. *Journal of Chemical Technology & Biotechnology: International Research in Process, Environmental and Clean Technology* 68.4 (1997), pp. 351–356.
- [2] S. Zhang, N. Sun, X. He, X. Lu, and X. Zhang. “Physical properties of ionic liquids: database and evaluation”. *Journal of Physical and Chemical Reference Data* 35.4 (2006), pp. 1475–1517.
- [3] T. Welton. “Room-temperature ionic liquids. Solvents for synthesis and catalysis”. *Chemical reviews* 99.8 (1999), pp. 2071–2084.
- [4] A Guerfi, M Dontigny, P Charest, M Petitclerc, M Lagacé, A Vijh, and K Zaghbi. “Improved electrolytes for Li-ion batteries: Mixtures of ionic liquid and organic electrolyte with enhanced safety and electrochemical performance”. *Journal of Power Sources* 195.3 (2010), pp. 845–852.
- [5] A Balducci, S. Jeong, G. Kim, S Passerini, M Winter, M Schmuck, G. Appetecchi, R Marcilla, D Mecerreyes, V Barsukov, et al. “Development of safe, green and high performance ionic liquids-based batteries (ILLIBATT project)”. *Journal of Power Sources* 196.22 (2011), pp. 9719–9730.
- [6] L.-L. Zhang, Z.-L. Wang, D. Xu, X.-B. Zhang, and L.-M. Wang. “The development and challenges of rechargeable non-aqueous lithium–air batteries”. *International Journal of Smart and Nano Materials* 4.1 (2013), pp. 27–46.
- [7] J. Zheng, R. Liang, M Hendrickson, and E. Plichta. “Theoretical energy density of Li–air batteries”. *Journal of The Electrochemical Society* 155.6 (2008), A432–A437.
- [8] M. Galinski, A. Lewandowski, and I. Stkepniak. “Ionic liquids as electrolytes”. *Electrochimica acta* 51.26 (2006), pp. 5567–5580.
- [9] C. Wang, Z. Xie, and Z. Zhou. “Lithium-air batteries: Challenges coexist with opportunities”. *APL Materials* 7.4 (2019), p. 040701.
- [10] V Halka, R Tsekov, and W Freyland. “Peculiarity of the liquid/vapour interface of an ionic liquid: study of surface tension and viscoelasticity of liquid BMImPF<sub>6</sub> at various temperatures”. *Physical Chemistry Chemical Physics* 7.9 (2005), pp. 2038–2043.
- [11] E. Sloutskin, B. M. Ocko, L. Tamam, I. Kuzmenko, T. Gog, and M. Deutsch. “Surface layering in ionic liquids: an X-ray reflectivity study”. *Journal of the American Chemical Society* 127.21 (2005), pp. 7796–7804.
- [12] R. Lynden-Bell. “Gas—liquid interfaces of room temperature ionic liquids”. *Molecular Physics* 101.16 (2003), pp. 2625–2633.
- [13] R. Lynden-Bell, J Kohanoff, and M. Del Popolo. “Simulation of interfaces between room temperature ionic liquids and other liquids”. *Faraday Discussions* 129 (2005), pp. 57–67.

- [14] W. D. Amith, J. J. Hettige, E. W. Castner Jr, and C. J. Margulis. “Structures of ionic liquids having both anionic and cationic octyl tails: Lamellar vacuum interface vs sponge-like bulk order”. *The Journal of Physical Chemistry Letters* 7.19 (2016), pp. 3785–3790.
- [15] R. Hayes, G. G. Warr, and R. Atkin. “Structure and nanostructure in ionic liquids”. *Chemical reviews* 115.13 (2015), pp. 6357–6426.
- [16] L. A. Jurado, H. Kim, A. Arcifa, A. Rossi, C. Leal, N. D. Spencer, and R. M. Espinosa-Marzal. “Irreversible structural change of a dry ionic liquid under nanoconfinement”. *Physical Chemistry Chemical Physics* 17.20 (2015), pp. 13613–13624.
- [17] R. S. Anareddy and S. K. Shaw. “Long-range ordering of ionic liquid fluid films”. *Langmuir* 32.20 (2016), pp. 5147–5154.
- [18] D. Parr, J. Chrestenson, K. Malik, M. Molter, C. Zibart, B. Egan, and L. M. Haverhals. “Structure and dynamics at ionic liquid/electrode interfaces”. *ECS Transactions* 66.30 (2015), pp. 35–42.
- [19] T. Yan, C. J. Burnham, M. G. Del Pópolo, and G. A. Voth. “Molecular dynamics simulation of ionic liquids: The effect of electronic polarizability”. *The Journal of Physical Chemistry B* 108.32 (2004), pp. 11877–11881.
- [20] J. B. Haskins, W. R. Bennett, J. J. Wu, D. M. Hernandez, O. Borodin, J. D. Monk, C. W. Bauschlicher Jr, and J. W. Lawson. “Computational and Experimental Investigation of Li-Doped Ionic Liquid Electrolytes:[pyr14][TFSI],[pyr13][FSI], and [EMIM][BF<sub>4</sub>]”. *The Journal of Physical Chemistry B* 118.38 (2014), pp. 11295–11309.
- [21] Y. Wang, S. Izvekov, T. Yan, and G. A. Voth. “Multiscale coarse-graining of ionic liquids”. *The Journal of Physical Chemistry B* 110.8 (2006), pp. 3564–3575.
- [22] S. Lin. *Multi-Scale Computational Materials Science Laboratory*. 2014-2017.
- [23] S. Markutsya and M. H. Lamm. “A coarse-graining approach for molecular simulation that retains the dynamics of the all-atom reference system by implementing hydrodynamic interactions”. *The Journal of Chemical Physics* 141.17 (2014), p. 174107.
- [24] A. R. Leach. *Molecular modelling: principles and applications*. Pearson Education, 2001.
- [25] N. V. Plechkova and K. R. Seddon. *Ionic Liquids Further Uncoiled: Critical Expert Overviews*. John Wiley & Sons, 2014.
- [26] S. J. Marrink, H. J. Risselada, S. Yefimov, D. P. Tieleman, and A. H. De Vries. “The MARTINI force field: coarse grained model for biomolecular simulations”. *The journal of Physical Chemistry B* 111.27 (2007), pp. 7812–7824.
- [27] L. Monticelli, S. K. Kandasamy, X. Periole, R. G. Larson, D. P. Tieleman, and S.-J. Marrink. “The MARTINI coarse-grained force field: extension to proteins”. *Journal of Chemical Theory and Computation* 4.5 (2008), pp. 819–834.
- [28] A. P. Lyubartsev and A. Laaksonen. “Calculation of effective interaction potentials from radial distribution functions: A reverse Monte Carlo approach”. *Physical Review E* 52.4 (1995), p. 3730.
- [29] F. Müller-Plathe. “Coarse-graining in polymer simulation: from the atomistic to the mesoscopic scale and back”. *ChemPhysChem* 3.9 (2002), pp. 754–769.
- [30] D. Reith, M. Pütz, and F. Müller-Plathe. “Deriving effective mesoscale potentials from atomistic simulations”. *Journal of Computational Chemistry* 24.13 (2003), pp. 1624–1636.

- [31] T. Murtola, E. Falck, M. Patra, M. Karttunen, and I. Vattulainen. “Coarse-grained model for phospholipid/cholesterol bilayer”. *The Journal of Chemical Physics* 121.18 (2004), pp. 9156–9165.
- [32] S. Izvekov and G. A. Voth. “Effective force field for liquid hydrogen fluoride from ab initio molecular dynamics simulation using the force-matching method”. *The Journal of Physical Chemistry B* 109.14 (2005), pp. 6573–6586.
- [33] S. Izvekov and G. A. Voth. “Multiscale coarse graining of liquid-state systems”. *The Journal of Chemical Physics* 123.13 (2005), p. 134105.
- [34] W. Noid, J.-W. Chu, G. S. Ayton, V. Krishna, S. Izvekov, G. A. Voth, A. Das, and H. C. Andersen. “The multiscale coarse-graining method. I. A rigorous bridge between atomistic and coarse-grained models”. *The Journal of Chemical Physics* 128.24 (2008), p. 244114.
- [35] W. Noid, P. Liu, Y. Wang, J.-W. Chu, G. S. Ayton, S. Izvekov, H. C. Andersen, and G. A. Voth. “The multiscale coarse-graining method. II. Numerical implementation for coarse-grained molecular models”. *The Journal of Chemical Physics* 128.24 (2008), p. 244115.
- [36] R. McGreevy and L Pusztai. “Reverse Monte Carlo simulation: a new technique for the determination of disordered structures”. *Molecular Simulation* 1.6 (1988), pp. 359–367.
- [37] T. C. Moore, C. R. Iacovella, and C. McCabe. “Derivation of coarse-grained potentials via multistate iterative Boltzmann inversion”. *The Journal of Chemical Physics* 140.22 (2014), p. 224104.
- [38] G. A. Voth. *Coarse-graining of condensed phase and biomolecular systems*. CRC press, 2009, pp. 1–4.
- [39] J. Weiner and R. Forman. “Rate theory for solids. IV. Classical Brownian-motion model”. *Physical Review B* 10.2 (1974), p. 315.
- [40] N Böckenfeld, M Willeke, J. Pires, M. Anouti, and A. Balducci. “On the use of lithium iron phosphate in combination with protic ionic liquid-based electrolytes”. *Journal of The Electrochemical Society* 160.4 (2013), A559–A563.
- [41] S Menne, J Pires, M Anouti, and A Balducci. “Protic ionic liquids as electrolytes for lithium-ion batteries”. *Electrochemistry Communications* 31 (2013), pp. 39–41.
- [42] O. Borodin and G. D. Smith. “Development of many-body polarizable force fields for Li-battery components: 1. ether, alkane, and carbonate-based solvents”. *The Journal of Physical Chemistry B* 110.12 (2006), pp. 6279–6292.
- [43] O. Borodin and G. D. Smith. “Development of many-body polarizable force fields for Li-Battery applications: 2. LiTFSI-doped oligoether, polyether, and carbonate-based electrolytes”. *The Journal of Physical Chemistry B* 110.12 (2006), pp. 6293–6299.
- [44] O. Borodin. “Polarizable force field development and molecular dynamics simulations of ionic liquids”. *The Journal of Physical Chemistry B* 113.33 (2009), pp. 11463–11478.
- [45] J. N. Canongia Lopes and A. A. Pádua. “Using spectroscopic data on imidazolium cation conformations to test a molecular force field for ionic liquids”. *The Journal of Physical Chemistry B* 110.14 (2006), pp. 7485–7489.
- [46] P. Hunt. “The simulation of imidazolium-based ionic liquids”. *Molecular Simulation* 32.01 (2006), pp. 1–10.

- [47] S. Nosé. “A unified formulation of the constant temperature molecular dynamics methods”. *The Journal of Chemical Physics* 81.1 (1984), pp. 511–519.
- [48] W. G. Hoover. “Canonical dynamics: Equilibrium phase-space distributions”. *Physical Review A* 31.3 (1985), p. 1695.
- [49] S. Plimpton. “Fast parallel algorithms for short-range molecular dynamics”. *Journal of computational physics* 117.1 (1995), pp. 1–19. URL: <http://lammps.sandia.gov>.
- [50] C. L. Lawson and R. J. Hanson. *Solving least squares problems*. Prentice-Hall, Englewood Cliffs, 1974.
- [51] A. Einstein. “Über die von der molekularkinetischen Theorie der Wärme geforderte Bewegung von in ruhenden Flüssigkeiten suspendierten Teilchen”. *Annalen der Physik* 322.8 (1905), pp. 549–560.
- [52] A. Elbourne, K. Voitchovsky, G. G. Warr, and R. Atkin. “Ion structure controls ionic liquid near-surface and interfacial nanostructure”. *Chemical science* 6.1 (2015), pp. 527–536.
- [53] W. Jiang, Y. Wang, T. Yan, and G. A. Voth. “A multiscale coarse-graining study of the liquid/vacuum interface of room-temperature ionic liquids with alkyl substituents of different lengths”. *The Journal of Physical Chemistry C* 112.4 (2008), pp. 1132–1139.

# Tyler D. Stoffel

Ph.D. Student

Department of Mechanical Engineering

University of Kentucky

## Education

**University of Kentucky, GPA: 3.88** Paducah, KY  
*MSc Mechanical Engineering w/Focus on Thermal Fluids* 2018-2019 (Thesis Submitted)

**University of Kentucky, GPA: 3.95** Paducah, KY  
*BSc, Summa cum Laude, Mechanical Engineering* 2014 - 2018

## Awards & Affiliations

Kentucky Space Grant Consortium Graduate Fellowship . . . . . 2019  
Kentucky Space Grant Consortium Undergraduate Grant . . . . . 2016  
Dean's List-University of Kentucky . . . . . Fall 2016-Spring 2018  
Dean's List-West Kentucky Community and Technical College . Fall 2014-Spring 2016  
Outstanding Physics and Thermodynamics Student . . . . . 2016-17  
Pi Tau Sigma, National Mechanical Engineering Honor Society . . Inducted Fall 2016  
Tau Beta Pi, National Engineering Honor Society . . . . . Inducted Spring 2017  
Great Lakes National Scholarship . . . . . 2016-17  
The Ernest L. Baulch and Marcia E. Baulch AARL Scholarship . . . . . 2017-18

## Professional Experience

**University of Kentucky** Lexington, KY  
*Graduate Teaching Assistant* Current

**University of Kentucky** Paducah, KY  
*Graduate Research Assistant* 2018-2019

**University of Kentucky** Paducah, KY  
*Lab Technician* 2016-2018

**Fore-Front Mechanical** Wausau, WI  
*Mechanical Designer* 2014-2016

**Island City Engineering LLC** Merrill, WI  
*Mechanical Designer* 2013-2015

**Londerville Steel Enterprises** Wausau, WI  
*Machinery Operator* 2012-2014

## Publications/Presentations

1. *Poster*: Tyler D. Stoffel, Jordan Garcia, Colton Roach, Y Charles Lu, “Analysis of Interfacial Stress Transfers in Graphene-Polymer Nanocomposites”
  - (a) Presented at National Conference on Undergraduate Research (NCUR), Memphis, TN 04/07/2017
2. *Poster*: Jordan Garcia, Tyler D. Stoffel, Johnson Joseph, Y. Charles Lu, “Integrated Computational Design of Material Engineering 3D CNT/Graphene Hybrid Nanomaterials”
  - (a) 1st place in Engineering poster presentations at Kentucky Academy of Science (KAS) Conference, Murray, KY 11/04/2017
  - (b) Presented at National Conference on Undergraduate Research (NCUR), Memphis, TN 04/07/2017
3. *Oral Presentation*: Tyler D. Stoffel, Justin B. Haskins, John W. Lawson, Sergiy Markutsya, “Interfacial Structure of Ionic Liquids Studied with Coarse-grained Molecular Dynamics”
  - (a) Presented at 2019 American Institute of Chemical Engineers (AIChE) Annual Meeting, Orlando, FL 11/12/2019
4. *Master’s Thesis (Submitted)*: Tyler D. Stoffel, “Coarse-Grained Dynamically Accurate Simulations of Ionic Liquids at Vacuum-Interface” (Relevant Article for Publication in Progress)